Smart inverters for seamless voltage and frequency dynamics in microgrids

by

Mohsen Shid Pilehvar

B.Sc., Ferdowsi University of Mashhad, 2011

M.Sc., Shiraz University of Technology, 2013

AN ABSTRACT OF A DISSERTATION

submitted in partial fulfillment of the
requirements for the degree

DOCTOR OF PHILOSOPHY

Mike Wiegers Department of Electrical & Computer Engineering
Carl R. Ice College of Engineering

KANSAS STATE UNIVERSITY
Manhattan, Kansas

2021

Abstract

This dissertation focuses on improving the dynamic behavior of microgrids during the abnormal conditions. For this purpose, novel approaches are presented to turn the conventional inverters implemented in distributed generation (DG) units into smart inverters capable of dealing with disturbances. In the context of microgrids, the *smartness* of an inverter is tied to its ability to cope with abnormalities such as sudden load changes, loss of generation, and transitions between different modes of operation. Founded on these principles, this dissertation advances the state-of-the-art in enhancing the dynamic response of microgrids. To this end, firstly, a new approach of forming smart loads in a fleet of nanogrids, which is also referred as a grid of nanogrids (GNG), is presented in this dissertation. The proposed smart load configuration is obtained via series connection of electric dampers (EDs) with critical loads to cope with disturbances at the point of critical loads. A systematic approach is presented for modeling of the proposed smart loads considering the switching states of EDs. The stability of the smart loads is then studied using the developed state-space model. Secondly, the conventional controllers of battery energy storage system (BESS) and photovoltaic (PV) units are modified in this dissertation in order to enable them to participate in dynamic-response enhancement of islanded mixed-inertia microgrids. For this purpose, two piecewise linear-elliptic (PLE) droops are proposed and employed in BESS to improve the voltage and frequency profiles during abnormalities. Besides, the controllers of PV units are equipped with an adaptive piecewise droop (APD) to cope with disturbances. Lastly, an approach is presented in this dissertation for seamless interconnection of three single-phase feeders at distribution level for residential communities that are suffering from power imbalance within the phases during islanded mode. To attain this, a seamless transition

algorithm is presented which monitors the system condition in real time and sends appropriate commands to the static transfer switches (STSs) and modified controllers of single-phase inverters. Using the proposed method for interconnecting the isolated single-phase feeders results in forming a unified single-phase residential microgrid and maintaining the power balance and voltage level within all three phases. Moreover, the proposed approach enables the residential community to seamlessly reconnect to the main grid after resolving the abnormal condition on the grid side. In this dissertation, numerous case studies are carried out in PSCAD/EMTDC environment to validate the viability of proposed approaches in improving the dynamic behavior of microgrids.

Smart inverters for seamless voltage and frequency dynamics in microgrids

by

Mohsen Shid Pilehvar

B.Sc., Ferdowsi University of Mashhad, 2011

M.Sc., Shiraz University of Technology, 2013

A DISSERTATION

submitted in partial fulfillment of the
requirements for the degree

DOCTOR OF PHILOSOPHY

Mike Wiegers Department of Electrical & Computer Engineering
Carl R. Ice College of Engineering

KANSAS STATE UNIVERSITY
Manhattan, Kansas

2021

Approved by:

Major Professor
Professor Behrooz Mirafzal

Copyright

Abstract

This dissertation focuses on improving the dynamic behavior of microgrids during the abnormal conditions. For this purpose, novel approaches are presented to turn the conventional inverters implemented in distributed generation (DG) units into smart inverters capable of dealing with disturbances. In the context of microgrids, the *smartness* of an inverter is tied to its ability to cope with abnormalities such as sudden load changes, loss of generation, and transitions between different modes of operation. Founded on these principles, this dissertation advances the state-of-the-art in enhancing the dynamic response of microgrids. To this end, firstly, a new approach of forming smart loads in a fleet of nanogrids, which is also referred as a grid of nanogrids (GNG), is presented in this dissertation. The proposed smart load configuration is obtained via series connection of electric dampers (EDs) with critical loads to cope with disturbances at the point of critical loads. A systematic approach is presented for modeling of the proposed smart loads considering the switching states of EDs. The stability of the smart loads is then studied using the developed state-space model. Secondly, the conventional controllers of battery energy storage system (BESS) and photovoltaic (PV) units are modified in this dissertation in order to enable them to participate in dynamic-response enhancement of islanded mixed-inertia microgrids. For this purpose, two piecewise linear-elliptic (PLE) droops are proposed and employed in BESS to improve the voltage and frequency profiles during abnormalities. Besides, the controllers of PV units are equipped with an adaptive piecewise droop (APD) to cope with disturbances. Lastly, an approach is presented in this dissertation for seamless interconnection of three single-phase feeders at distribution level for residential communities that are suffering from power imbalance within the phases during islanded mode. To attain this, a seamless transition

algorithm is presented which monitors the system condition in real time and sends appropriate commands to the static transfer switches (STSs) and modified controllers of single-phase inverters. Using the proposed method for interconnecting the isolated single-phase feeders results in forming a unified single-phase residential microgrid and maintaining the power balance and voltage level within all three phases. Moreover, the proposed approach enables the residential community to seamlessly reconnect to the main grid after resolving the abnormal condition on the grid side. In this dissertation, numerous case studies are carried out in PSCAD/EMTDC environment to validate the viability of proposed approaches in improving the dynamic behavior of microgrids.

Table of Contents

List of Figures

List of Tables

Acknowledgments

This dissertation summarizes years of learning and research, which would not have been possible without the support, motivation, and guidance received from several people. There are no proper words to convey my deep gratitude and respect for my parents because of their unconditional love and support. I would also like to thank my siblings, Ehsan, Arezoo, and Nazanin, for their support.

My sincere gratitude and appreciation to my advisor, Prof. Behrooz Mirafzal, for inspiring me to become a better researcher, and helping me to work on my weaknesses. His insightful feedback pushed me to sharpen my thinking and brought my work to a much higher level. I thank Prof. Mirafzal for the continuous support of my Ph.D. study and related research, for his patience, motivation, and immense knowledge. His guidance helped me in all the time of research and writing papers.

I would like to thank my Ph.D. committee members Dr. Anil Pahwa, Dr. Hongyu Wu, Dr. Warren N. White, and the outside chairperson of the examining committee, Dr. George Amariucai, for their effort and constructive feedback to improve this work.

I would like to express my heartfelt thanks to my former labmates Dr. Aswad Adib and Dr. Joseph Benzaquen, for always helping me to improve my research and kindly sharing their considerable technical skills with me. Also, a very special thanks to my current labmates at the Smart Power Electronics and Control Systems (SPECS) research group at Kansas State University, Mr. Fahmid Sadeque, Mr. Tareq Hossen, and Mr. Mehmetcan Gursoy, for all their support in enhancing this work. Their positive attitude has made our lab a great place to work.

Finally, my sincere thanks must also go to the faculty members of Electrical and Computer Engineering Department at Kansas State University who enriched my knowledge during the graduate courses. The administrative staffs in the department are memorable not only for their prompt support but also for always being nice.

Dedication

To my parents, of course.

Chapter 1

Introduction

The objective of this dissertation is to present novel approaches to improve the dynamic behavior of microgrids during abnormal conditions such as sudden load changes, loss of generation, and transitions between different modes of operation. This introductory chapter includes four sections. The motivation and objectives of this dissertation are outlined in Section 1.1. Subsequently, a review of the existing state-of-the-art solutions to achieve enhanced dynamics in microgrids is provided in Section 1.2. The main contributions of this dissertation are summarized in Section 1.3, while Section 1.4 briefly describes the organization of the dissertation.

1.1 Motivation and Objectives

Microgrids are becoming an important part of the energy infrastructure, representing a paradigm shift from remote central station power plants toward more localized distributed generation, especially in cities, communities and campuses. A microgrid is a small-scale electrical grid with its own power system that can operate separate, i.e., islanded, from or alongside the electrical grid, i.e., grid connected. The power to isolate from the larger grid makes microgrids resilient, and the ability to conduct parallel operations permits delivery of services that make the grid more competitive. By "islanding" from the grid during emer-

gencies, a microgrid can both continue serving its included load when the grid is down and serve its surrounding community by providing a platform to support critical services from hosting first responders and governmental functions to providing key services and emergency shelter. Microgrids provide low-cost clean energy, enhance local resiliency, and improve the operation and stability of the regional electric grid. The U.S. Department of Energy (DOE) Smart Grid R&D Program considers microgrids as a key building block for a smart grid and has established microgrid R&D as a key focus area.

Despite all the benefits that implementing microgrids bring to the electrical grid, low-inertia distributed generation (DG) units make microgrids vulnerable to the voltage and frequency fluctuations caused by abnormal conditions. The conversion of critical loads to smart loads is a potential solution for maintaining their desired voltage level, and consequently, improving the stability and power quality in microgrids. Besides, due to the voltage and frequency regulation by low-inertia DG units in islanded microgrids, it is necessary to employ effective control approaches to improve the dynamic performance of islanded microgrids during short-term voltage and frequency deviations, resulting in stability enhancement of overall system. To this end, the conventional control scheme of inverter-based DGs, e.g., photovoltaic (PV) units and battery energy storage systems (BESSs), can be modified in such a way to enable the microgrids to cope with abnormalities. Nevertheless, most of research studies on microgrids have been focused only on three-phase systems. However, over the past few years, there has been a huge rise in installation of rooftop PV panels and household BESSs at residential settings. Considering the fact that multiple houses are generally supplied by a single phase in residential applications, improving the dynamic performance of single-phase/residential microgrids deserves more attention.

1.1.1 Voltage and Power Fluctuation Issue in a Fleet of Nanogrids

Nanogrid is defined as a medium-to-low voltage power grid with a maximum consumption of a commercial building. In other words, nanogrid can be considered as a small-scale microgrid with the capability of operating in islanded mode. Implementation of a fleet of

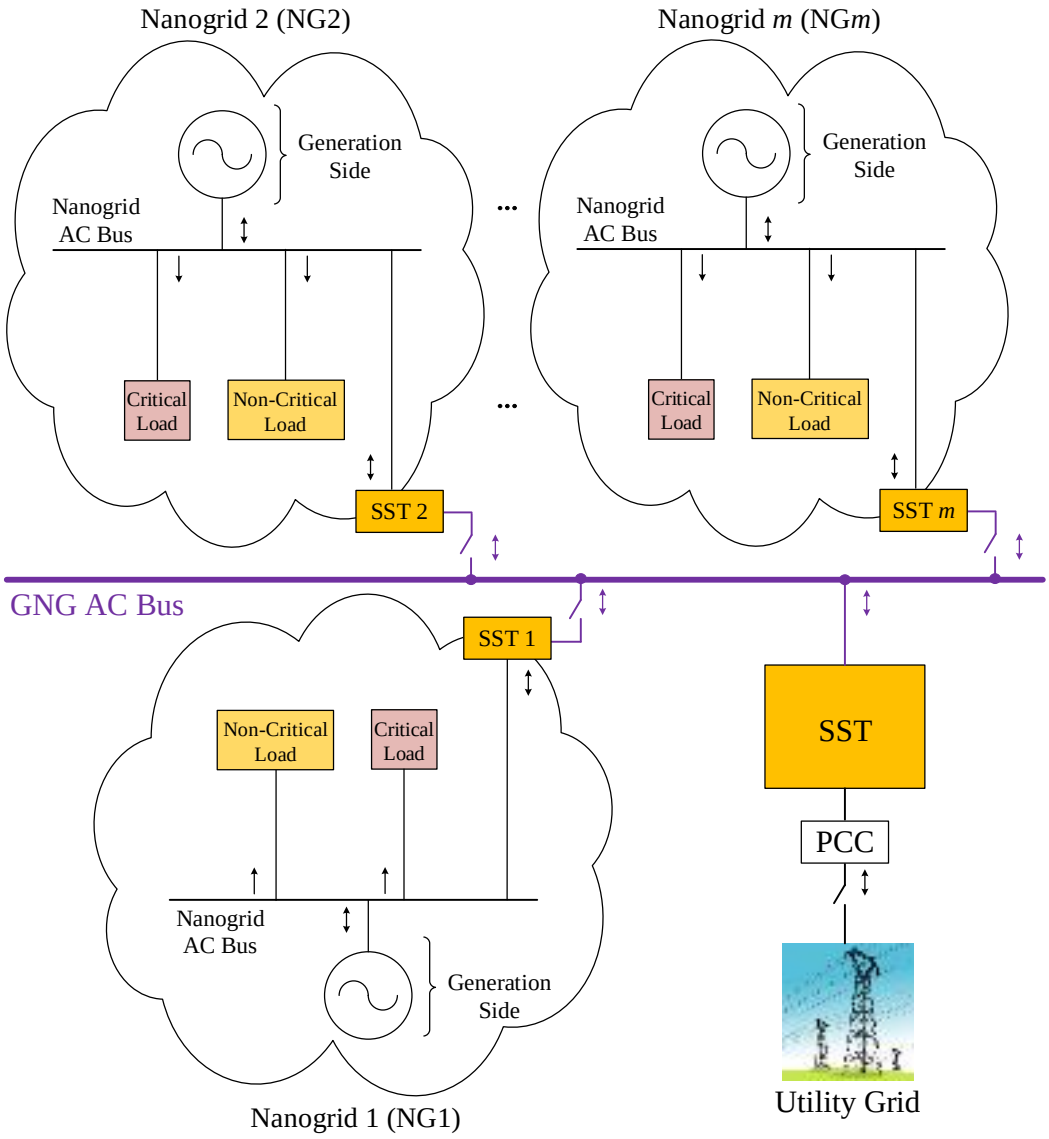

Figure 1.1: Grid of nanogrids (GNG) forming power systems of smart cities.

nanogrids, which is also referred as a grid of nanogrids (GNG), is a potential solution that will pave the way toward smart cities [1–3]. The traditional grid was not designed for high penetration of renewable energy resources with their reverse power flows, thus a traditional grid cannot appropriately accommodate the transformation from consumer to prosumer. Simply patching the traditional power system beyond its original design and safety margins will not alleviate the complications of power delivery congestion, reactive power support, feeder voltage regulation, and the other challenges of the way in which the grid is now being used. A potential solution is to separate the bulk power delivery from point of load

generation and control [4]. In a GNG, the loads and DG units are interconnected into a local power and energy system. Similar to the traditional microgrids, a GNG can operate in either grid-connected mode or off-grid mode known as islanded operation.

GNG has the potential for many technological benefits, but major limitations exist that prevent truly widespread adoption, especially the low inertia of DG units and highly fluctuating renewable energy generation which can lead to active and reactive power imbalances between generation and consumption in an islanded GNG. This results in voltage and power fluctuations which are not desirable, especially for the critical loads that require a well-regulated voltage, see Fig. 1.1. In a high-penetration PV scenario, the continuous fluctuation in PV generation presents considerable operational challenges for maintaining the power balance and stability in GNG [5–8]. Nanogrids are suffering from these fluctuations more than larger distributed generation systems due to their low inertia. Thus, it is necessary to explore innovative configurations and control schemes on demand side to avoid instability, and even improve the power quality [9, 10] of nanogrids.

1.1.2 Voltage and Frequency Fluctuation Issue in Islandeed Microgrids

Islanded microgrids are suffering from short-term voltage and frequency fluctuations caused by abnormal conditions such as sudden load changes, deviations of power generation, and transition from grid-connected to islanded mode of operation. This vulnerability to the transients is because of the voltage and frequency regulation by low-inertia power generation units in islanded microgrids. However, in grid-connected microgrids, due to the tight regulation of voltage and frequency by high-inertia utility grid, the dynamic behavior of the system is not a challenging issue. Therefore, it is necessary to employ effective control approaches to improve the dynamic performance of islanded microgrids during short-term voltage and frequency deviations, resulting in stability enhancement of overall system.

Islanded microgrids can be supplied by a combination of synchronous-based and inverter-based DG units, forming islanded mixed-inertia microgrids, see Fig. 1.2. Diesel generators as

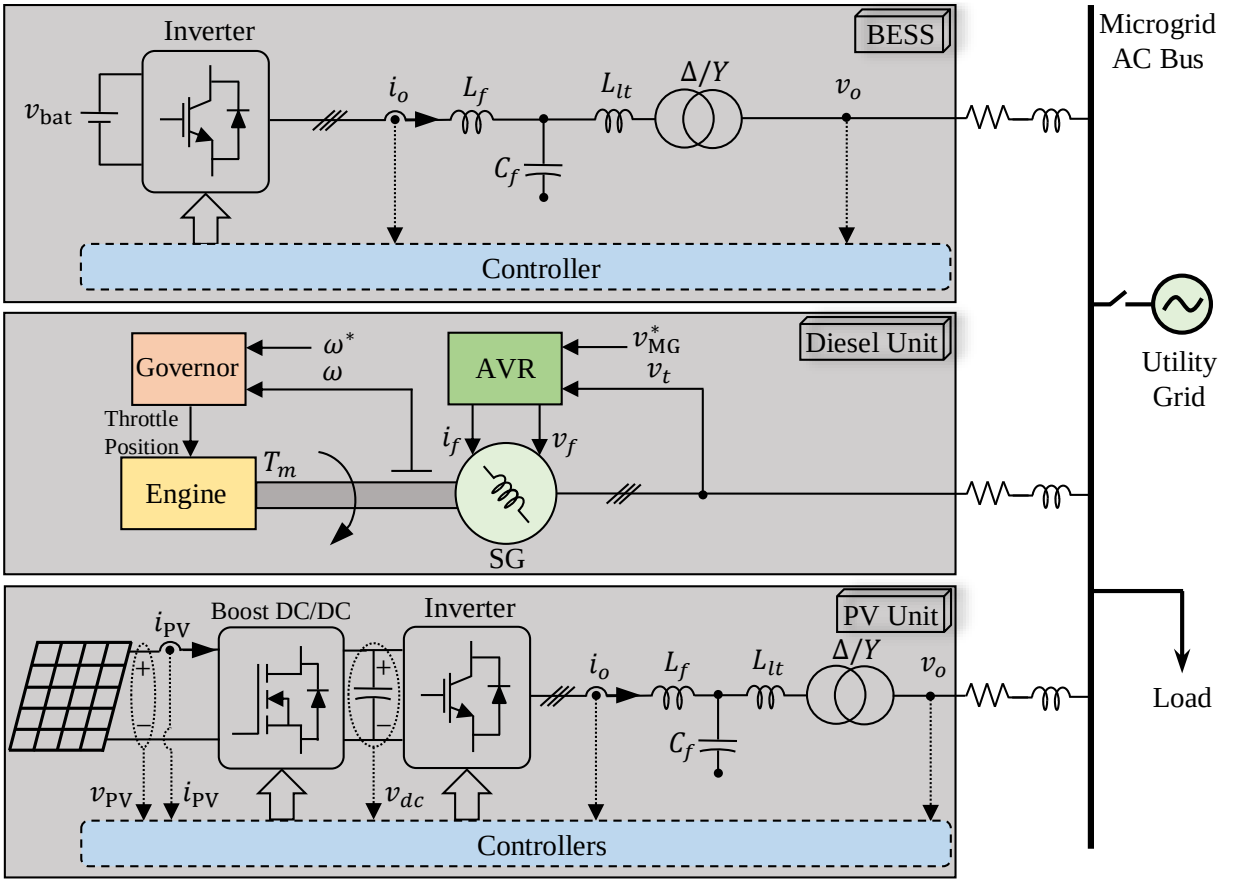

Figure 1.2: Configuration of an islanded mixed-inertia microgrid.

synchronous-based DGs have been widely used in islanded microgrids, especially in remote areas [11–13]. This extensive utilization of diesel generators is due to their low cost [14] and high reliability [15]. Typically, in the presence of diesel generators, inverter-based DGs are equipped with renewable energy resources, e.g. PV systems and wind turbines, to reduce the fuel consumption [16–18]. However, the unpredictable and stochastic output power of renewable energy resources has led to the implementation of BESSs to inject/absorb the deficit/extra power in real time. In such condition, the diesel generator operates in grid-forming mode by taking responsibility for controlling the voltage and frequency of ac bus using an automatic voltage regulator (AVR) and governor, respectively. On the other hand, in order to take the full advantage of clean and inexhaustible solar energy, the PV units are traditionally operating in active and reactive power *(PQ)* control mode, which is also referred as grid-following mode, in which the reactive power, i.e., Q, is typically set to zero

to achieve a unity power factor [19–22].

A central energy management system (EMS) is utilized in islanded microgrids to achieve a coordinated operation between paralleled inverter-based and synchronous-based DGs. The central EMS allows prompt operation of islanded microgrids by supervising the power flow and maintaining a balance between load demand and power generation [23]. However, the conventional EMSs provide a coordinated load sharing between DG units mainly during the steady-state condition, whereas significant inertia difference between inverter-based and synchronous-based DGs causes different dynamic responses in islanded microgrids. This leads to instantaneous power imbalance between generation and consumption during abnormalities, resulting in short-term voltage and frequency fluctuations. As a result, according to IEEE standard 1547-2018 [24], the system can experience a blackout if these voltage or frequency oscillations surpass the permissible limits. This necessitates the deployment of traditional controllers of DGs in order to participate in mitigating the short-term voltage and frequency fluctuations.

1.1.3 Power Imbalance Issue in Isolated Single-Phase Feeders at Distribution Level

Although microgrids have been the center of attention during the last few years, most of research studies on microgrids have been focused only on three-phase systems [22, 25], and the single-phase/residential microgrids have not been regarded enough. Considering the fact that most individual residences in North America are using single-phase feeders at distribution level, the concept of single-phase/residential microgrid deserves more attention, see Fig. 1.3. The residential microgrid can be considered as a group of houses which are equipped with rooftop PV panels and household BESSs connected to their respective phase with the ability of operating in both grid-connected and islanded modes [26]. The DG units are traditionally operating in PQ control mode, i.e., grid-following mode, when the residential micogrid is connected to the main grid [21]. On the other hand, during islanded mode of operation, DG units are responsible for regulating the voltage and frequency (vf)

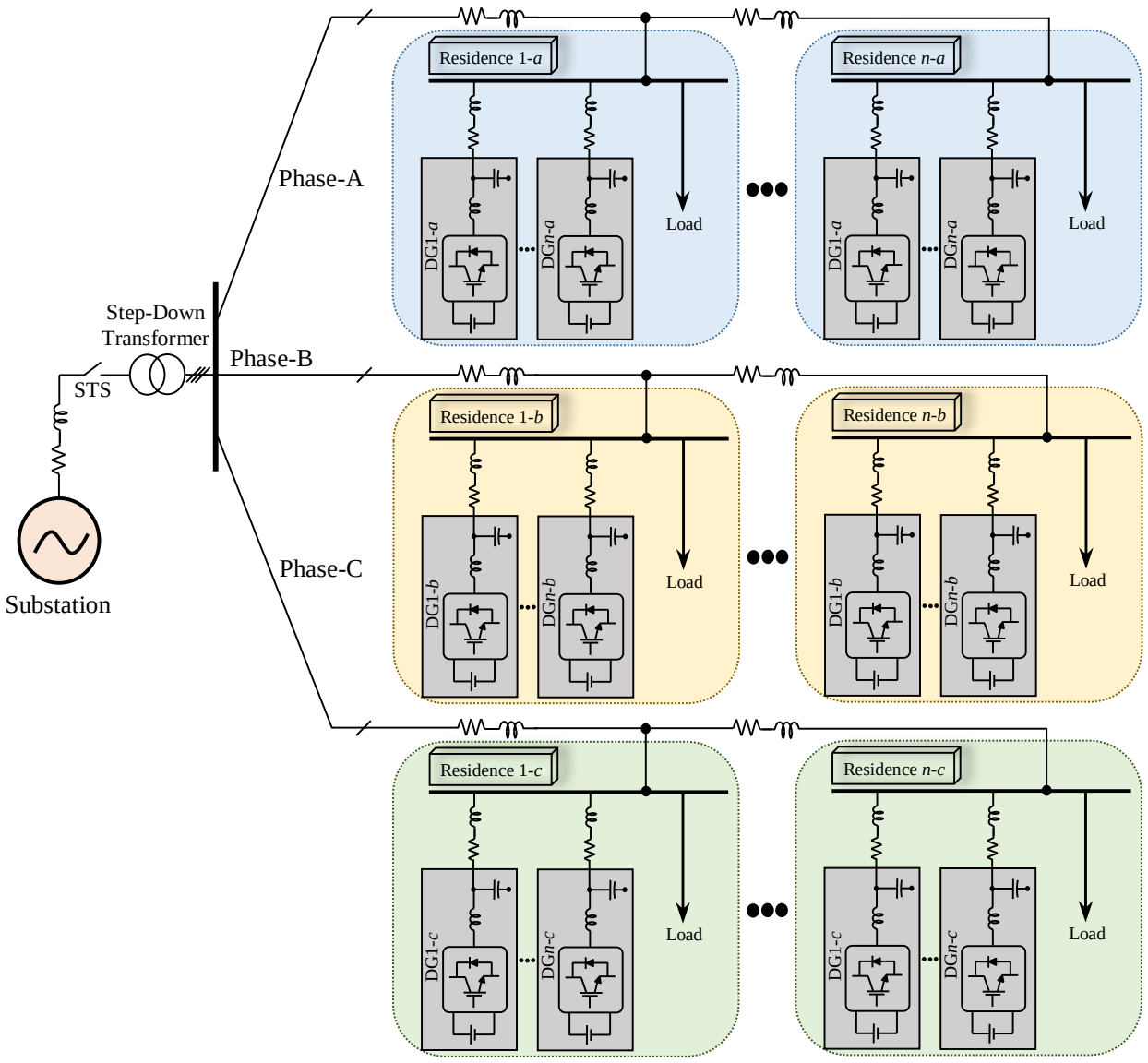

Figure 1.3: Schematic of residential microgrid at distribution level.

of the system, i.e., grid-forming mode. Thus, depending on the operation mode of the system, i.e., grid connected or islanded, the DG units typically transfer between PQ (or grid following) and vf (or grid forming) control modes. During transitions between grid-connected and islanded operations, any mismatch between magnitude and frequency of grid-side and microgrid-side voltages can lead to large transients across the household loads. Thus, it is necessary to implement a mechanism to achieve seamless transitions between these two modes of operation.

During islanded mode, the DG units start maintaining the voltage and frequency of local

loads based on their predefined droop characteristics. Due to the predominancy of resistive lines in distribution systems [27], it is preferable to utilize the inverse/reverse droops, i.e., *P-v* and *Q-f*, in order to avoid the poor performance of traditional droop control, i.e., *P-f* and *Q-v*. On the other hand, multiple inverter-based DG units are typically connected to their respective phase at residential level. However, during islanded mode, there should be some connections between different phases in order to ensure the balance between generation and consumption within all three phases. This situation calls for new challenges to achieve a seamless transition while interconnecting all three single-phase feeders which have not yet been addressed.

1.2 Literature Review

This section presents a review of the existing state-of-the-art solutions to address the abovementioned challenges in section 1.1.

1.2.1 Power Conditioning Units in Transmission and Distribution Systems

Several solutions have been presented in literature to resolve the power and voltage variation issues and improve the power quality in power systems in general and GNG. To this end, parallel, series, and parallel-series compensators have been widely used in the last two decades [28, 29]. Static synchronous compensator (STATCOM) [30] and synchronous series compensator (SSSC) [31] are examples of these compensators. The main objective of employing STATCOM at transmission systems is to regulate the voltage by injecting/absorbing reactive power. The STATCOM is a parallel-connected power-electronics based infrastructure, whereas the SSSC is connected in series with the transmission line, and this can be considered as the main difference between STATCOM and SSSC. The solid-state transformer (SST) with the capability of providing ancillary services for the distribution system has been proposed as a replacement for traditional power transformers [32, 33]. Tha main

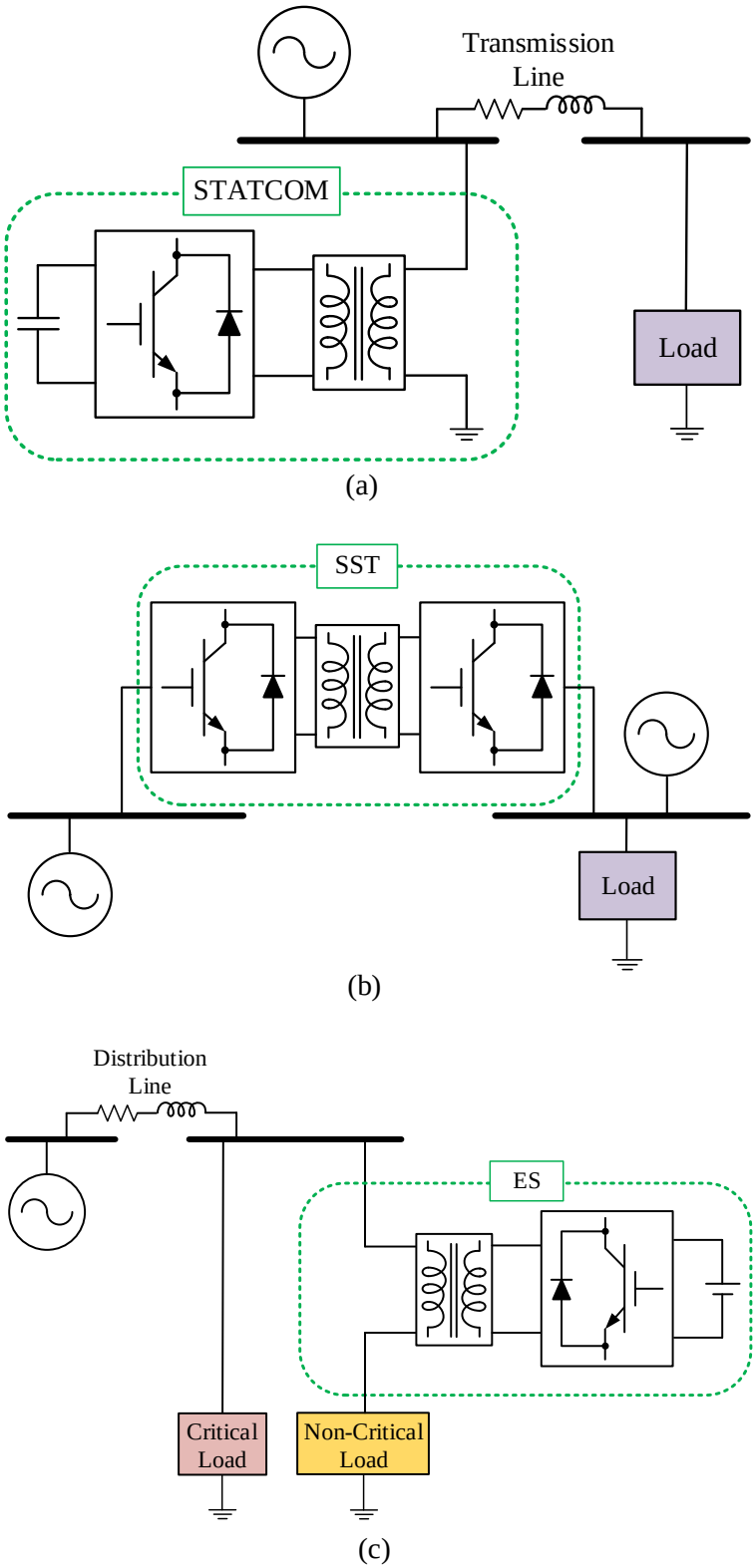

Figure 1.4: Comparison between overall configuration of (a) STATCOM, (b) SST, and (c) ES as conventional power conditioning units.

objective of SST is to regulate the ac-bus voltage of downstream power network. On the other hand, in order to shift some of power dispatching issues from generation side to demand side, the concept of smart loads has recently received wide attention. The work in [34] develops a configuration for smart loads by connecting an electric spring (ES) in series with non-critical load, i.e., a load or cluster of loads which can tolerate high voltage variation, to provide voltage support at the point of common coupling (PCC). In other words, ES passes some fluctuations associated with DG units to non-critical loads to provide a well-regulated voltage for critical loads. Fig. 1.4 provides a comparison between overall configuration of STATCOM, SST, and ES.

Another configuration of smart loads is proposed in [35] using ac drives to provide power and frequency support for the network. The other developments of smart loads mostly focus on introducing novel approaches to adjust the loads in order to achieve a continuous power balance between generation side and demand side. In [36], droop-based smart loads are utilized to autonomously manage the load demand without a need for communication systems. A neural network load estimator is used in [37] to develop a mathematical model for smart loads and integrate it into a microgrid EMS. Furthermore, the electric vehicle charging stations are mathematically modeled as smart loads in [38]. The study in [39] investigates the benefits of smart loads in an industrial microgrid to minimize the required energy storage system.

1.2.2 Dynamic-Response Enhancement in Islanded Microgrids

A number of previous studies have been focused on the voltage and/or frequency support in islanded microgrids. In [40–42], an enhanced frequency response is achieved by coordinating the operation of DG units. However, implementing a coordinated control algorithm increases the complexity and communication requirements of the system. Ref. [43] and [44] utilize BESS for frequency regulation and stability improvement of islanded microgrids by optimizing the size of BESS and employing virtual inertia, respectively. On the other hand, considering the system cost, different control methods are presented in [45, 46] using PV

units instead of BESS for reducing the frequency deviations. However, the control strategies developed in [45, 46] are not applicable when the load demand is higher than power generation. Moreover, an approach is presented in [47] which reduces the dependency of islanded microgrids on BESS by controlling the frequency through voltage regulation.

Nevertheless, the abovementioned methods in [40–47] focus only on frequency regulation of the system. However, maintaining the ac-bus voltage within acceptable limits is essential for improving the stability, reliability, and power quality of the system, especially in the presence of critical loads [48]. In [49], an enhanced voltage profile is achieved by synchronizing the response times of different voltage regulation devices employed in an islanded microgrid. The network theory concepts are utilized in [50] to develop a control scheme for mitigating the voltage fluctuations of ac bus in islanded microgrids. In [51] and [52], the voltage and frequency of the system are controlled by BESS instead of diesel generator. However, due to the low inertia of BESS, this might lead to stability deterioration of the system. The proposed method in [53] coordinates the distributed controllers of an islanded microgrid to improve the voltage and frequency responses during abnormal conditions. However, based on the presented results, the proposed control strategy deteriorates the frequency response of the system during the transition from islanded to grid-connected mode.

1.2.3 Seamless Transitions in Residential Microgrids

Although various studies have been focused on different aspects of performance improvement in residential microgrids such as power management [54], harmonic compensation [55], voltage regulation [56], and reactive power compensation [57], only a few have addressed the challenge of achieving seamless transitions between different operation modes. Nevertheless, the proposed solutions in literature to achieve seamless transitions between operation modes can be divided into three main categories. The first category implements control algorithms into the primary control loops of DG units to cope with transients caused by transitions between modes of operation [58–60]. However, due to the parallel connection of multiple inverters in microgrids, employing complex control algorithms at primary control level with-

out any coordination between inverters can lead to stability issues. The second category utilizes hierarchical control schemes to achieve seamless mode-transition capability [61–65]. The third category employs multiagent technology for a seamless transition between grid-connected and islanded modes [66–68]. Although multiagent systems reduce the dependency on communication links, coordinating agents is always a complex process.

At distribution level, each single-phase feeder can be isolated and operate as an islanded microgrid after the loss of utility grid only if there are enough DG units in each phase. During islanded mode, the conventional droop characteristics, i.e., P-f and Q-v, are typically implemented which assume the lines are inductive [69–71]. However, for low-voltage distribution systems where the R/X ratio of feeders is high, the P-v and Q-f droops can be used for enhanced controllability [72]. Interphase ac-ac converters have been suggested to be placed between islanded single-phase feeders for power flow control between the feeders, while the three single-phase feeders can remain in their original abc-sequence with 120 degrees phase-shift with respect to each other [26, 73]. Instead of ac-ac converters to control the power flow between the feeders, employing a tertiary control scheme in smart inverters [74–78] can eliminate the need for adding any interphase power processing device. The tertiary control of microgrids can be achieved by centralized or decentralized methods.

1.3 Contributions of the Dissertation

This section summarizes the main contributions of this dissertation in improving the dynamic behavior of microgrids during abnormal conditions.

A new configuration and control scheme for smart loads is presented in this dissertation to cope with voltage and power fluctuations in a fleet of nanogrids. The proposed configuration is obtained via series connection of a three-phase electric damper (ED) with critical load, developing a smart critical load (SCL). The ED decouples the critical load from ac bus and consists of a small battery, an inverter, and isolation transformer. In this way, instead of controlling the ac-bus voltage, each ED is only responsible for regulating its respective critical load voltage at desired level. Therefore, smaller battery energy storage can be utilized in the

proposed SCL configuration, resulting in significant cost reduction. On the other hand, due to the utilization of an inverter with short-time response in SCL configuration, dynamics of SCLs are taken into account in small-signal stability analysis of overall system. To this end, a systematic approach is presented to model the proposed three-phase SCLs considering the switching states of ED's inverter.

In this dissertation, the dynamic behavior of islanded microgrids is improved by mitigating the short-term voltage and frequency fluctuations. For this purpose, the BESS with fast response is used to inject/absorb the active and reactive power during abnormal conditions. A piecewise linear-elliptic (PLE) active power-frequency, i.e., *P-f*, droop is proposed for BESS which improves the frequency response of the system. Similarly, in order to enhance the voltage profile of the system, a PLE reactive power-voltage, i.e., *Q-v*, droop is introduced. Furthermore, it is demonstrated that for any linear droop characteristic with a specified droop coefficient, there is also a PLE droop which can be formulated using the proposed method in this dissertation. Compared with conventional linear droops, employing the proposed PLE droops results in injecting/absorbing more active and reactive power by BESS to compensate for the instantaneous power imbalance between supply and demand during abnormal conditions. This leads to stability enhancement and dynamic-performance improvement of the system.

Another approach for improving the dynamics of islanded microgrids is presented in this dissertation using PV units instead of BESS. For this purpose, the PV units are utilized to cope with the instantaneous power imbalance between supply and demand during abnormal conditions. An adaptive piecewise droop (APD) characteristic is proposed for PV units which increases/decreases their predefined active-power setpoint during abnormalities, leading to an improved frequency response. Besides, a droop characteristic is implemented in reactive-power control loop of PV units in order to enable them to participate in voltage regulation of the system during abnormal conditions. Considering the fact that the conventional operation mode of PV units, i.e., *PQ* control mode, is independent of voltage and frequency variations, equipping PV units with the proposed droops results in an enhanced dynamic response. This leads to stability improvement and dynamic-response enhancement of the system.

Due to the posibility of having power imbalance within the phases of an islanded residential community, an approach for seamless interconnection of three isolated single-phase feeders at distribution level is proposed in this dissertation. In other words, the proposed method discusses a solution to seamlessly form a unified single-phase residential microgrid, and avoid voltage drop and frequency fluctuation across household loads by maintaining power balance within all three phases. To this end, a new operation mode is defined for the case all three single-phase feeders are interconnected, which is called inter-phase connected mode. Hence, three operation modes are considered for the residential community: grid connected, islanded, and inter-phase connected. A seamless transition algorithm is presented which monitors the system condition in real time, and sends commands to static transfer switches (STSs) accordingly in order to enable the residential community to transfer between different operations modes seamlessly. Moreover, after resolving the abnormal conditions on the grid side, the residential community is seamlessly reconnected to the main grid, i.e., grid-connected mode.

The main contributions of this dissertation can be summarized as follows:

- Development of a new configuration and control scheme for smart loads via series connection of EDs with critical loads to cope with short-term voltage and power transients in a fleet of nanogrids.

- Development of a detailed small-signal state-space model for analyzing the stability of proposed smart loads by taking into account the switching process of three-phase inverter.

- Proposing PLE droops for BESS to participate in mitigation of short-term voltage and frequency fluctuations in islanded mixed-inertia microgrids.

- Development of the control scheme of PV units to participate in mitigation of short-term voltage and frequency fluctuations in islanded mixed-inertia microgrids.

- Forming an islanded single-phase microgrid from three isolated single-phase feeders at distribution level to cope with power imbalance inside the feedres.

1.4 Organization of the Dissertation

Besides this introductory chapter, the remainder of this dissertation is organized as follows:

Chapter 2 presents a new configuration for smart loads in a fleet of nanogrids to mitigate the voltage and power fluctuations of critical loads during abnormal grid conditions, sudden load changes, and fluctuations in PV ambient condition. The operational performance of nanogrids with and without the proposed smart loads are compared; the results demonstrate significant improvement in power quality of nanogrids when incorporating the proposed smart loads. A detailed small-signal state-space model is derived for the proposed smart loads considering the switching process of three-phase inverter. This model is then used to investigate the location of eigenvalues due to the changes in different parameters of smart load to demonstrate the stability region and robustness of the proposed smart loads configuration. Moreover, it is demonstrated that the suggested smart loads configuration can be an effective solution to improve the size and lifetime of central battery bank. Several case studies are carried out to validate the effectiveness of the proposed smart loads in small-scale microgrids known as nanogrids featuring lower inertia.

Chapter 3 investigates the cooperative role of BESS and PV units in improving the dynamic behavior of islanded microgrids during abnormal conditions. For this purpose, two PLE droops, i.e., P-f and Q-v, are proposed for BESS to mitigate the voltage and frequency variations during abnormalities. Compared with linear droop characteristics, significant mitigation in voltage and frequency fluctuations is achieved, when the BESS is equipped with the proposed PLE droop characteristics. Furtheremore, the conventional controller of PV units is deployed to enhance the dynamic response of islanded microgrids by mitigating the short-term voltage and frequency fluctuations. Different case studies are performed to confirm the effectiveness and superiority of proposed methods in dynamic-performance improvement of islanded microgrids.

In Chapter 4, an approach is presented for solving the power imbalance issue in isolated single-phase feeders at distribution level. To this end, the proposed method enables seamless

interconnection of all three phases of residential microgrid during islanded mode. This leads to supplying the local loads in all three phases at their desired voltage level. On the other hand, after resolving the abnormal condition on the grid side, the residential microgrid is reconnected to the utility grid seamlessly. Employing the proposed approach ensures the stable operation of DG units during transitions, while the power quality is improved significantly. A seamless transition algorithm is introduced which monitors the system condition in real time and sends appropriate signal commands to the STSs in order to ensure seamless transitions. Different case studies are carried out to validate the viability of proposed method in achieving seamless transitions in residential microgrids.

A summary of the presented research in this dissertation along with the contributions to the state-of-the-art regarding dynamic-behavior improvement of microgrids during abnormal conditions is presented in Chapter 5. In addition, suggestions are given for future work on developing the controllers of inverter-based DG units and turning their inverters into smart inverters in order to cope with fast transients.

Chapter 2

Improved Dynamics in a Fleet of Nanogrids

This chapter investigates the effects of utilizing smart loads on the performance of nanogrids. Low-inertia power generation units make nanogrids vulnerable to the voltage and power fluctuations caused by pulse loads and abnormal grid conditions. The conversion of critical loads to smart loads is a potential solution for improving the stability and power quality in nanogrids. A smart load can compensate for sudden deviations between supply and demand, and therefore, can mitigate voltage and power oscillations in low-inertia nanogrids. The conversion of critical loads to smart loads can reduce the stress on energy storage units and minimize the required battery banks in nanogrids. In this dissertation, several case studies are considered to verify the stability and power quality improvement of nanogrids when some loads are converted to smart loads.

The contents of this chapter are organized into seven sections. Section 2.1 provides a comparison between the overall configuration of proposed smart load and the existing power conditioning units in power systems. A general overview of the GNG under study equipped with proposed smart loads is presented in Section 2.2. The proposed control scheme for smart loads is explained in detail in Section 2.3. Subsequently, the stability of smart loads is analyzed in Section 2.4 by developing their small-signal state-space models end performing

the eigenvalue analysis. In addition, Section 2.5 demonstrates the effectiveness of employing smart loads in increasing the lifetime and decreasing the size of central battery banks which are utilized on the generation side of nanogrids. Case study results are provided in Section 2.6 to verify the merits of proposed configuration and control scheme for smart load. Lastly, Section 2.7 concludes this chapter.

2.1 Proposed Smart Load vs. Other Power Conditioning Units

This section compares the overall configuration of proposed SCL with some other conventional power conditioning units in power systems, i.e., STATCOM, SST, and ES. This proposed configuration is obtained via a series connection of a three-phase voltage compensator, which is also referred as an ED, with the critical load to develop a SCL. As can be found from Fig. 2.1(a), the STATCOM is commonly allocated at transmission level to regulate the ac-bus voltage by controlling the reactive power from the upstream power network. However, the proposed SCL shown in Fig. 2.1(d) is installed at the point of load to compensate the short-term active and reactive power imbalances for critical loads in real time, thus enhancing the controllability of loads in critical infrastructure. The three-stage SST shown in Fig. 2.1(b) is connected between the medium voltage (MV) and low voltage (LV) distribution networks, which can have advanced control and communication capabilities [79, 80]. Thus, the SST decouples the MV and LV networks, while controlling the ac-bus voltage of LV downstream network. In contrast, the ED in SCL configuration is connected between the critical load and the ac bus regulating the critical load voltage.

The ES shown in Fig. 2.1(c) has recently been utilized in distribution systems for demand-side management [34, 82, 83]. ES is a voltage compensator connected in series with the non-critical load to regulate the ac-bus voltage while reshaping the load demand (load shedding). In other words, the ES passes the fluctuations of renewable energy resources to the non-critical loads by allowing their power consumption to vary. However, since the voltage

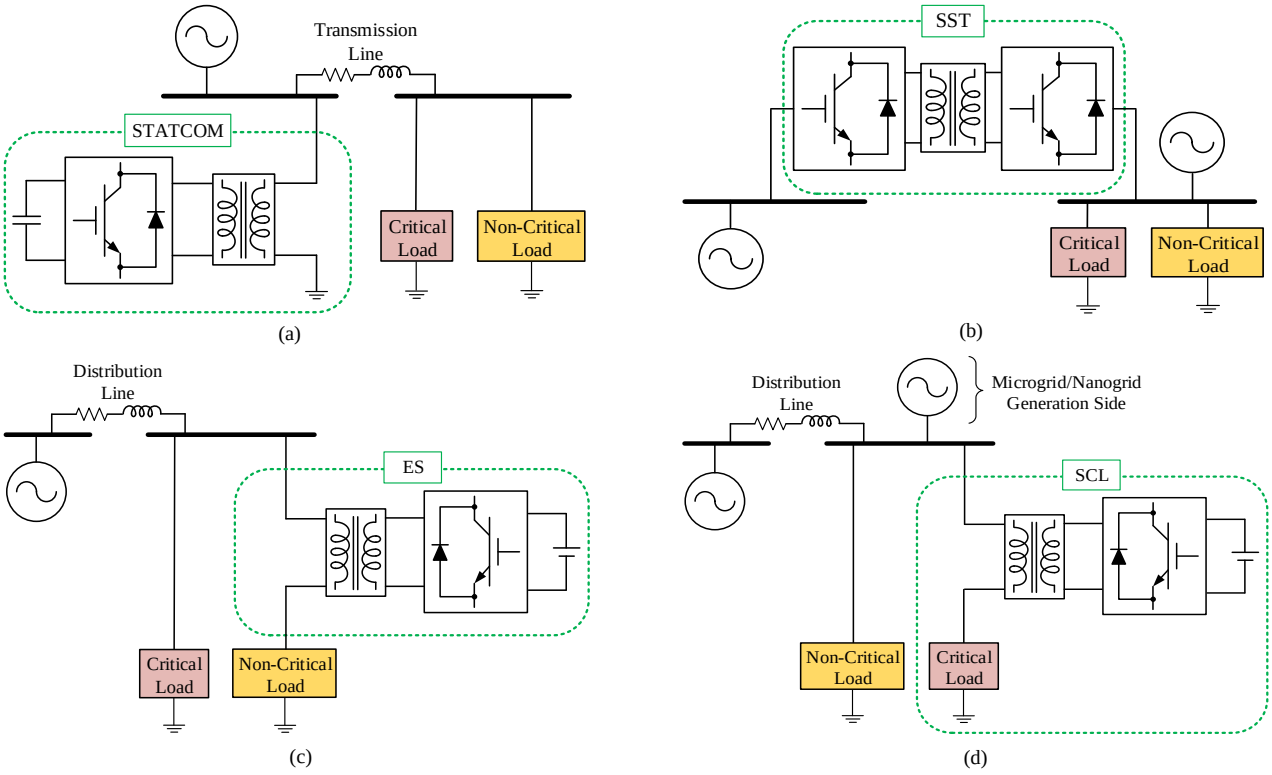

Figure 2.1: SCL versus other power conditioning units in power systems. (a) STATCOM. (b) SST. (c) ES. (d) SCL [48, 81].

variations across the non-critical load should not exceed ±20% [84], the operation range of ES is limited [85]. In order to resolve this issue, in [86], another configuration is introduced for ES which operates independently without direct interaction with the non-critical load. In high-penetrated PV nanogrids, the ES's battery is under severe stress while constantly charges and discharges to regulate the fluctuating ac-bus voltage [87]. This results in a significant reduction in battery lifetime and limited operation range for ES. However, for the idea presented in this work, considering the fact that the demand side is typically a mixture of multiple critical and non-critical loads, each ED in the proposed SCL configuration is only responsible for regulating the associated critical load voltage instead of the ac-bus voltage. This leads to lower discharge rate and lifetime improvement of ED's battery while mitigating the short-term voltage and power fluctuations of critical load.

2.2 Grid of Nanogrids (GNG) Equipped with Smart Loads

The schematic of GNG formed by a fleet of nanogrids is shown in Fig. 2.2. Each nanogrid consists of different energy resources, e.g., diesel generators, PVs, central battery bank, power electronics interfaces (PEIs), SCLs, and non-critical loads. Each SCL consists of an ED connected in series with a critical load to regulate its voltage. All nanogrids are connected to the main ac bus through SSTs, which can facilitate bidirectional power flow capability among nanogrids. The operator is capable of disconnecting nanogrids from GNG, i.e., islanded mode, or reconnecting them to GNG, i.e., GNG-connected mode. An SST is also used at PCC between GNG and the main utility grid. The GNG is able to interact with the main utility grid by injecting/absorbing power and providing ancillary services in grid-connected mode. A circuit breaker at PCC enables GNG to get isolated from the grid in case of abnormal conditions such as utility power outage. The utilization of SCLs plays an important role in improving the stability and power quality of islanded GNG, as the main grid is no longer available to compensate for the potential power imbalances.

The equivalent block diagram of each nanogrid is illustrated in Fig. 2.3. In order to balance the power supply and demand in the GNG-connected mode, the following criteria should always be satisfied:

$$P_{\text{gen}} + P_{\text{GNG}} = P_{\text{NCL}} + \sum_{i=1}^{n} P_{\text{SCL}i}, \tag{2.1}$$

$$Q_{\text{gen}} + Q_{\text{GNG}} = Q_{\text{NCL}} + \sum_{i=1}^{n} Q_{\text{SCL}i}, \tag{2.2}$$

where n is the number of interconnected SCLs in nanogrid. P_{gen} and Q_{gen} are the active and reactive power delivered by generation side, while P_{GNG} and Q_{GNG} are the active and reactive power injected/absorbed by GNG. The active and reactive power demand of non-critical load are denoted as P_{NCL} and Q_{NCL}. Besides, $P_{\text{SCL}i}$ and $Q_{\text{SCL}i}$ are the active and

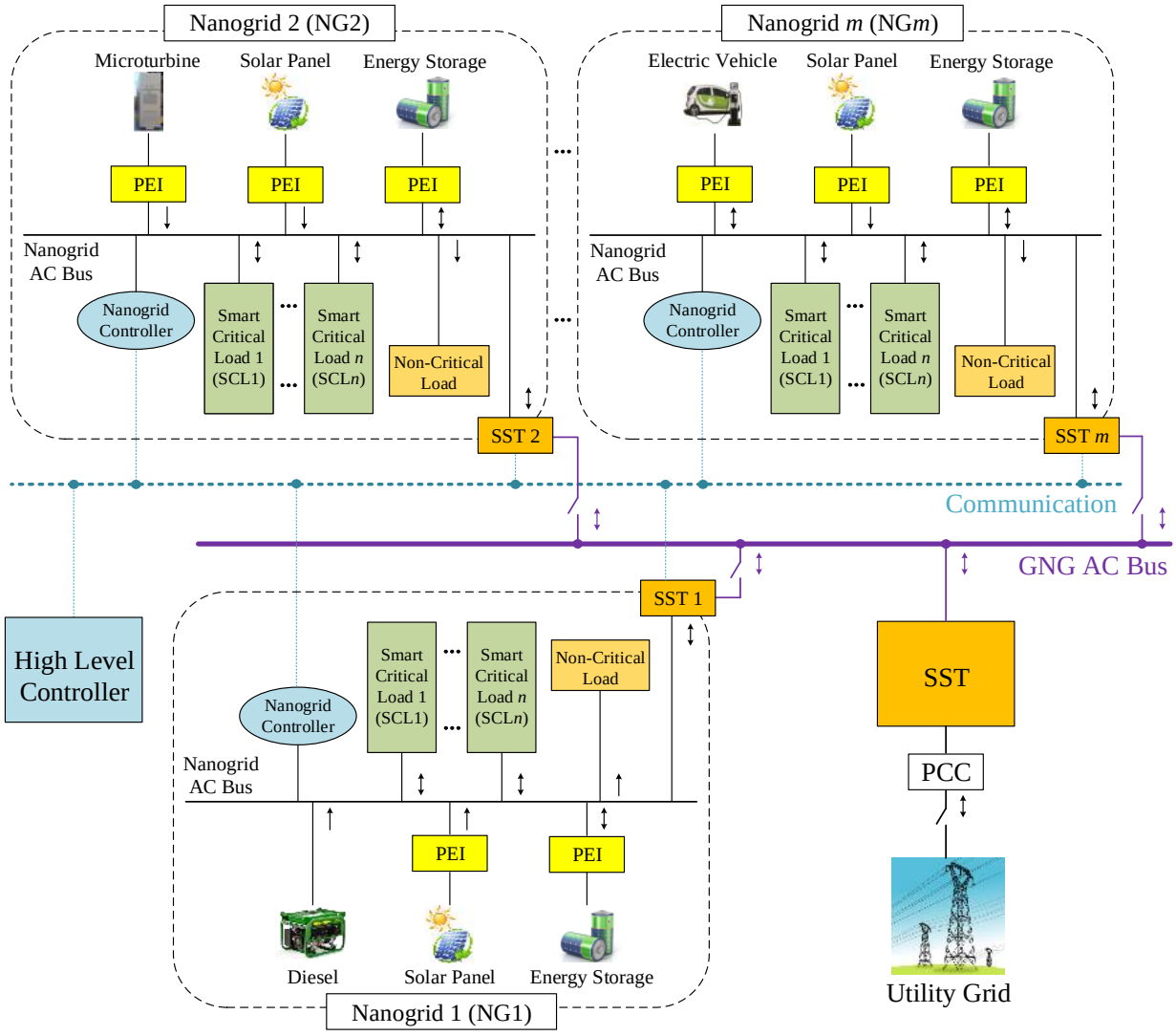

Figure 2.2: Grid of nanogrids (GNG) equipped with smart loads [48].

reactive power of ith SCL, which can be obtained as follows:

$$P_{\mathrm{SCL}i} = P_{\mathrm{CL}i} \pm P_{\mathrm{ED}i}, \tag{2.3}$$

$$Q_{\mathrm{SCL}i} = Q_{\mathrm{CL}i} \pm Q_{\mathrm{ED}i}, \tag{2.4}$$

where $P_{\mathrm{CL}i}$ and $Q_{\mathrm{CL}i}$ are the active and reactive power of ith critical load. The injected/absorbed active and reactive power by ith ED are $P_{\mathrm{ED}i}$ and $Q_{\mathrm{ED}i}$. According to (2.1), (2.2), (2.3), and (2.4), a balanced nanogrid should follow the below criteria:

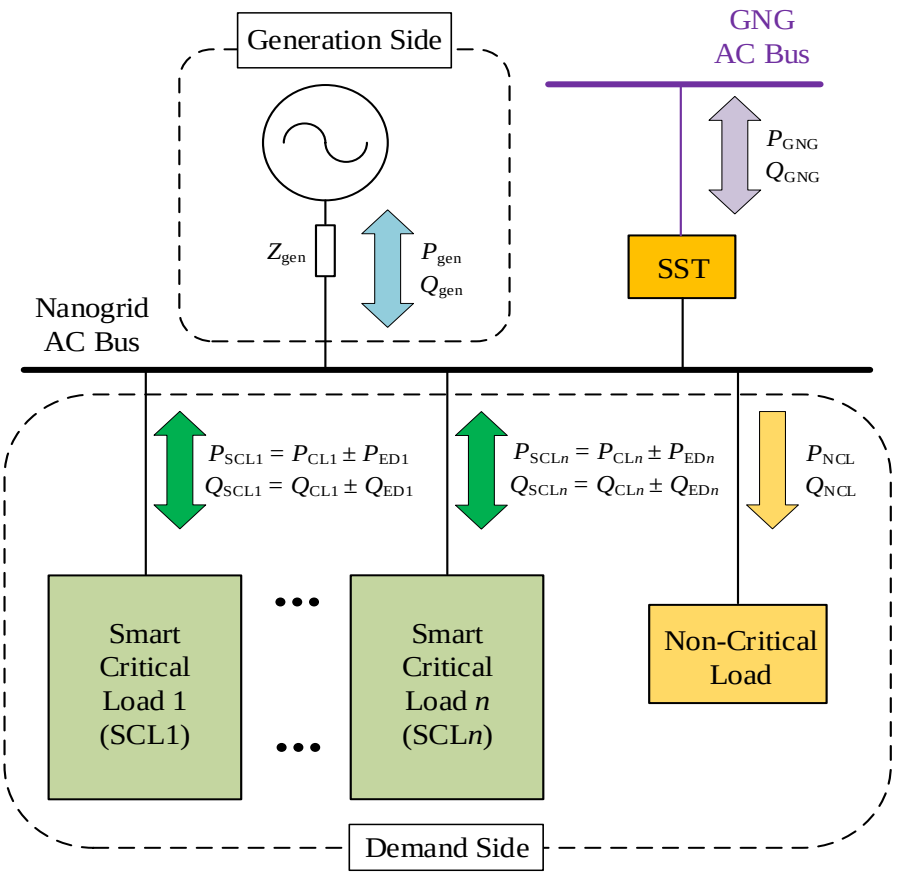

Figure 2.3: Equivalent block diagram of each nanogrid [48].

$$P_{\text{gen}} + P_{\text{GNG}} = P_{\text{NCL}} + \sum_{i=1}^{n} P_{\text{CL}i} \pm \sum_{i=1}^{n} P_{\text{ED}i} \; = P_{\text{L}} \pm \sum_{i=1}^{n} P_{\text{ED}i}, \tag{2.5}$$

$$Q_{\text{gen}} + Q_{\text{GNG}} = Q_{\text{NCL}} + \sum_{i=1}^{n} Q_{\text{CL}i} \pm \sum_{i=1}^{n} Q_{\text{ED}i} \; = Q_{\text{L}} \pm \sum_{i=1}^{n} Q_{\text{ED}i}, \tag{2.6}$$

where P_{L} and Q_{L} are the total active and reactive power demand, including both critical and non-critical loads. For an islanded nanogrid, P_{GNG} and Q_{GNG} are zero. Herein, SCLs are capable of acting as active and reactive power compensators in case of having short-term power imbalances in the system.

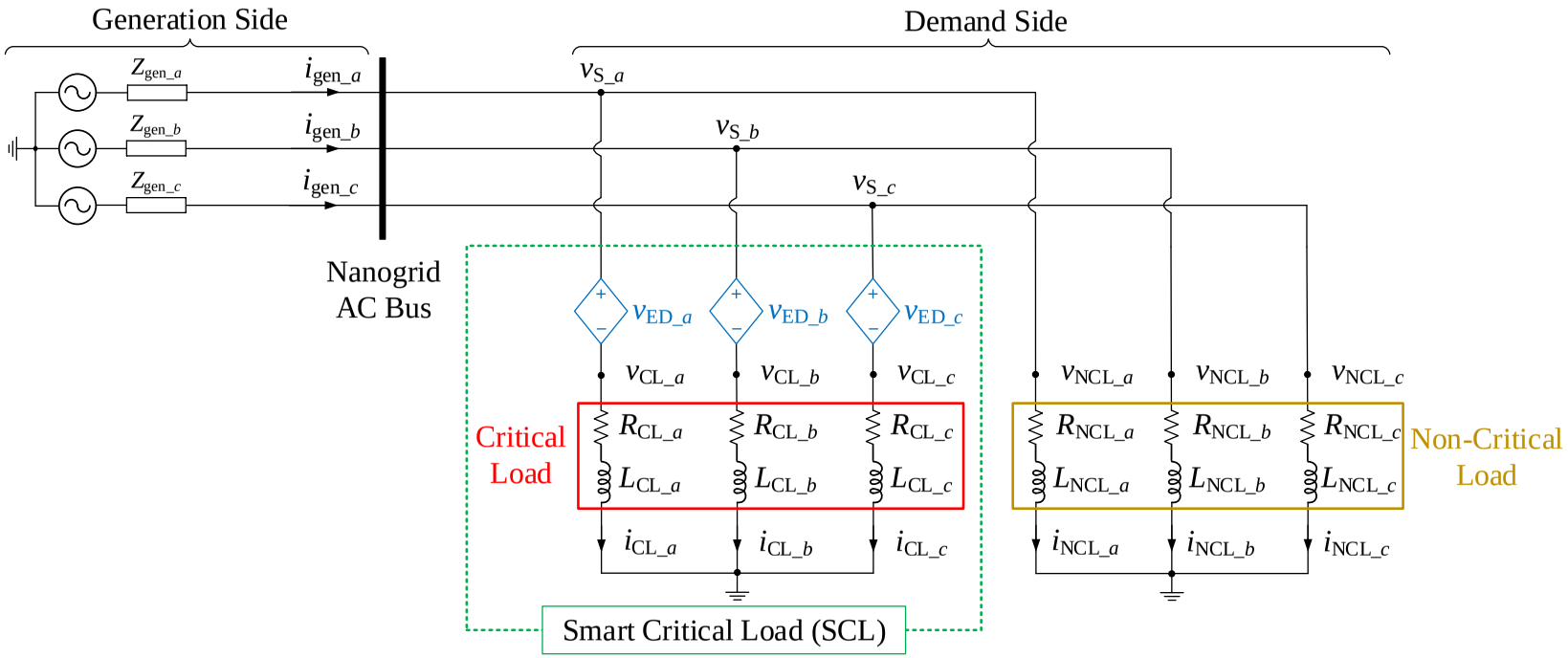

Figure 2.4: Simplified electrical diagram of each nanogrid with implementation of one SCL [48, 81].

2.3 Control Scheme of Smart Loads

The simplified electrical diagram of each nanogrid with only one SCL is shown in Fig. 2.4. In the proposed SCL configuration, the secondary side of ED's isolation transformer is connected in series with the critical load. The three-phase ED is controlled to regulate the critical load voltage, and consequently, produce the active ($\pm P_{\mathrm{ED}}$) and reactive ($\pm Q_{\mathrm{ED}}$) power differences between generation side and load demand. Therefore, voltage and power fluctuations of critical loads can be mitigated using three-phase EDs.

The line-to-line output voltages of ED, i.e., $v_{\mathrm{ED\_}ab}$, $v_{\mathrm{ED\_}bc}$, and $v_{\mathrm{ED\_}ca}$, are given by:

$$\begin{bmatrix} v_{\mathrm{ED\_}ab} \\ v_{\mathrm{ED\_}bc} \\ v_{\mathrm{ED\_}ca} \end{bmatrix} = \begin{bmatrix} v_{\mathrm{S\_}ab} \\ v_{\mathrm{S\_}bc} \\ v_{\mathrm{S\_}ca} \end{bmatrix} - \begin{bmatrix} v_{\mathrm{CL\_}ab} \\ v_{\mathrm{CL\_}bc} \\ v_{\mathrm{CL\_}ca} \end{bmatrix}, \tag{2.7}$$

where $v_{\mathrm{S\_}ab}$, $v_{\mathrm{S\_}bc}$, and $v_{\mathrm{S\_}ca}$ are line-to-line voltages of nanogrid ac bus, and $v_{\mathrm{CL\_}ab}$, $v_{\mathrm{CL\_}bc}$, and $v_{\mathrm{CL\_}ca}$ are line-to-line voltages of critical load.

For a resistive-inductive (RL) load, the ED output voltage in (2.7) can be rewritten as:

$$\begin{aligned} \begin{bmatrix} v_{\mathrm{ED\_}ab} \\ v_{\mathrm{ED\_}bc} \\ v_{\mathrm{ED\_}ca} \end{bmatrix} = & \begin{bmatrix} v_{\mathrm{S\_}ab} \\ v_{\mathrm{S\_}bc} \\ v_{\mathrm{S\_}ca} \end{bmatrix} - \begin{bmatrix} R_{\mathrm{CL\_}a} & 0 & 0 \\ 0 & R_{\mathrm{CL\_}b} & 0 \\ 0 & 0 & R_{\mathrm{CL\_}c} \end{bmatrix} \begin{bmatrix} i_{\mathrm{CL\_}ab} \\ i_{\mathrm{CL\_}bc} \\ i_{\mathrm{CL\_}ca} \end{bmatrix} \\ & - \begin{bmatrix} L_{\mathrm{CL\_}a} & 0 & 0 \\ 0 & L_{\mathrm{CL\_}b} & 0 \\ 0 & 0 & L_{\mathrm{CL\_}c} \end{bmatrix} \frac{d}{dt} \begin{bmatrix} i_{\mathrm{CL\_}ab} \\ i_{\mathrm{CL\_}bc} \\ i_{\mathrm{CL\_}ca} \end{bmatrix}, \end{aligned} \tag{2.8}$$

where $i_{\mathrm{CL\_}ab}$, $i_{\mathrm{CL\_}bc}$, and $i_{\mathrm{CL\_}ca}$ are virtual line-to-line currents of critical load, defined as $i_{\mathrm{CL\_}ab} = i_{\mathrm{CL\_}a} - i_{\mathrm{CL\_}b}$, $i_{\mathrm{CL\_}bc} = i_{\mathrm{CL\_}b} - i_{\mathrm{CL\_}c}$, and $i_{\mathrm{CL\_}ca} = i_{\mathrm{CL\_}c} - i_{\mathrm{CL\_}a}$.

Applying the direct-quadrature (dq) reference frame transformation [88, 89] results in d-axis and q-axis components of ED output voltage as follows:

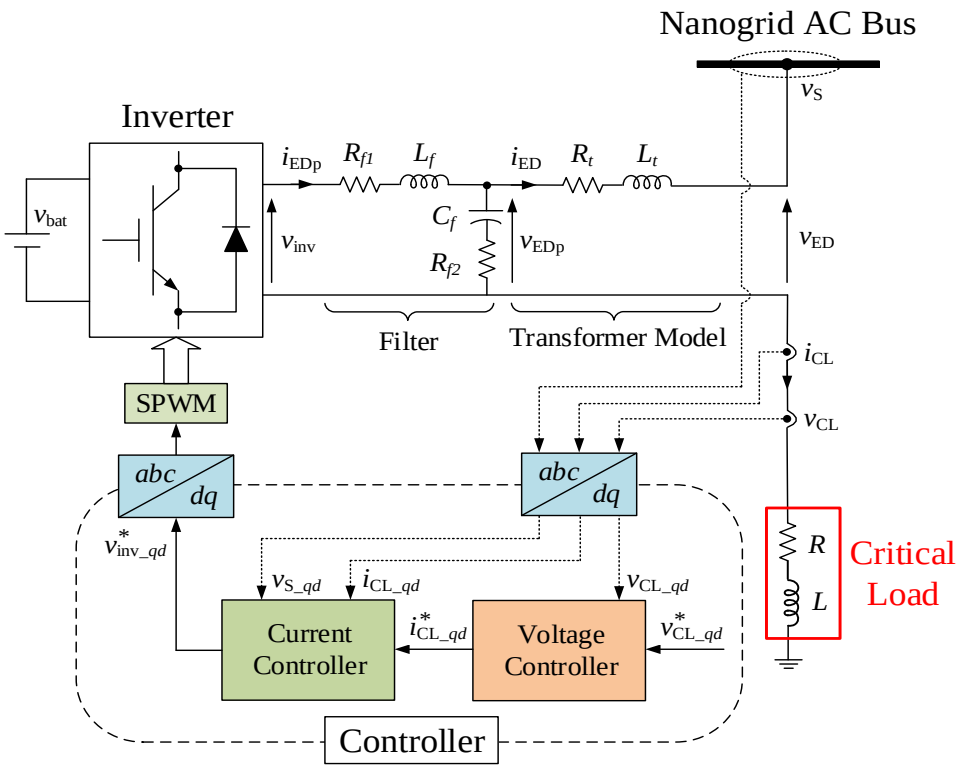

Figure 2.5: Block diagram of a SCL connected to nanogrid ac bus [48, 81].

$$[v_{ED\_qd}] = [v_{S\_qd}] - \begin{bmatrix} R & \omega L \\ -\omega L & R \end{bmatrix} [i_{CL\_qd}] - \begin{bmatrix} L & 0 \\ 0 & L \end{bmatrix} \frac{d}{dt} [i_{CL\_qd}], \tag{2.9}$$

where $\omega = 2\pi f$ is the angular frequency of ac bus. Also, $R = R_{CL\_a} = R_{CL\_b} = R_{CL\_c}$ and $L = L_{CL\_a} = L_{CL\_b} = L_{CL\_c}$ are the resistance and inductance of a symmetrical three-phase critical load, respectively. For the sake of simplicity, d and q components of voltages and currents are expressed as $\kappa_{qd} = \begin{bmatrix} \kappa_q & \kappa_d \end{bmatrix}^T$.

The block diagram of an individual SCL and its controller are illustrated in Figs. 2.5 and 2.6, respectively. In order to regulate the critical load voltage, the reference values for dq components of critical load current, i.e., $i^*_{CL\_qd}$, must be determined. Then, using (2.9), the desired values for the sinusoidal pulse-width modulation (SPWM) of the inverter, i.e., $v^*_{inv\_qd}$, can be obtained. A phase locked loop (PLL) is used to extract the angle of nanogrid ac bus ($\theta = \omega t$). The reference for q-axis component of critical load voltage, i.e., $v^*_{CL\_q}$, is set

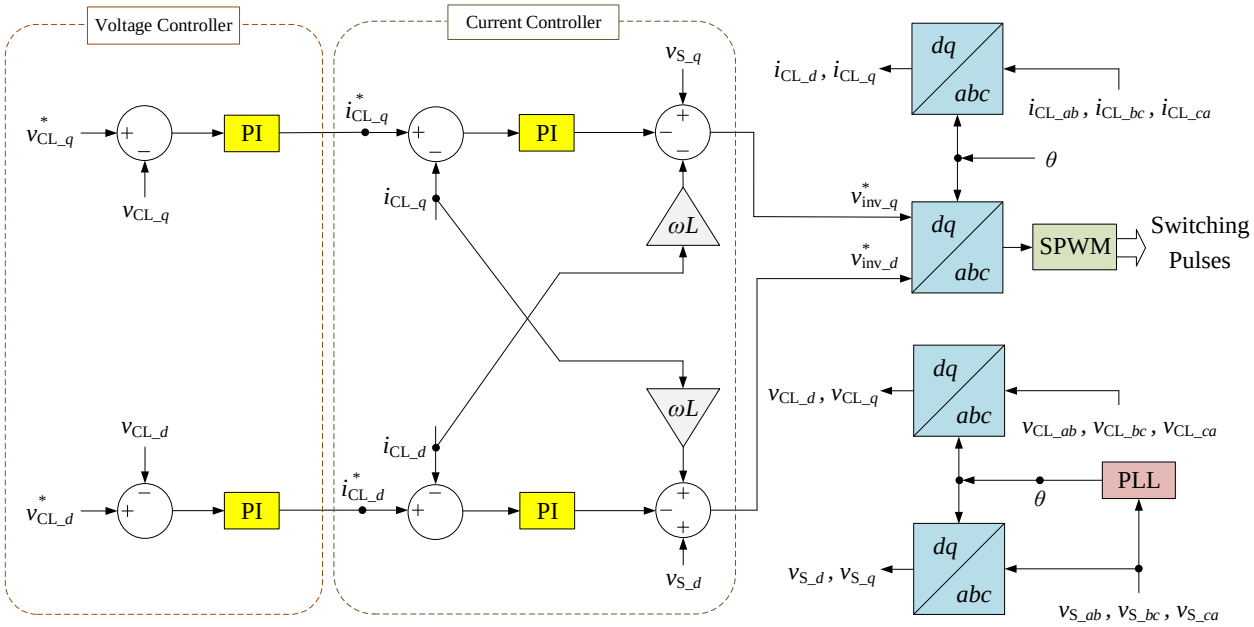

Figure 2.6: Control scheme of SCL [81].

equal to the maximum value of the nominal line-to-line voltage for the critical load, while the d-axis component of critical load voltage, i.e., $v^*_{\mathrm{CL}\_d}$, is set to zero.

The phasor diagrams in Fig. 2.7 illustrate the voltage compensation scenarios. In the case that the ac-bus voltage is less than the reference value of critical load voltage, i.e., $v_{\mathrm{S}} < v^*_{\mathrm{CL}}$, ED maintains the critical load voltage at its nominal level by introducing a compensation voltage, as shown in Fig. 2.7(a). In the case of overvoltage scenario, v_{S} is more than v^*_{CL}, i.e., $v_{\mathrm{S}} > v^*_{\mathrm{CL}}$, and ED compensates the overvoltage to keep the critical load voltage at its nominal value, as shown in Fig. 2.7(b).

2.4 On Stability of Smart Loads

This section presents a small-signal state-space model for SCLs in nanogrids. The presented small-signal modeling approach takes into account the switching process of the three-phase inverter by deriving the state-space equations for the circuits corresponding to each switching state [90, 91].

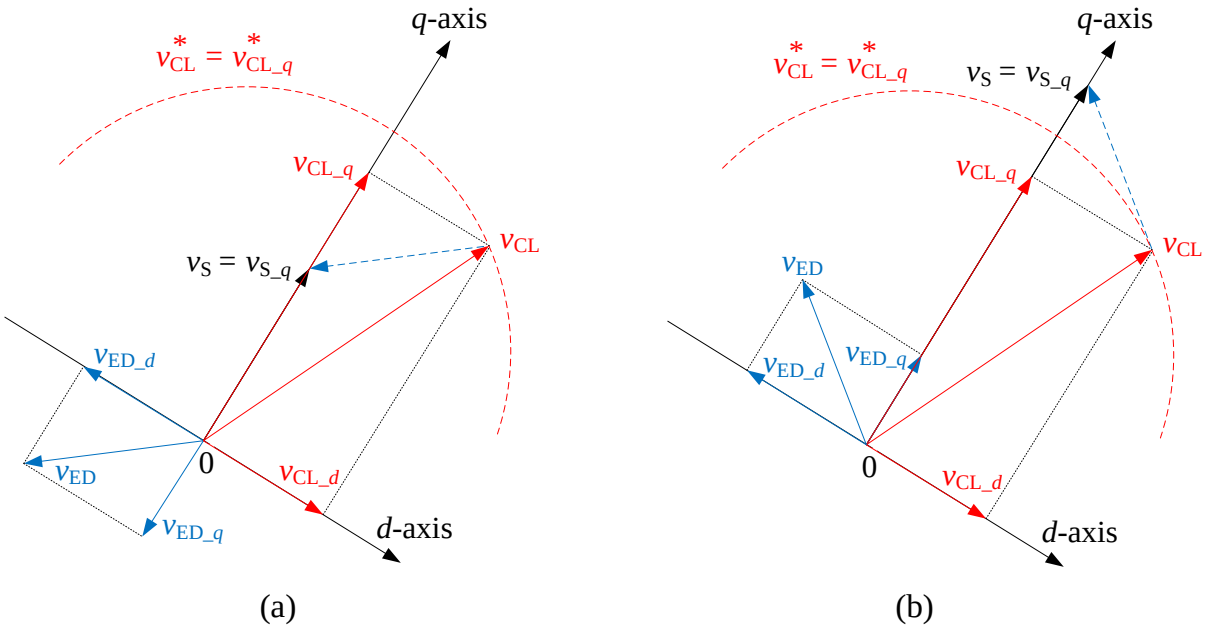

Figure 2.7: Phasor diagrams of SCL with q-axis aligned with ac-bus voltage. (a) Undervoltage compensation. (b) Overvoltage compensation [48, 81].

2.4.1 Small-Signal State-Space Model

As shown in Fig. 2.5, the SCL system includes controllers, inverter, output filter, transformer, and critical load. The proposed modeling approach divides the SCL system into three subsystems: (i) voltage controller, (ii) current controller, and (iii) open-loop circuit. The open-loop circuit includes battery energy storage, three-phase inverter, output filter, isolation transformer, and critical load. The winding resistances and leakage inductances are taken into account in transformer modeling, while magnetizing characteristics of transformer core are neglected. The PWM switching pattern of the inverter is taken into account using an averaged state-space model. In this subsection, the state-space model of each subsystem, i.e., controllers and open-loop circuit, is developed separately. Then, the state-space model of an individual SCL is derived.

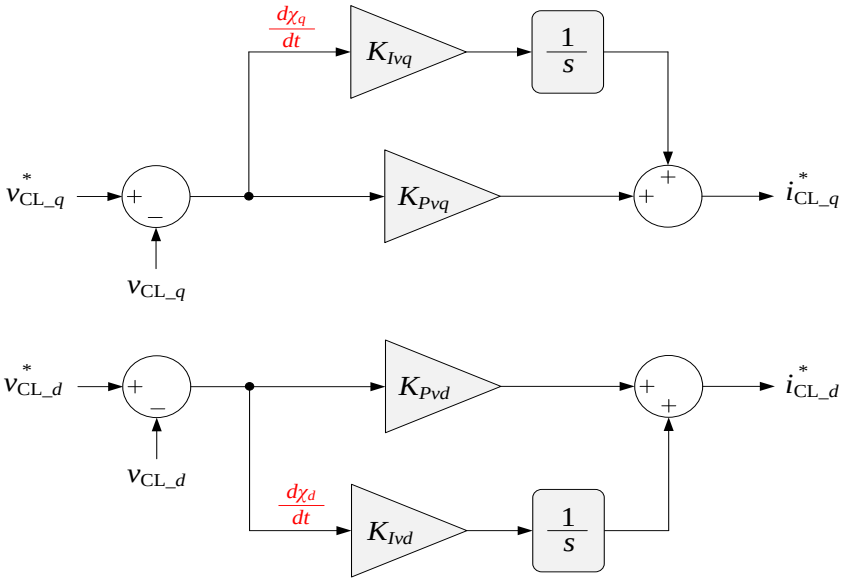

Figure 2.8: Block diagram of voltage controller [48, 92].

2.4.1.1 Voltage Controller

The outer-loop voltage controller is shown in Fig. 2.8. In order to develop the small-signal model of the voltage controller, the state equations are derived as follows:

$$\frac{d\chi_q}{dt} = v^*_{\mathrm{CL\_}q} - v_{\mathrm{CL\_}q} = v^*_{\mathrm{CL\_}q} - \left(Ri_{\mathrm{CL\_}q} + \omega L i_{\mathrm{CL\_}d} + L\frac{d}{dt}i_{\mathrm{CL\_}q}\right), \tag{2.10}$$

$$\frac{d\chi_d}{dt} = v^*_{\mathrm{CL\_}d} - v_{\mathrm{CL\_}d} = v^*_{\mathrm{CL\_}d} - \left(Ri_{\mathrm{CL\_}d} - \omega L i_{\mathrm{CL\_}q} + L\frac{d}{dt}i_{\mathrm{CL\_}d}\right), \tag{2.11}$$

where χ_q and χ_d are the state variables shown in 2.8. The reference values for dq components of critical load current, i.e., $i^*_{\mathrm{CL\_}d}$ and $i^*_{\mathrm{CL\_}q}$, are the output of the voltage controller which can be derived from Fig. 2.8, and taking (2.10) and (2.11) into account as follows:

$$\begin{aligned} i^*_{\mathrm{CL\_}q} &= K_{Pvq}\left(v^*_{\mathrm{CL\_}q} - v_{\mathrm{CL\_}q}\right) + K_{Ivq}\chi_q \\ &= K_{Pvq}\left(v^*_{\mathrm{CL\_}q} - Ri_{\mathrm{CL\_}q} - \omega L i_{\mathrm{CL\_}d} - L\frac{d}{dt}i_{\mathrm{CL\_}q}\right) + K_{Ivq}\chi_q, \end{aligned} \tag{2.12}$$

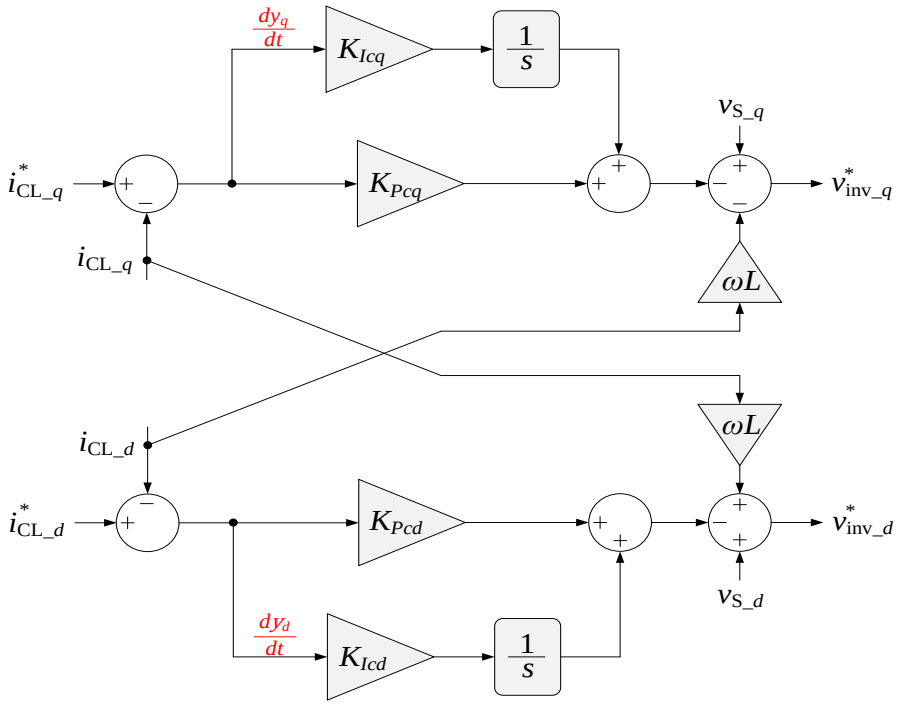

Figure 2.9: Block diagram of current controller [48, 92].

$$\begin{aligned} i^*_{CL\_d} &= K_{Pvd}\left(v^*_{CL\_d} - v_{CL\_d}\right) + K_{Ivd}\chi_d \\ &= K_{Pvd}\left(v^*_{CL\_d} - Ri_{CL\_d} + \omega L i_{CL\_q} - L\tfrac{d}{dt}i_{CL\_d}\right) + K_{Ivd}\chi_d. \end{aligned} \tag{2.13}$$

The derivative terms in (2.10), (2.11), (2.12), and (2.13) are negligible compared with $\omega L i_{CL\_d}$ and $\omega L i_{CL\_q}$. Therefore, the small-signal state-space form of voltage controller can be approximated from (2.10), (2.11), (2.12), and (2.13) as follows:

$$[\Delta\dot{\chi}_{qd}] = A_v\,[\Delta\chi_{qd}] + B1_v\left[\Delta v^*_{CL\_qd}\right] + B2_v\,[\Delta i_{CL\_qd}] + B3_v\,[\Delta\omega]\,, \tag{2.14}$$

$$\left[\Delta i^*_{CL\_qd}\right] = C_v\,[\Delta\chi_{qd}] + D1_v\left[\Delta v^*_{CL\_qd}\right] + D2_v\,[\Delta i_{CL\_qd}] + D3_v\,[\Delta\omega]\,, \tag{2.15}$$

where matrices A_v, $B1_v$, $B2_v$, $B3_v$, C_v, $D1_v$, $D2_v$, and $D3_v$ are provided in Appendix A.

2.4.1.2 Current Controller

The block diagram of the inner-loop current controller is depicted in Fig. 2.9. The corresponding state equations are defined as follows:

$$\frac{dy_q}{dt} = i^*_{\mathrm{CL\_}q} - i_{\mathrm{CL\_}q}, \tag{2.16}$$

$$\frac{dy_d}{dt} = i^*_{\mathrm{CL\_}d} - i_{\mathrm{CL\_}d}, \tag{2.17}$$

where y_q and y_d are the state variables shown in Fig. 2.9. The output equations of the current controller from (2.16), (2.17), and Fig. 2.9 are given by:

$$v^*_{\mathrm{inv\_}q} = v_{\mathrm{S\_}q} - \omega L i_{\mathrm{CL\_}d} - K_{Pcq}\left(i^*_{\mathrm{CL\_}q} - i_{\mathrm{CL\_}q}\right) - K_{Icq} y_q, \tag{2.18}$$

$$v^*_{\mathrm{inv\_}d} = v_{\mathrm{S\_}d} + \omega L i_{\mathrm{CL\_}q} - K_{Pcd}\left(i^*_{\mathrm{CL\_}d} - i_{\mathrm{CL\_}d}\right) - K_{Icd} y_d. \tag{2.19}$$

The small-signal state-space model of the current controller can be determined from linearization and combination of (2.16), (2.17), (2.18), and (2.19) as follows:

$$[\Delta \dot{y}_{qd}] = A_c\left[\Delta y_{qd}\right] + B1_c\left[\Delta i^*_{\mathrm{CL\_}qd}\right] + B2_c\left[\Delta i_{\mathrm{CL\_}qd}\right], \tag{2.20}$$

$$\left[\Delta v^*_{\mathrm{inv\_}qd}\right] = C_c\left[\Delta y_{qd}\right] + D1_c\left[\Delta i^*_{\mathrm{CL\_}qd}\right] + D2_c\left[\Delta i_{\mathrm{CL\_}qd}\right] + D3_c\left[\Delta v_{\mathrm{S\_}qd}\right]. \tag{2.21}$$

From Fig. 2.10, the dq components of inverter output voltage can be expressed as:

$$v_{\mathrm{inv\_}q} = mV_{\mathrm{bat}}\cos\left(\psi\right), \tag{2.22}$$

$$v_{\mathrm{inv\_}d} = -mV_{\mathrm{bat}}\sin\left(\psi\right), \tag{2.23}$$

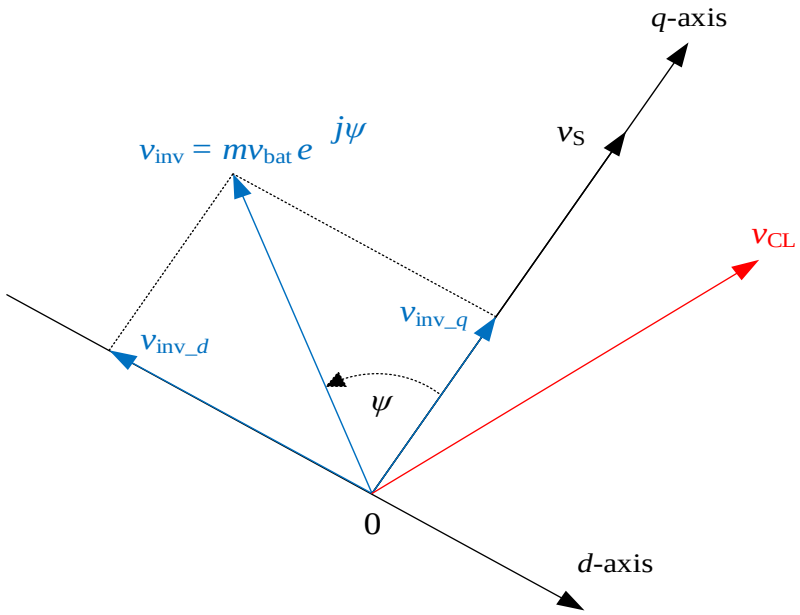

Figure 2.10: Phasor diagram of inverter output voltage and its dq components [48, 92].

where m is the modulation index, V_{bat} is the battery voltage, and ψ is the angle between Phase-A of inverter output voltage and q-axis. Assuming that the inverter output voltage is equal to the desired voltage, i.e., $v_{inv} = v^*_{inv}$, and neglecting the perturbations associated with battery voltage, linearization of (2.22) and (2.23) yields:

$$\left[\Delta v^*_{inv\_qd}\right] = M\left[\Delta u\right], \tag{2.24}$$

where M is provided in Appendix A and $\triangle u = \begin{bmatrix} \triangle m & \triangle \psi \end{bmatrix}^T$. Substituting (2.24) into (2.21) results in:

$$[\Delta u] = M^{-1}(C_c\left[\Delta y_{qd}\right] + D1_c\left[\Delta i^*_{CL\_qd}\right] + D2_c\left[\Delta i_{CL\_qd}\right] + D3_c\left[\Delta v_{S\_qd}\right]), \tag{2.25}$$

where Δu will be used to integrate the state-space model of the current controller with the state-space model of the open-loop circuit.

2.4.1.3 Open-Loop Circuit

The open-loop circuit is divided into two parts: the open-loop ED system and the critical load. The open-loop ED includes a battery, three-phase inverter, LC filter, and an isolation transformer. In the previous work [20], the state-space model of an open-loop inverter with LCL filter is extracted from the switching pattern. Therefore, the modeling approach for open-loop ED is not repeated in this dissertation. Linearizing (2.15) and utilizing the presented model in [20] results in the small-signal state-space model of the open-loop circuit as follows:

$$\begin{bmatrix} \triangle\dot{i}_{\mathrm{EDp\_}qd} \\ \triangle\dot{v}_{\mathrm{EDp\_}qd} \\ \triangle\dot{i}_{\mathrm{ED\_}qd} \\ \triangle\dot{i}_{\mathrm{CL\_}qd} \end{bmatrix} = A_{\mathrm{OL}} \begin{bmatrix} \triangle i_{\mathrm{EDp\_}qd} \\ \triangle v_{\mathrm{EDp\_}qd} \\ \triangle i_{\mathrm{ED\_}qd} \\ \triangle i_{\mathrm{CL\_}qd} \end{bmatrix} + B1_{\mathrm{OL}} \left[\triangle u\right] + B2_{\mathrm{OL}} \begin{bmatrix} \triangle v_{\mathrm{ED\_}qd} \\ \triangle v_{\mathrm{S\_}qd} \end{bmatrix} + B3_{\mathrm{OL}} \left[\triangle\omega\right], \quad (2.26)$$

where A_{OL}, $B1_{\mathrm{OL}}$, $B2_{\mathrm{OL}}$, and $B3_{\mathrm{OL}}$ are given in Appendix A.

2.4.1.4 Complete Model of a Smart Load

Combining the small-signal models of inner-control loop and outer-control loop, as well as the open-loop circuit, defined in (2.14), (2.15), (2.20), (2.21), (2.25), and (2.26), results in the complete model of ith SCL implemented in each nanogrid as follows:

$$\left[\Delta\dot{x}_{\mathrm{SCL}i}\right] = A_{\mathrm{SCL}i} \left[\Delta x_{\mathrm{SCL}i}\right] + B1_{\mathrm{SCL}i} \left[\Delta v^{*}_{\mathrm{CL}i\_qd}\right] + B2_{\mathrm{SCL}i} \begin{bmatrix} \Delta v_{\mathrm{ED}i\_qd} \\ \Delta v_{\mathrm{S\_}qd} \end{bmatrix} + B3_{\mathrm{SCL}i} \left[\Delta\omega\right], \quad (2.27)$$

where the full-form of $A_{\mathrm{SCL}i}$, $B1_{\mathrm{SCL}i}$, $B2_{\mathrm{SCL}i}$, $B3_{\mathrm{SCL}i}$, and $\triangle x_{\mathrm{SCL}i}$ are given in Appendix A. As derived in (2.27), the model of each individual SCL includes twelve state variables and seven inputs. The frequency deviation of ac bus, i.e., $\triangle\omega$, is one of the inputs which is the

same for all SCLs in nanogrid. This is because of taking the reference frame of ac bus as the common reference frame. In other words, the same θ is used for all SCLs in a nanogrid. It is to be noted that there is no need to coordinate the SCLs using a centralized controller, and each SCL is capable of mitigating the voltage and power fluctuations of its critical load autonomously.

2.4.2 Small-Signal Stability Analysis

In this subsection, the dynamic behavior of an individual SCL is analyzed using the developed state-space model. The root locus analysis is used to investigate the location of eigenvalues as a result of changes in different parameters of SCL.

2.4.2.1 System Eigenvalues

Fig. 2.11(a) illustrates the eigenvalues of the complete model of SCL for the parameters given in Table 2.1. It can be observed that there is a high range of frequency variation between the eigenvalues of the system. Four eigenvalues, i.e., λ_7, λ_8, λ_9, and λ_{10}, are near the origin with low frequency, while λ_1, λ_2, λ_3, and λ_4 are high-frequency eigenvalues. The rest of the eigenvalues, i.e., λ_5, λ_6, λ_{11}, and λ_{12}, are farther away from the origin, and their associated frequency is relatively low.

Table 2.1: SCL Parameters

Parameter	**Value**	**Parameter**	**Value**
f	60 Hz	L	2 mH
v_{bat}	570 V	K_{Ivq}	50
v_{S} (line-to-line)	480 V	K_{Pvq}	7
R_{f1}	0.15 Ω	K_{Ivd}	50
L_f	0.5 mH	K_{Pvd}	0.4
R_{f2}	0.008 Ω	K_{Pcq}	0.01
C_f	13.2 µF	K_{Icq}	33.33
R_t	0.03 Ω	K_{Pcd}	1.5
L_t	0.25 mH	K_{Icd}	100
R	2.3 Ω		

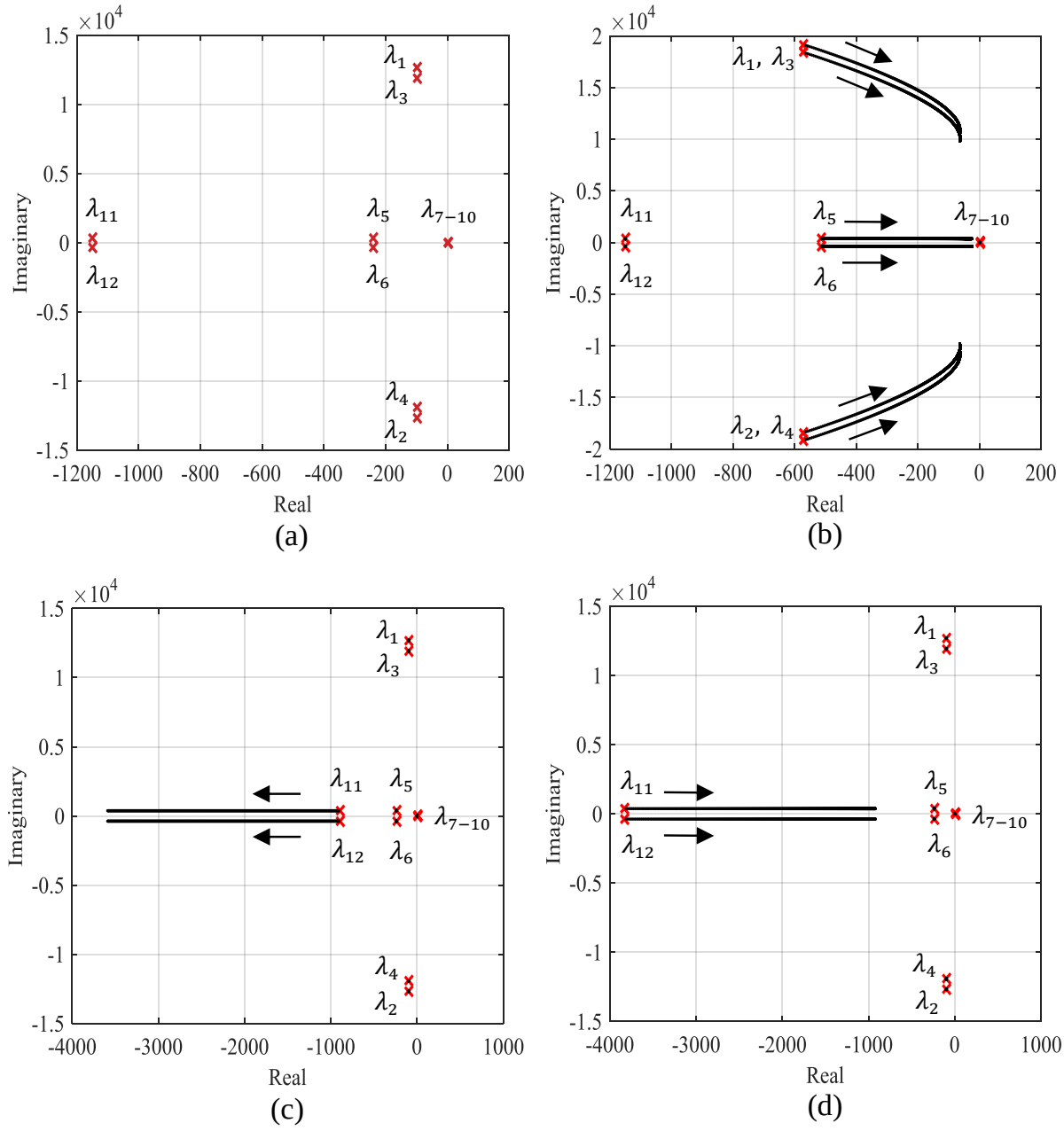

Figure 2.11: Eigenvalue analysis of an individual SCL. (a) SCL eigenvalues for the system parameters given in Table 2.1. (b) Trace of SCL eigenvalues when filter inductance (L_f) is increased from 0.1 mH to 7 mH. (c) Trace of SCL eigenvalues when critical load resistance (R) is increased from 1.8 Ω to 7.18 Ω. (d) Trace of SCL eigenvalues when critical load inductance (L) is increased from 0.6 mH to 2.5 mH [48].

2.4.2.2 Sensitivity to the Filter Inductance

Fig. 2.11(b) depicts the root locus of the SCL eigenvalues when L_f is gradually increased from 0.1 mH to 7 mH, and the other parameters are kept constant, same as Table 2.1. It can be found that increasing L_f drives λ_5, λ_6, and high-frequency eigenvalues, i.e., λ_1, λ_2, λ_3, and λ_4, towards the imaginary axis of complex plane, while the other eigenvalues do not move considerably. This results in deteriorating the damping performance of the system. However, all eigenvalues always stay in the left-hand side of the complex plane even for higher values of L_f.

2.4.2.3 Sensitivity to the Critical Load Resistance

Fig. 2.11(c) shows the root locus of the eigenvalues subsequent to a change in critical load resistance, i.e., R, from 1.8 Ω to 7.18 Ω. As R increases, λ_{11} and λ_{12} move rapidly away from the imaginary axis, resulting in damping improvement of the system. On the other hand, it can be observed that the rest of the eigenvalues are not sensitive to the critical load resistance.

2.4.2.4 Sensitivity to the Critical Load Inductance

The root locus of the SCL eigenvalues is illustrated in Fig. 2.11(d) as the critical load inductance, i.e., L, is varied from 0.6 mH to 2.5 mH. It can be seen that the inductance increase of critical load leads to the departure of a pair of eigenvalues, i.e., λ_{11} and λ_{12}, towards the imaginary axis, while the rest of the eigenvalues are not affected significantly. Notice that even for higher values of L, all eigenvalues remain on the left-hand side of the complex plane. Thus, increasing L results in damping decrease and stability deterioration of the system.

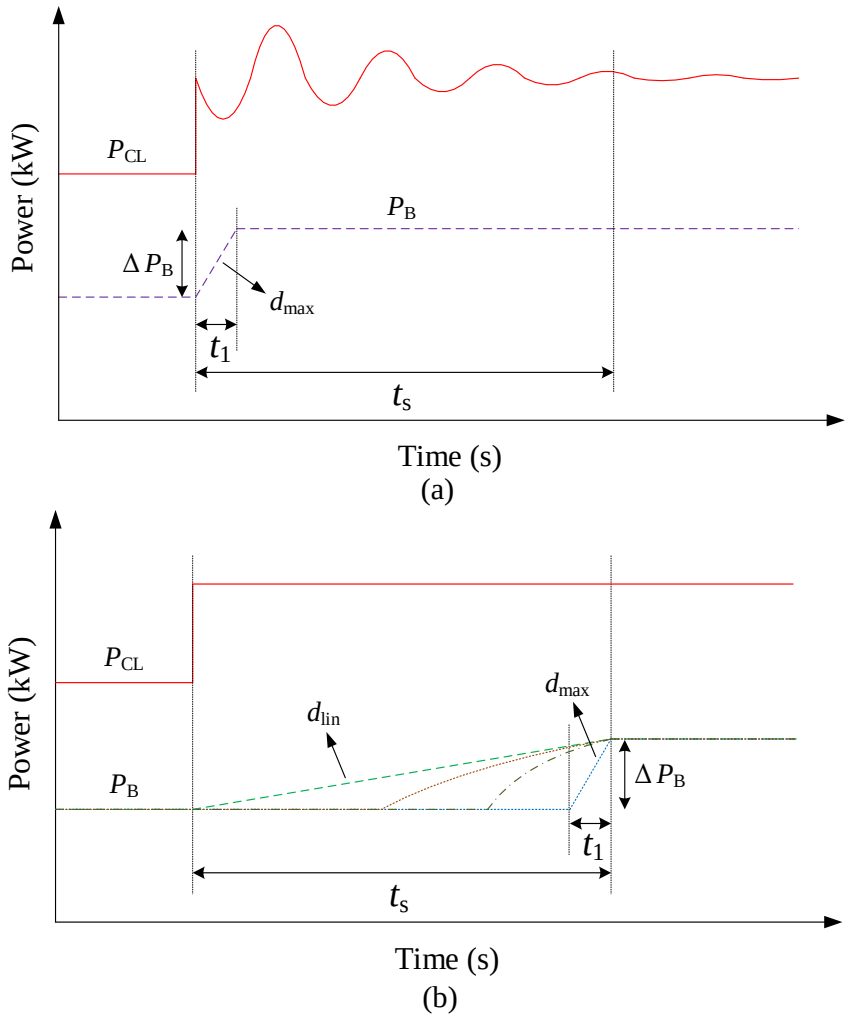

Figure 2.12: Response of central battery bank to critical load step change. (a) Without implementation of SCL. (b) With implementation of SCL [48, 81].

2.5 Size and Lifetime Improvement of Central Battery Bank

As previously mentioned, the generation side of each nanogrid is a combination of different energy resources such as central battery bank, diesel generator, PVs, etc. As reported in [93], repetitive charge/discharge cycles cause a significant reduction in the capacity of batteries. Therefore, it is necessary to protect the central battery bank from high charging/discharging rates caused by sudden load transients. For this purpose, the central battery bank is typically utilized for supplying the load during long-term power demands [94]. This results in lower

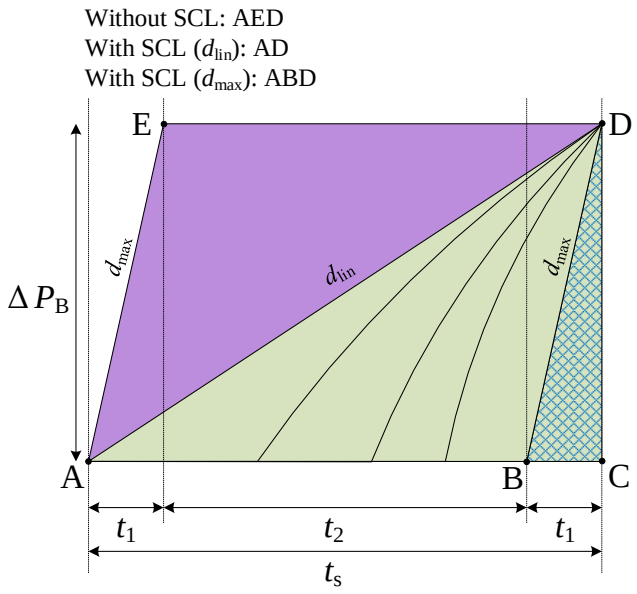

Figure 2.13: Possible power profiles of central battery bank due to critical load step change [48,81].

stress on the battery bank, leading to an extension in its lifetime.

Fig. 2.12(a) illustrates that in the absence of SCL, a step change in critical load leads to short-term power transients. This is due to the low-inertia power generation units of nanogrids. In such condition, the central battery bank, with the power of P_{B}, discharges at its maximum discharge rate, i.e., $d_{\max}$, for a period of t_1 to meet its new power set-point as fast as possible. After that, it supplies the load at zero discharge rate. This results in a severe stress on the battery bank leading to capacity and lifetime deterioration. As shown in Fig. 2.12(b), in the presence of SCL, the central battery bank is capable of providing power under different operating conditions. The battery can be discharged with a linear discharge rate of $d_{\mathrm{lin}} = {}^{\triangle P_{\mathrm{B}}}/_{t_{\mathrm{s}}}$ during the settling time of t_{s}. The battery bank can deliver power at zero discharge rate initially, and then work at its maximum discharge rate of $d_{\max}$. Moreover, battery can be discharged with any non-linear discharge rate between d_{lin} and $d_{\max}$.

Fig. 2.13 shows the power profiles of the central battery bank with and without implementation of SCL with more details. The path AED indicates the power profile with a maximum discharge rate of $d_{\max}$ in the absence of SCL. The power trajectories of AD and ABD, and any non-linear power trajectory lying in between, show the power profiles in the

presence of SCL. The energy delivered by the central battery bank for the power profile following the path ABD can be defined as follows:

$$E_{\text{B\_ABD}} = \text{Area of } \Delta\text{BCD} = \frac{1}{2}t_1\Delta P_{\text{B}} = \frac{1}{2}d_{\max}t_1^2 = \frac{(\Delta P_{\text{B}})^2}{2d_{\max}}. \tag{2.28}$$

The provided energy for the power trajectory of AD can be obtained as follows:

$$E_{\text{B\_AD}} = \text{Area of } \Delta\text{ACD} = \text{Area of } (\Delta\text{ABD} + \Delta\text{BCD}) = \frac{1}{2}t_{\text{s}}\Delta P_{\text{B}} = \frac{1}{2}d_{\text{lin}}t_{\text{s}}^2 = \frac{(\Delta P_{\text{B}})^2}{2d_{\text{lin}}}. \tag{2.29}$$

The energy delivered by the battery bank for the path AED can be defined as follows:

$$\begin{aligned} E_{\text{B\_AED}} &= \text{Area of ABCDEA} = \text{Area of } (\Delta\text{ADE} + \Delta\text{ABD} + \Delta\text{BCD}) \\ &= \frac{1}{2}t_1\Delta P_{\text{B}} + t_2\Delta P_{\text{B}} + t_1\Delta P_{\text{B}}. \end{aligned} \tag{2.30}$$

Considering that $t_2 = t_{\text{s}} - 2t_1$, $E_{\text{B\_AED}}$ in (2.30) can be rewritten as follows:

$$E_{\text{B\_AED}} = (t_{\text{s}} - \frac{1}{2}t_1)\Delta P_B = (\frac{1}{d_{\text{lin}}} - \frac{1}{2d_{\max}})(\Delta P_{\text{B}})^2. \tag{2.31}$$

As can be found from (2.28), (2.29), (2.30), and (2.31), the energy delivered by the central battery bank during the transient is in the following order:

$$E_{\text{B\_ABD}} < E_{\text{B\_AD}} < E_{\text{B\_AED}} \tag{2.32}$$

Therefore, in the absence of SCL (path AED), the central battery bank delivers more energy at a high discharge rate. But, utilization of SCL (path AD, ABD, or any non-linear power trajectory lying in between) results in delivering less amount of energy. It is to be noted that although both the power trajectories of AED and ABD supply the load at a maximum discharge rate of $d_{\max}$, the energy drained from the central battery bank is much less for the path ABD, leading to significant size reduction. Also, following the path AD

Table 2.2: Basic Parameters of Energy Resources Employed on Generation Sides of NG1 and NG2

Parameter	Value
Battery Maximum Charging/Discharging Power	100 kW
Battery Operating Voltage Range	360-600 V
Battery Rated Energy	101 kWh
PV Maximum Power	50 kW
Diesel Generator Maximum Power	127 kW
Diesel Generator Inertia Constant (H)	0.3 s
Microturbine Maximum Power	65 kW

results in the lowest stress level, while the amount of energy delivered by battery bank is in between. Therefore, utilization of SCL results in delivering less energy with a lower discharge rate by choosing any trade-off condition between the power trajectories of AD and ABD.

2.6 Verification

Several case studies are demonstrated in this section to verify the performance of the developed SCLs in improving the dynamic behavior of nanogrids and consequently GNG. As the first step, the detailed models of Nanogrid 1 (NG1) and Nanogrid 2 (NG2) shown in Fig. 2.2 are developed in PSCAD/EMTDC environment. All implemented SCLs have the same parameters as those listed in Table 2.1. The nominal line-to-line ac-bus voltage for each nanogrid is considered 480 V. The generation side of NG1 consists of a PV unit, a diesel generator, and a central battery bank, with the parameters provided in Table 2.2. The generation side of NG2 is similar to NG1 except that the diesel generator is replaced by a 65 kW microturbine system.

2.6.1 Case Study 1: Critical Load Step Change

The first case study investigates the dynamic performance of NG1 while there is a step change in critical load with and without implementation of SCL. The NG1, shown in Fig. 2.14, operates in islanded mode, and therefore, diesel generator participates in primary

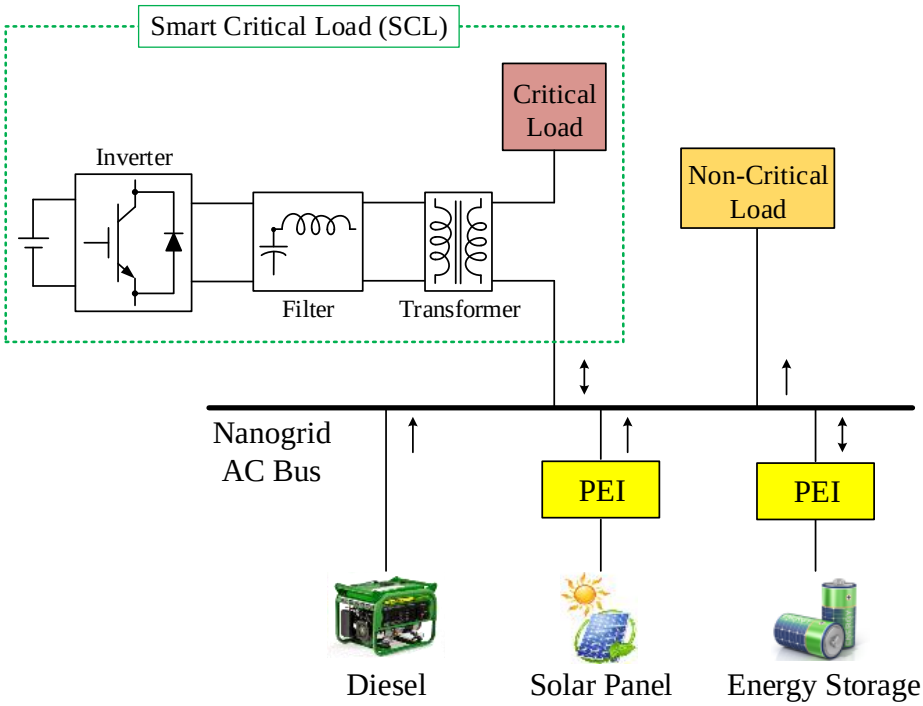

Figure 2.14: Case study 1: NG1 operating in islanded mode.

voltage and frequency control of ac bus using an AVR and governor. The active and reactive power of critical load, i.e., P_{CL} and Q_{CL}, are initially 60 kW and 20 kVAr. The active and reactive power of non-critical load, i.e., P_{NCL} and Q_{NCL}, remain constant at 30 kW and 10 kVAr during this case study. At instant t = 30 s, the active and reactive power of critical load are stepped up to 90 kW and 30 kVAr.

The PV unit and battery bank operate in PQ control mode while diesel generator is regulating voltage and frequency. As shown in Fig. 2.15 (left), without implementation of SCL, the system requires almost 3 s to meet the new critical load demand due to the inertia of diesel generator. However, the proposed SCL helps the system to provide the exact amount of demand requested by the critical load in less than 0.2 s, see Fig. 2.15 (right). After increasing the critical load demand, the active and reactive power of ED, i.e., P_{ED} and Q_{ED}, are negative for about 1 s, which means that the ED is injecting the deficit power into the system (discharge mode). Morover, it can be obsereved that with the proposed SCL configuration, the critical load voltage, i.e., v_{CL}, is well regulated at its rated value, i.e., 480 V, and the fluctuations are significantly mitigated. Table 2.3 summarizes the comparison

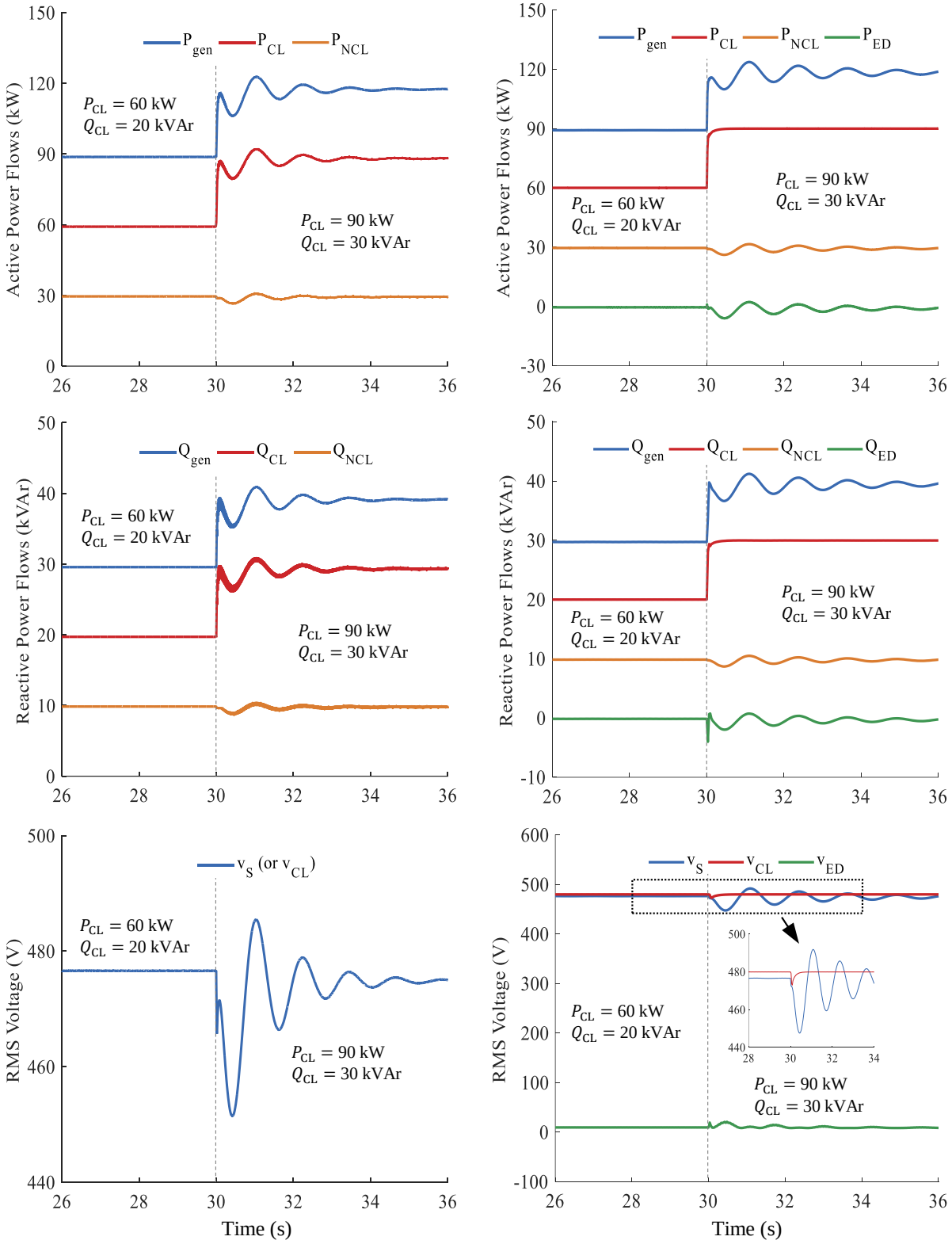

Figure 2.15: Case study 1: step change in critical load demand of NG1 (islanded) without (left) and with (right) implementation of SCL.

Table 2.3: Dynamic Performance Comparison of NG1 for Step Change in Critical Load Demand with and without SCL (Case study 1)

	Without SCL		**With SCL**	
	Settling Time	Overshoot	Settling Time	Overshoot
P_{CL}	$\approx$ 3 s	$\approx$ 4 kW	$<$ 200 ms	negligible
Q_{CL}	$\approx$ 3 s	$\approx$ 1 kVAr	$<$ 200 ms	negligible
v_{CL}	$\approx$ 4 s	$\approx$ 10 V	$<$ 400 ms	negligible

between the operational performance of NG1 with and without implementation of SCL based on the results demonstrated in Fig. 2.15. From Table 2.3, utilizing the proposed SCL results in remarkable improvement in the dynamic behavior of NG1 for a step change in critical load demand.

According to the stability analysis in Figs. 2.11(c) and 2.11(d), λ_{11} and λ_{12} are two eigenvalues with the highest sensitivity to the critical load level. Moreover, it can be observed that the frequency associated with the aforementioned eigenvalues is around 60 Hz. Fig. 2.16 shows that a step change in critical load leads to transients in dq components of critical load current, i.e., $i_{\text{CL\_}d}$ and $i_{\text{CL\_}q}$, with a frequency around 60 Hz which is in good agreement with the stability analysis presented in Section 2.4.

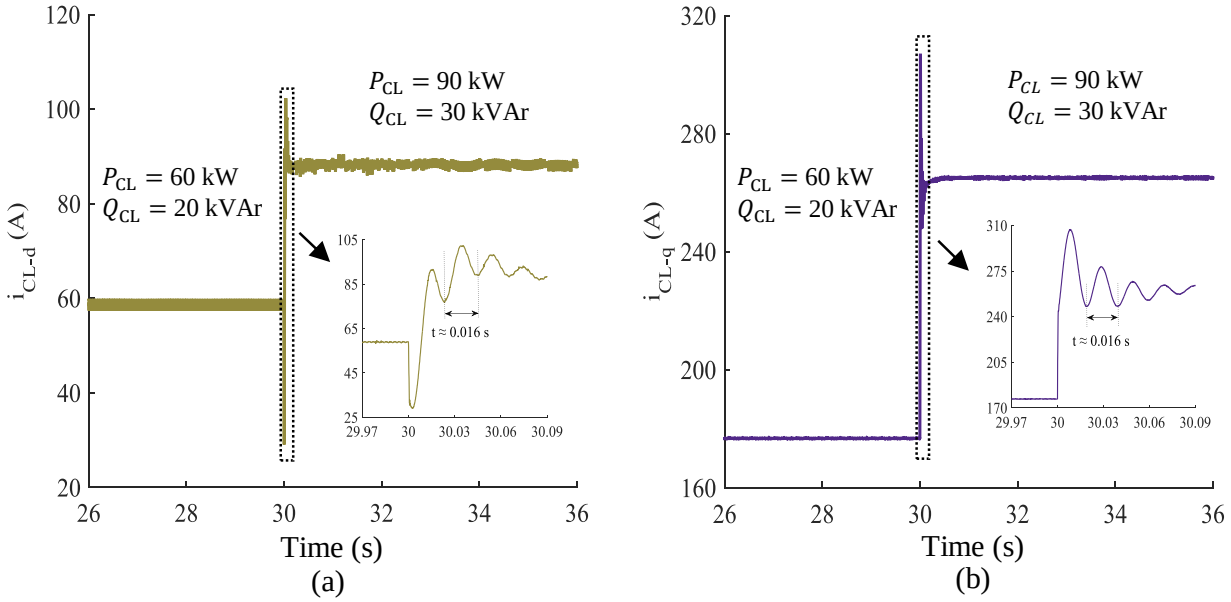

Figure 2.16: Case study 1: response of critical load current to step change in critical load demand of NG1 (islanded) with implementation of SCL. (a) d-axis component. (b) q-axis component.

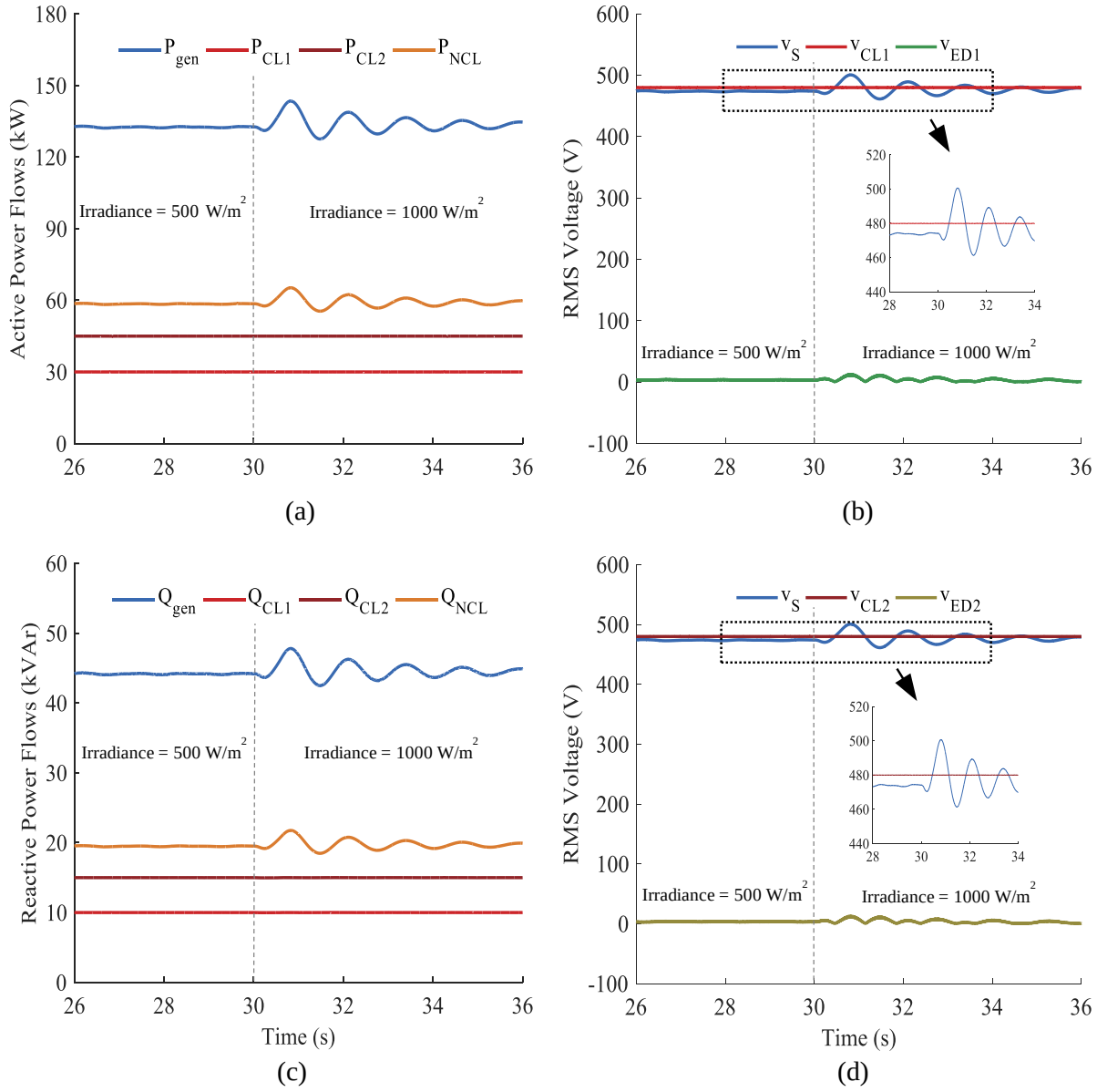

Figure 2.17: Case study 2: effect of change in solar irradiance on performance of NG1 (islanded) with implementation of SCL.

2.6.2 Case Study 2: Solar Irradiance Variation

This case study investigates the effect of solar irradiance variation on the operational performance of NG1. In this scenario, the system is islanded from the rest of GNG and two SCLs are connected to the ac bus of NG1. The active and reactive power of critical load 1 and 2 are $P_{\text{CL1}} = 30$ kW, $Q_{\text{CL1}} = 10$ kVAr, $P_{\text{CL2}} = 45$ kW, and $Q_{\text{CL2}} = 15$ kVAr. The required

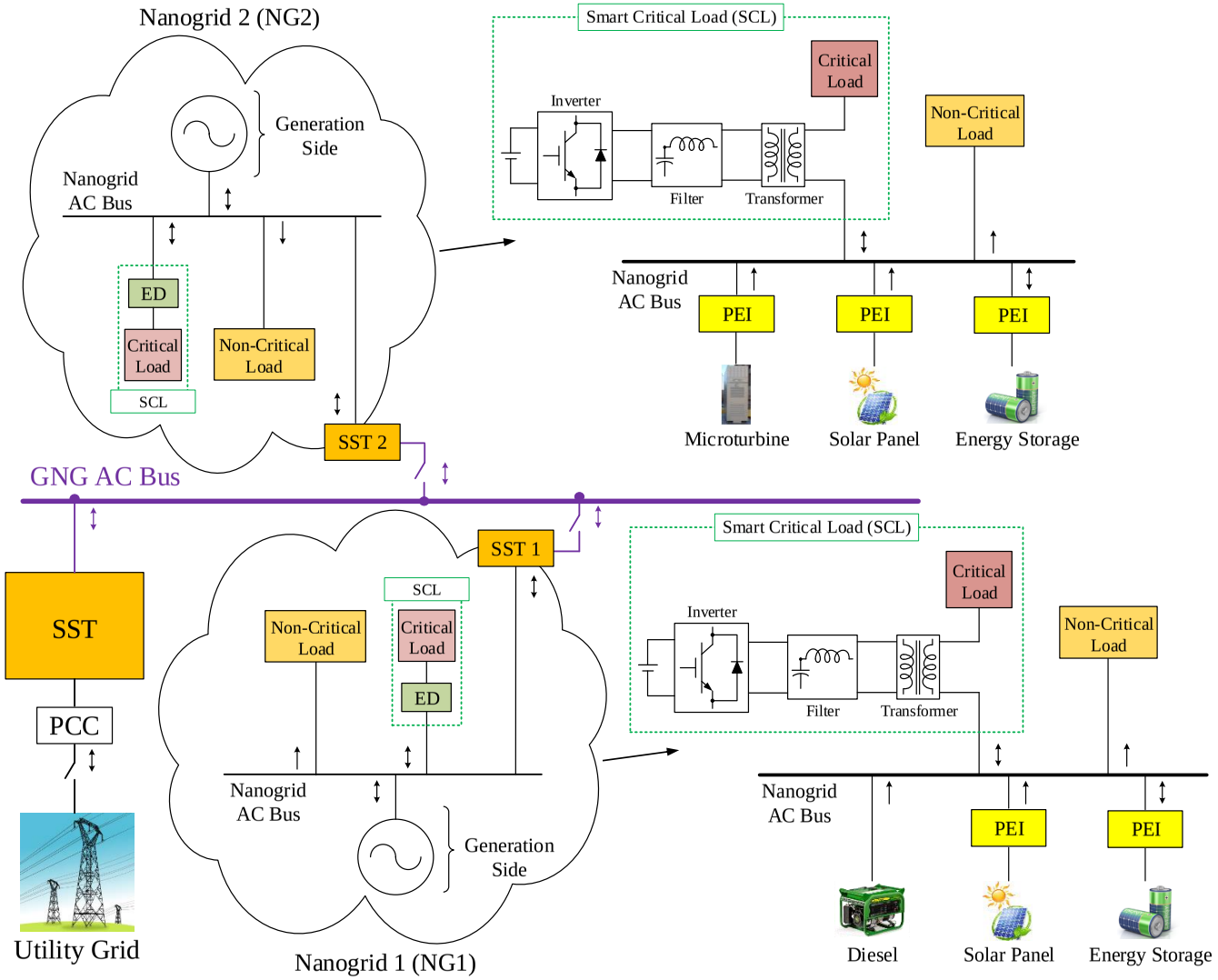

Figure 2.18: Case study 3: NG1 transferring from GNG-connected to islanded mode.

active and reactive power of non-critical load, i.e., P_{NCL} and Q_{NCL}, are 60 kW and 20 kVAr. At $t = 30$ s, the solar irradiance level starts to increase from 500 W/m^2 to 1000 W/m^2, with an exaggerated ramp rate of 1000 W/m^2/s, which results in power imbalance between generation side and demand side. As shown in Figs. 2.17(a) and 2.17(c), the proposed SCLs compensate the fluctuations of P_{gen} and Q_{gen} for critical loads in islanded NG1. Figs. 2.17(b) and 2.17(d) compare the ac-bus voltage, i.e., v_{S}, with critical load voltages, i.e., v_{CL1} and v_{CL2}, and it can be seen that although the ac-bus voltage is fluctuating, v_{CL1} and v_{CL2} are well regulated at 480 V.

2.6.3 Case Study 3: GNG-Connected to Islanded Mode

Due to the low inertia of nanogrids, disconnecting them from GNG can cause larger transients in voltage and current compared with traditional microgrids. Thus, this case study evaluates the effectiveness of the proposed SCL configuration in mitigating voltage and power fluctuations of critical loads during the transition from GNG-connected to islanded mode of operation. The GNG considered in this case study is shown in Fig. 2.18 consisting of two nanogrids, i.e., NG1 and NG2, and each nanogrid includes only one SCL and one non-critical load ($P_{\mathrm{CL}} = 60$ kW, $Q_{\mathrm{CL}} = 20$ kVAr, $P_{\mathrm{NCL}} = 30$ kW, and $Q_{\mathrm{NCL}} = 10$ kVAr). NG1 is initially in GNG-connected mode of operation and at $t = 30$ s, the grid operator disconnects it from GNG.

Fig. 2.19 demonstrates the effectiveness of the proposed SCL on the operational performance of NG1 during the transition from GNG-connected to islanded mode. During GNG-connected mode, there is extra power generation in the system, i.e., $P_{\mathrm{gen}} > P_{\mathrm{L}}$, which is absorbed by GNG, i.e., $P_{\mathrm{GNG}} < 0$. At $t = 30$ s, NG1 is triggered to operate in islanded mode, and as shown in Fig. 2.19 (left), without the proposed SCL, the active power supplied to the critical load, i.e., P_{CL}, starts fluctuating during the transition. However, from Fig. 2.19 (right), it can be observed that the proposed SCL compensates these fluctuations caused by islanding of NG1. Besides, when NG1 is GNG connected, the required reactive power is provided by GNG, i.e., $Q_{\mathrm{GNG}} > 0$. Similarly, the proposed SCL suppresses the reactive

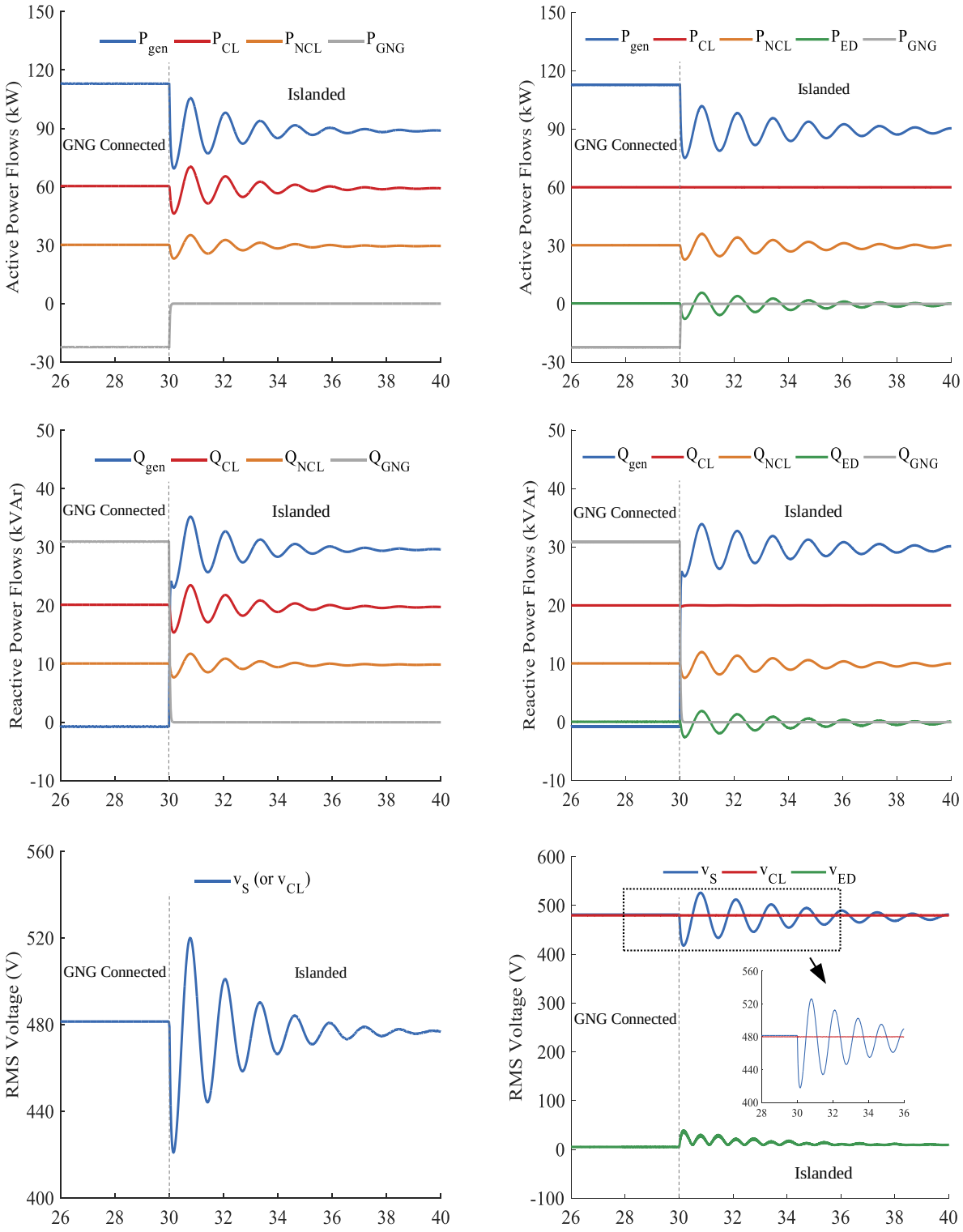

Figure 2.19: Case study 3: transition of NG1 from GNG-connected to islanded mode without (left) and with (right) implementation of SCL.

Table 2.4: Dynamic Performance Comparison of NG1 during Transition from GNG-Connected to Islanded Mode with and without SCL (Case Study 3)

	Without SCL		**With SCL**	
	Settling Time	Overshoot	Settling Time	Overshoot
P_{CL}	$\approx$ 6 s	$\approx$ 10 kW	negligible	negligible
Q_{CL}	$\approx$ 6 s	$\approx$ 3 kVAr	$<$ 100 ms	negligible
v_{CL}	$\approx$ 8 s	$\approx$ 40 V	negligible	negligible

power fluctuations during the transition from GNG-connected mode to islanded mode. In addition, the fluctuations of v_{CL} are analyzed in Fig. 2.19, with and without the proposed SCL configuration. It can be observed that in the absence of SCL, disconnecting NG1 from GNG leads to relatively large oscillations in v_{S}, and consequently v_{CL}. The proposed SCL configuration regulates v_{CL} at 480 V (nominal value), and significantly mitigates its fluctuations during the transition. Table 2.4 investigates the effect of utilizing the proposed SCL in operational performance improvement of NG1 based on the results demonstrated in Fig. 2.19. The provided comparison analysis in Table 2.4 indicates that the proposed SCL configuration is an effective solution for dealing with the stability challenges and improving the power quality in nanogrids during transition from GNG-connected to islanded mode of operation.

2.7 Conclusion

A study on effects of employing smart loads in a fleet of nanogrids has been presented in this chapter to investigate their role in further mitigation of voltage and power fluctuations across critical loads during abnormal grid conditions, sudden load changes, and fluctuations in power generation. The operational performance of nanogrids with and without the proposed smart loads have been compared; the results demonstrate significant improvement in power quality of nanogrids when incorporating the proposed smart loads. A detailed small-signal state-space model has been derived for the proposed smart loads considering the switching process of three-phase inverter. This model has been used to investigate the location of eigenvalues due to the changes in different parameters of smart load to demon-

strate the stability region and robustness of the proposed smart load configuration. This developed model could be incorporated into the models of nanogrids in order to study the effect of utilizing smart loads on the stability of overall system. Moreover, it has been demonstrated that the suggested smart load configuration can be an effective solution to improve the lifetime and reduce the size of the central battery bank. Several case studies have been carried out to validate the effectiveness of the proposed smart loads in small-scale microgrid known as nanogrid featuring low inertia.

Chapter 3

Improved Dynamics in Islanded Mixed-Inertia Microgrids

This chapter proposes improved droop control approaches to enhance the dynamic response of islanded microgrids by mitigating voltage and frequency fluctuations. Islanded microgrids are vulnerable to voltage and frequency variations due to the presence of low-inertia DG units. Moreover, implementation of both synchronous-based and inverter-based DG units with a significant difference in inertia forms islanded mixed-inertia microgrids, leading to instantaneous power imbalance between generation and consumption during abnormal conditions. This results in voltage and frequency deviations which might have severe consequences such as blackouts. This chapter presents piecewise linear-elliptic (PLE) droops to be employed in BESS with fast response in order to balance the active and reactive power during abnormal conditions. It is demonstrated that for any linear droop characteristic with a specified droop coefficient, there is also a PLE droop characteristic which can be formulated using the proposed approach in this chapter. Compared with linear droops, an enhanced dynamic response is achieved by utilizing the proposed PLE droops. Furthermore, an adaptive piecewise droop (APD) is proposed and employed in PV units to achieve a faster balance between generation and consumption during abnormalities, leading to an enhanced frequency response. Besides, the reactive-power control loop of PV units is equipped with

a droop characteristic which enables the PV systems to inject/absorb reactive power during abnormalities and participate in voltage-profile enhancement of microgrids. In this way, the conventional inverters implemented in BESSs and PV units turn into smart inverters [74–78] to cope with fast transients. Several case studies are carried out in PSCAD/EMTDC to verify the validity of proposed droop control methods in improving the dynamics of islanded mixed-inertia microgrids.

The contents of this chapter are organized into four sections. Section 3.1 studies the cooperative role of BESS in improving the dynamics of islanded microgrids by proposing two PLE droops. Moreover, the conventional control scheme of PV units is modified in Section 3.2 to suppress the short-term voltage and frequency fluctuations in islanded microgrids. The proposed methods are verified by carrying out different case studies in Section 3.3. Finally, the concluding remarks for this chapter are given in Section 3.4.

3.1 Energy-Storage Fed Smart Inverters for Enhanced Voltage and Frequency Regualtion in Islanded Mixed-Inertia Microgrids

In this section, the traditional controller of BESS is deployed to enhance the dynamic response of islanded microgrids by mitigating the voltage and frequency fluctuations. The schematic of islanded mixed-inertia microgrid under study is shown in Fig. 3.1. Since the cooperative role of BESS in improving the dynamic behavior of the system is investigated in this section, the control scheme of BESS is illustrated with more details. A diesel generator is responsible for the primary voltage and frequency control of the main ac bus using an AVR and governor, i.e., grid-forming mode. The PV unit is connected to the ac bus through a boost dc-dc converter and a dc-ac inverter while operating in PQ-control mode (or grid-following mode) to inject the desired active and reactive power to the system. However, significant inertia difference between diesel generator and PV unit can easily lead to a

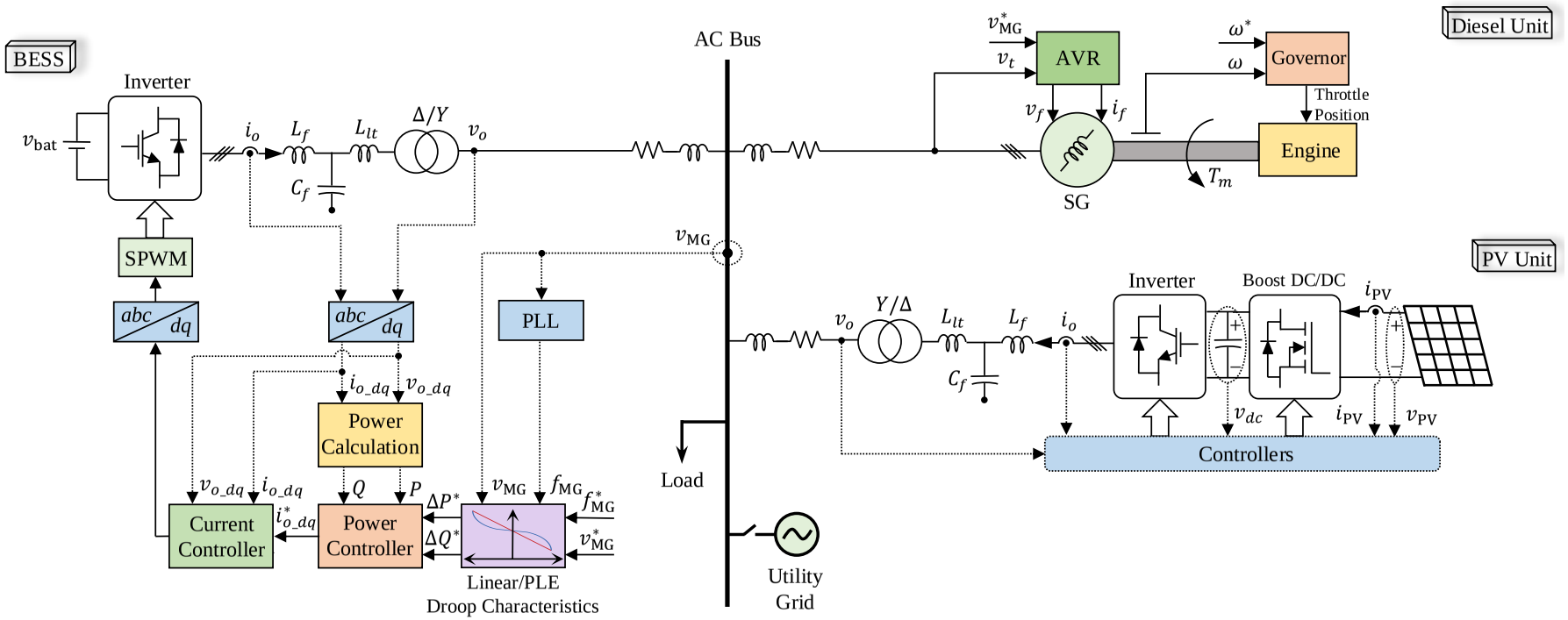

Figure 3.1: Configuration of islanded mixed-inertia microgrid with modified control scheme of BESS [95].

power imbalance between generation and consumption. This results in voltage and frequency variations which might have severe consequences such as blackouts.

In order to resolve the short-term voltage and frequency deviation issues, the BESS is utilized to balance the power supply and demand by injecting/absorbing the active and reactive power. For this purpose, two different PLE droops, i.e., *P-f* and *Q-v*, are defined for BESS to participate in voltage and frequency regulation in case of abnormal conditions. During the steady-state condition, the voltage and frequency of microgrid ac bus, i.e., v_{MG} and f_{MG}, are regulated at their nominal values, i.e., v^*_{MG} and f^*_{MG}, and thus, based on the implemented droop characteristics, the BESS does not cooperate in voltage and frequency regulation. However, since v_{MG} and f_{MG} are not fixed at their nominal values during abnormalities, the BESS participates in voltage and frequency restoration. In such condition, the BESS injects/absorbs the active and reactive power according to the proposed method, leading to an enhanced dynamic response compared with linear droops.

3.1.1 Frequency Dynamic-Response Improvement

This subsection investigates solutions to achieve an enhanced frequency response for islanded microgrids during abnormal conditions. First, a brief overview of the frequency dynamic-response of the system along with implemented *P-f* droops, i.e., linear and PLE, is presented, and then further explanation of the proposed PLE droop is provided.

3.1.1.1 Frequency Dynamic-Response of the System

The frequency deviations of ac bus during the settling time of t_{s} are shown in Fig. 3.2(a). These frequency variations can be a result of severe conditions such as load step change, solar irradiance variation, and transition from grid-connected to islanded mode. At point A, the system operates at its nominal frequency, i.e., f^*_{MG}. However, during abnormal conditions, the frequency of ac bus deviates which might lead to blackouts. For instance, at point B, the ac-bus frequency is lower than its nominal value, whereas the system suffers from high frequency at point C. Thus, as illustrated in Fig. 3.2(b), in order to mitigate these short-

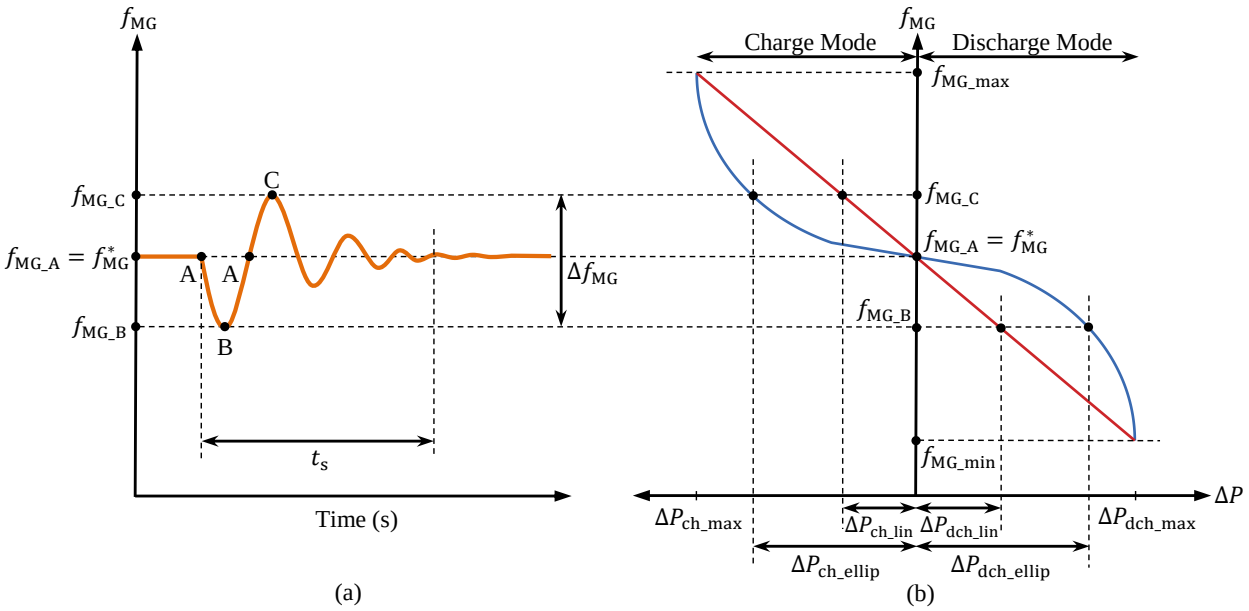

Figure 3.2: (a) Frequency variations of ac bus caused by abnormal conditions, and (b) corresponding linear (red line) and PLE (blue line) *P-f* droops [96].

term fluctuations, linear and PLE *P-f* droops can be implemented in BESS to cover the active power mismatches between generation and consumption. In Fig 3.2(b), the trajectory of linear *P-f* droop is shown by the red line, while the blue line is the trajectory of proposed PLE droop. Both linear and PLE droops are implemented within the same predefined frequency and active power range, which means that they both have the same start point and end point. A comparison between linear and PLE trajectories leads to the fact that more active power can be injected/absorbed during abnormalities, for faster adjustment of the frequency deviation, by employing the PLE droop. This results in an enhanced frequency dynamic response and stability improvement of the system.

Depending on the frequency of ac bus, three modes of operation can be defined for BESS: discharge mode, charge mode, and idle mode. In case of under frequency, i.e., $f_{\mathrm{MG}} < f^*_{\mathrm{MG}}$, the BESS operates in discharge mode, i.e., $\triangle P > 0$, to inject the deficit active power caused by significant inertia difference between DG units. On the other hand, when the frequency is higher than its nominal value, i.e., $f_{\mathrm{MG}} > f^*_{\mathrm{MG}}$, the BESS operates in charge mode, i.e., $\triangle P < 0$, and absorbs the extra active power in the system to restore the frequency. During the steady-state condition, the system operates at its nominal frequency, i.e., $f_{\mathrm{MG}} = f^*_{\mathrm{MG}}$,

and hence, the BESS is in idle mode, i.e., $\triangle P = 0$.

As can be found from Fig. 3.2(b), for the linear *P-f* droop with coefficient of m_P, the injected/absorbed active power by BESS can be obtained as follows:

$$\triangle P_{\text{lin}} = \frac{f^*_{\text{MG}} - f_{\text{MG}}}{m_P} = \begin{cases} \triangle P_{\text{dch\_lin}} > 0 & \text{if } f_{\text{MG}} < f^*_{\text{MG}} \text{ (discharge mode)} \\ 0 & \text{if } f_{\text{MG}} = f^*_{\text{MG}} \text{ (idle mode)} \\ \triangle P_{\text{ch\_lin}} < 0 & \text{if } f_{\text{MG}} > f^*_{\text{MG}} \text{ (charge mode)} \end{cases} \tag{3.1}$$

where f_{MG} and f^*_{MG} are the frequency of ac bus and its nominal value, respectively. $\triangle P_{\text{dch\_lin}}$ is the active power injected by BESS during discharge mode, and $\triangle P_{\text{ch\_lin}}$ is the active power absorbed by BESS during charge mode.

3.1.1.2 Piecewise Linear-Elliptic (PLE) *P-f* Droop

As previously mentioned, the upper and lower limits of frequency, i.e., $f_{\text{MG\_max}}$ and $f_{\text{MG\_min}}$, and the active power range of BESS are predetermined. Thus, a potential solution to enhance the frequency dynamic-response of the system is to define a new trajectory instead of a linear trajectory. As shown in Fig. 3.3, for the discharge mode, the start point, i.e., f^*_{MG}, and end point, i.e., $f_{\text{MG\_min}}$, can be connected by a quarter ellipse centered at $f_{\text{MG\_min}}$, whose horizontal radius is $\triangle P_{\text{dch\_max}}$ and vertical radius is $f^*_{\text{MG}} - f_{\text{MG\_min}}$. Herein, $\triangle P_{\text{dch\_max}}$ is the maximum active power that can be injected by BESS, which can be obtained from (3.1) as follows:

$$\triangle P_{\text{dch\_max}} = \frac{f^*_{\text{MG}} - f_{\text{MG\_min}}}{m_P} > 0. \tag{3.2}$$

Therefore, considering the abovementioned quarter ellipse, the active power provided by BESS during the discharge mode can be obtained as follows:

$$\triangle P_{\text{dch\_ellip}} = \sqrt{\frac{(f^*_{\text{MG}} - f_{\text{MG\_min}})^2 - (f_{\text{MG}} - f_{\text{MG\_min}})^2}{m_P^2}} > 0. \tag{3.3}$$

Similarly, as illustrated in Fig. 3.3, the trajectory between f^*_{MG} and $f_{\text{MG\_max}}$ during the

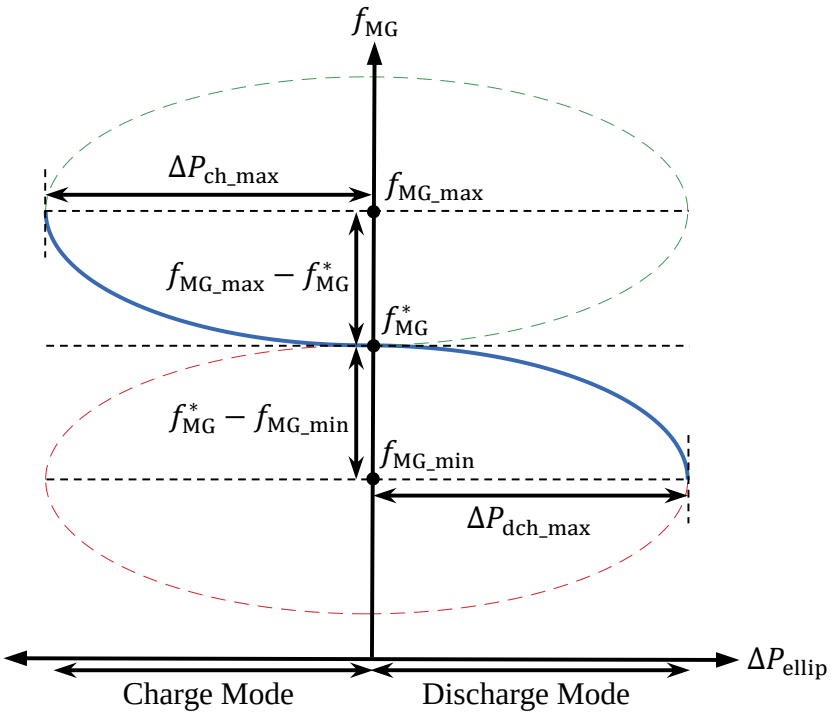

Figure 3.3: The elliptic trajectory (blue line) defined for charge and discharge modes of BESS [96].

charging can be considered as a quarter ellipse centered at $f_{\text{MG\_max}}$, with the horizontal radius of $\triangle P_{\text{ch\_max}}$ and vertical radius of $f_{\text{MG\_max}} - f^*_{\text{MG}}$. Considering the specified value of droop coefficient, i.e., m_P, $\triangle P_{\text{ch\_max}}$ is the maximum active power that can be absorbed by BESS, and can be obtained from (3.1) as follows:

$$\triangle P_{\text{ch\_max}} = \frac{f^*_{\text{MG}} - f_{\text{MG\_max}}}{m_P} < 0. \tag{3.4}$$

As the result, the active power absorbed by BESS during the charge mode can be formulated as follows:

$$\triangle P_{\text{ch\_ellip}} = -\sqrt{\frac{(f^*_{\text{MG}} - f_{\text{MG\_max}})^2 - (f_{\text{MG}} - f_{\text{MG\_max}})^2}{m_P^2}} < 0. \tag{3.5}$$

Considering the fact that the slope of elliptic trajectory shown in Fig. 3.3, i.e., the blue line, is zero at the nominal frequency, a narrow linear region should be defined around the nominal frequency as follows:

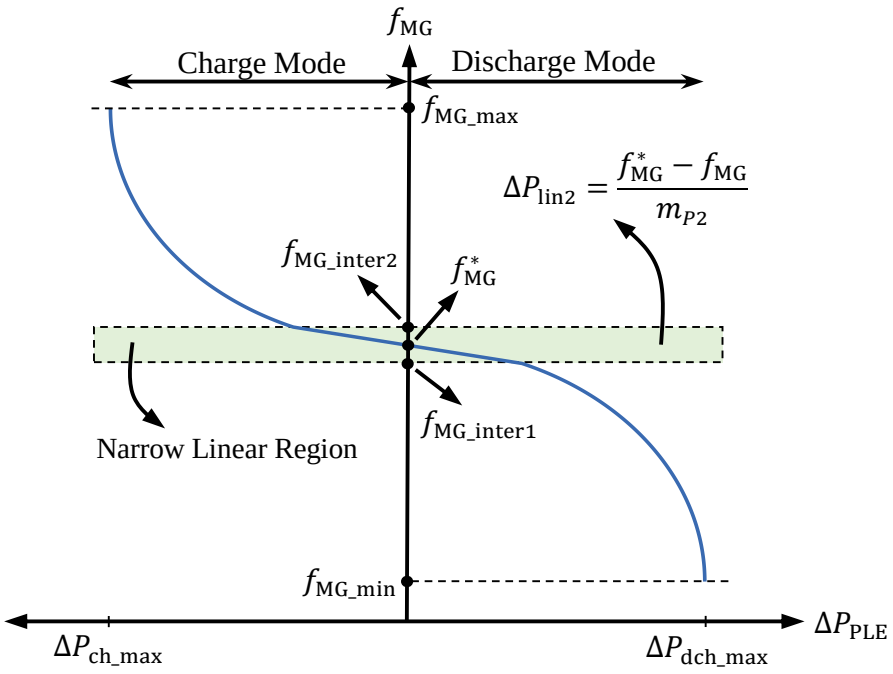

Figure 3.4: The PLE *P-f* droop for frequency dynamic-response improvement [96].

$$\triangle P_{\text{lin2}} = \frac{f^*_{\text{MG}} - f_{\text{MG}}}{m_{P2}}, \tag{3.6}$$

where m_{P2} is the droop coefficient of narrow linear trajectory which should always be less than m_P.

The proposed PLE droop for achieving an enhanced frequency response during abnormalities is shown in Fig. 3.4. As can be found from (3.3), (3.5), and (3.6), the injected/absorbed active power by BESS for the PLE *P-f* droop can be expressed as follows:

$$\triangle P_{\text{PLE}} = \begin{cases} \sqrt{\dfrac{(f^*_{\text{MG}} - f_{\text{MG\_min}})^2 - (f_{\text{MG}} - f_{\text{MG\_min}})^2}{m_P^2}} > 0 & \text{if } f_{\text{MG\_min}} < f_{\text{MG}} < f_{\text{MG\_inter1}} \\ \dfrac{f^*_{\text{MG}} - f_{\text{MG}}}{m_{P2}} & \text{if } f_{\text{MG\_inter1}} \leq f_{\text{MG}} \leq f_{\text{MG\_inter2}} \\ -\sqrt{\dfrac{(f^*_{\text{MG}} - f_{\text{MG\_max}})^2 - (f_{\text{MG}} - f_{\text{MG\_max}})^2}{m_P^2}} < 0 & \text{if } f_{\text{MG\_inter2}} < f_{\text{MG}} < f_{\text{MG\_max}} \end{cases} \tag{3.7}$$

As illustrated in Fig. 3.4, $f_{\text{MG\_inter1}}$ and $f_{\text{MG\_inter2}}$ are the points of intersection of linear

and elliptic trajectories. Therefore, equalizing (3.3) and (3.6) results in $f_{\text{MG\_inter1}}$, as given below:

$$f_{\text{MG\_inter1}} = \frac{\sqrt{4(m_P^2 f_{\text{MG}}^* + m_{P2}^2 f_{\text{MG\_min}})^2 - 4(m_P^2 + m_{P2}^2)((m_p^2 - m_{P2}^2) f_{\text{MG}}^{*^2} + 2m_{P2}^2 f_{\text{MG}}^* f_{\text{MG\_min}})}}{-2(m_P^2 + m_{P2}^2)} + \frac{(m_P^2 f_{\text{MG}}^* + m_{P2}^2 f_{\text{MG\_min}})}{(m_P^2 + m_{P2}^2)}. \tag{3.8}$$

Similarly, $f_{\text{MG\_inter2}}$ can be calculated by equalizing (3.5) and (3.6), as follows:

$$f_{\text{MG\_inter2}} = \frac{\sqrt{4(m_P^2 f_{\text{MG}}^* + m_{P2}^2 f_{\text{MG\_max}})^2 - 4(m_P^2 + m_{P2}^2)((m_p^2 - m_{P2}^2) f_{\text{MG}}^{*^2} + 2m_{P2}^2 f_{\text{MG}}^* f_{\text{MG\_max}})}}{2(m_P^2 + m_{P2}^2)} + \frac{(m_P^2 f_{\text{MG}}^* + m_{P2}^2 f_{\text{MG\_max}})}{(m_P^2 + m_{P2}^2)}. \tag{3.9}$$

3.1.2 Voltage Dynamic-Response Improvement

This subsection presents a PLE droop to achieve an enhanced voltage profile for islanded microgrids during abnormal conditions. First, the voltage dynamic-response of the system is studied. Then, the detailed description of the proposed PLE method and comparison with linear droop are presented.

3.1.2.1 Voltage Dynamic-Response of the System

The continuity in voltage variations of ac bus leads to significant operational challenges for ensuring the stability of the system. Fig. 3.5 shows these voltage fluctuations during severe conditions, and the corresponding linear, i.e., the red line, and PLE, i.e., the blue line, Q-v droops employed in BESS. Similar to the previous section, both linear and PLE droops have the same start point and end point. Besides, utilizing the PLE droop results in injecting/absorbing more reactive power during abnormalities, leading to an improved voltage profile of the system. At point A, the system operates at its nominal voltage, i.e.,

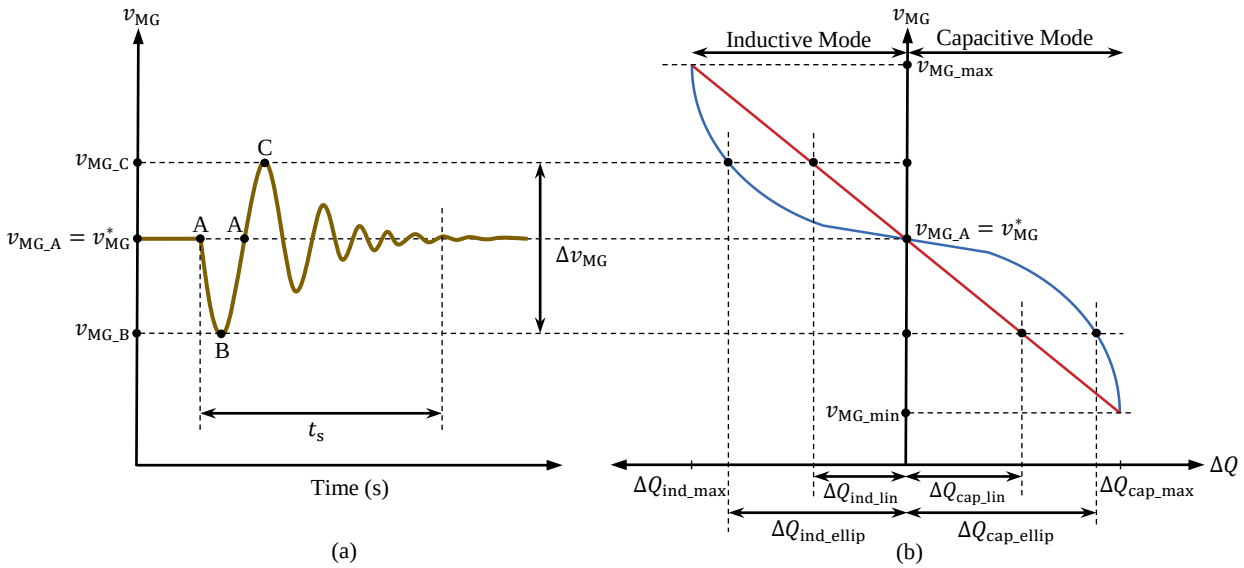

Figure 3.5: (a) Voltage variations of ac bus caused by abnormal conditions, and (b) corresponding linear (red line) and PLE (blue line) Q-v droops [95, 97].

$v_{MG} = v^*_{MG}$, and thus, the BESS is in idle mode, i.e., $\triangle Q = 0$. However, at point B, the ac-bus voltage falls below its nominal value, i.e., $v_{MG} < v^*_{MG}$, and hence, the BESS operates in capacitive mode, i.e., $\triangle Q > 0$, to inject the deficit reactive power into the system. On the other hand, at point C, the ac-bus voltage increases over its nominal value, i.e., $v_{MG} > v^*_{MG}$, and the BESS operates in inductive mode, i.e., $\triangle Q < 0$, to restore the voltage by absorbing the extra reactive power in the system.

For the linear Q-v droop with coefficient of m_Q, i.e., the red line in 3.5(b), the injected/absorbed reactive power by BESS can be calculated as follows:

$$\triangle Q_{lin} = \frac{v^*_{MG} - v_{MG}}{m_Q} = \begin{cases} \triangle Q_{cap\_lin} > 0 & \text{if } v_{MG} < v^*_{MG} \text{ (capacitive mode)} \\ 0 & \text{if } v_{MG} = v^*_{MG} \text{ (idle mode)} \\ \triangle Q_{ind\_lin} < 0 & \text{if } v_{MG} > v^*_{MG} \text{ (inductive mode)} \end{cases} \tag{3.10}$$

where v_{MG} and v^*_{MG} are the voltage of ac bus and its nominal value, respectively. $\triangle Q_{cap\_lin}$ is the reactive power injected by BESS during the capacitive mode, and $\triangle Q_{ind\_lin}$ is the reactive power absorbed by BESS during the inductive mode.

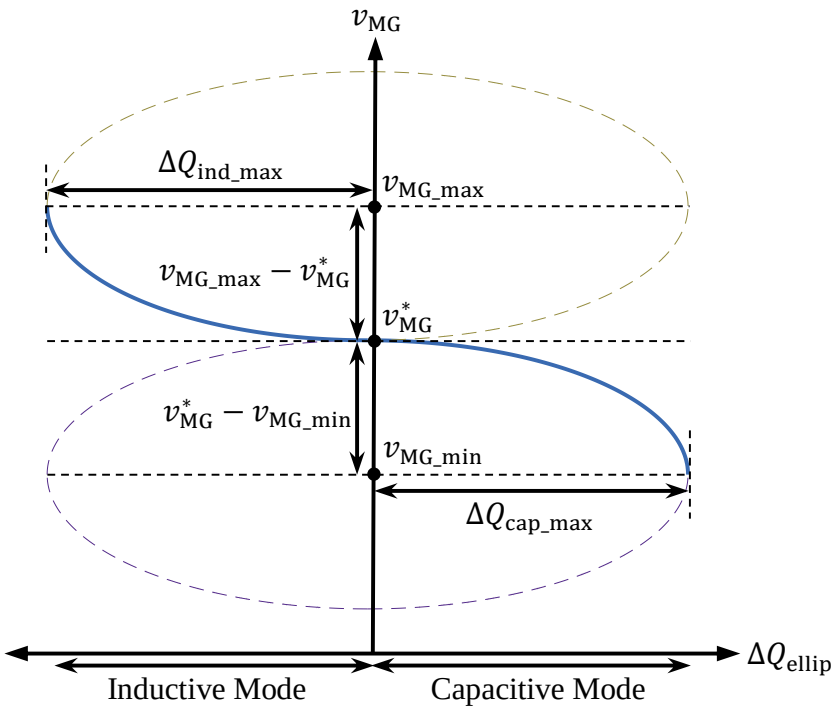

Figure 3.6: The elliptic trajectory (blue line) defined for inductive and capacitive modes of BESS.

3.1.2.2 Piecewise Linear-Elliptic (PLE) *Q-v* Droop

Due to the predetermination of voltage and reactive power range, defining a new trajectory instead of linear trajectory is a potential solution to achieve an enhanced voltage-dynamic response. As can be seen in Fig. 3.6, for the capacitive mode, the trajectory between the start point, i.e., v^*_{MG}, and the end point, i.e., $v_{\mathrm{MG\_min}}$, can be considered as a quarter ellipse centered at $v_{\mathrm{MG\_min}}$, whose horizontal radius is $\triangle Q_{\mathrm{cap\_max}}$ and vertical radius is $v^*_{\mathrm{MG}} - v_{\mathrm{MG\_min}}$. Herein, $\triangle Q_{\mathrm{cap\_max}}$ is the maximum reactive power that can be injected by BESS, which can be calculated from (3.10) as follows:

$$\triangle Q_{\mathrm{cap\_max}} = \frac{v^*_{\mathrm{MG}} - v_{\mathrm{MG\_min}}}{m_Q} > 0. \tag{3.11}$$

Considering the aforementioned quarter ellipse, the reactive power injected by BESS during the capacitive mode can be expressed as follows:

$$\triangle Q_{\text{cap\_ellip}} = \sqrt{\frac{(v^*_{\text{MG}} - v_{\text{MG\_min}})^2 - (v_{\text{MG}} - v_{\text{MG\_min}})^2}{m_Q^2}} > 0. \tag{3.12}$$

Another quarter ellipse can be considered for the inductive mode to connect the start point, i.e., v^*_{MG}, and the end point, i.e., $v_{\text{MG\_max}}$. This quarter ellipse is centered at $v_{\text{MG\_max}}$, with the horizontal radius of $\triangle Q_{\text{ind\_max}}$ and vertical radius of $v_{\text{MG\_max}} - v^*_{\text{MG}}$, see Fig. 3.6. Due to the predetermination of m_Q, $\triangle Q_{\text{ind\_max}}$ is the maximum reactive power that can be absorbed by BESS, which can be obtained from (3.10) as follows:

$$\triangle Q_{\text{ind\_max}} = \frac{v^*_{\text{MG}} - v_{\text{MG\_max}}}{m_Q} < 0. \tag{3.13}$$

Consequently, the reactive power absorbed by BESS during the inductive mode can be obtained as follows:

$$\triangle Q_{\text{ind\_ellip}} = -\sqrt{\frac{(v^*_{\text{MG}} - v_{\text{MG\_max}})^2 - (v_{\text{MG}} - v_{\text{MG\_max}})^2}{m_Q^2}} < 0. \tag{3.14}$$

As can be found from Fig. 3.6, the slope of elliptic trajectory, i.e., the blue line, is zero at the nominal voltage. Thus, a narrow linear region is defined around the nominal voltage as follows:

$$\triangle Q_{\text{lin2}} = \frac{v^*_{\text{MG}} - v_{\text{MG}}}{m_{Q2}}, \tag{3.15}$$

where m_{Q2} is the droop coefficient of narrow linear trajectory which should always be chosen less than m_Q.

The trajectory of proposed PLE droop for voltage dynamic-response enhancement of islanded microgrids is illustrated in Fig. 3.7. According to (3.12), (3.14), and (3.15), the injected/absorbed reactive power by BESS following the proposed PLE trajectory can be expressed as follows:

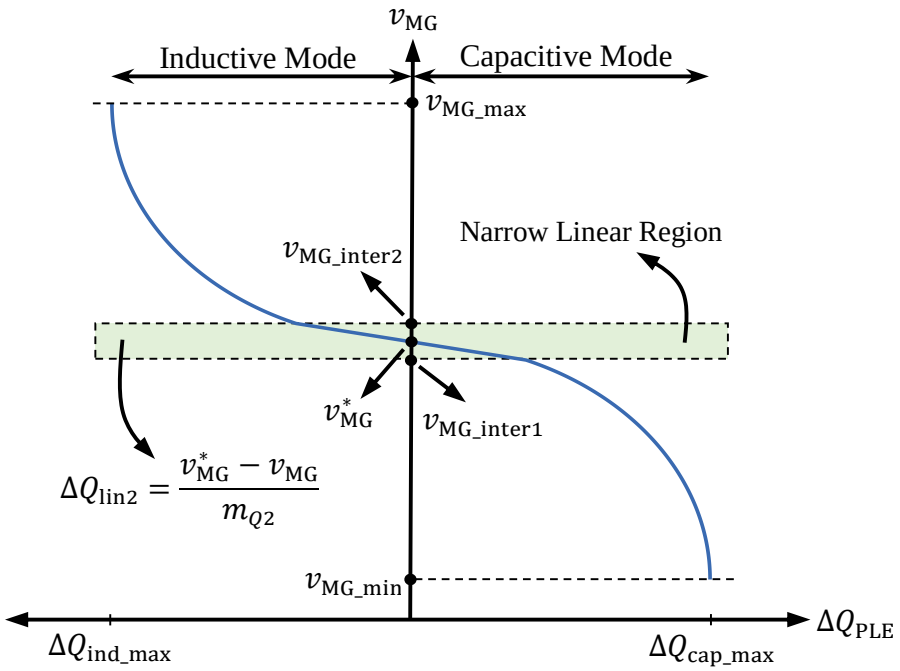

Figure 3.7: The PLE Q-v droop for voltage dynamic-response improvement [95].

$$\triangle Q_{\mathrm{PLE}} = \begin{cases} \sqrt{\dfrac{(v^*_{\mathrm{MG}} - v_{\mathrm{MG\_min}})^2 - (v_{\mathrm{MG}} - v_{\mathrm{MG\_min}})^2}{m_Q^2}} > 0 & \text{if } v_{\mathrm{MG\_min}} < v_{\mathrm{MG}} < v_{\mathrm{MG\_inter1}} \\ \dfrac{v^*_{\mathrm{MG}} - v_{\mathrm{MG}}}{m_{Q2}} & \text{if } v_{\mathrm{MG\_inter1}} \leq v_{\mathrm{MG}} \leq v_{\mathrm{MG\_inter2}} \\ -\sqrt{\dfrac{(v^*_{\mathrm{MG}} - v_{\mathrm{MG\_max}})^2 - (v_{\mathrm{MG}} - v_{\mathrm{MG\_max}})^2}{m_Q^2}} < 0 & \text{if } v_{\mathrm{MG\_inter2}} < v_{\mathrm{MG}} < v_{\mathrm{MG\_max}} \end{cases} \tag{3.16}$$

As can be seen in Fig. 3.7, $v_{\mathrm{MG\_inter1}}$ and $v_{\mathrm{MG\_inter2}}$ are the points of intersection of linear and elliptic trajectories. Therefore, $v_{\mathrm{MG\_inter1}}$ can be obtained by equalizing (3.12) and (3.15), as given below:

$$v_{\mathrm{MG\_inter1}} = \frac{\sqrt{4(m_Q^2 v^*_{\mathrm{MG}} + m_{Q2}^2 v_{\mathrm{MG\_min}})^2 - 4(m_Q^2 + m_{Q2}^2)((m_Q^2 - m_{Q2}^2)v^{*2}_{\mathrm{MG}} + 2m_{Q2}^2 v^*_{\mathrm{MG}} v_{\mathrm{MG\_min}})}}{-2(m_Q^2 + m_{Q2}^2)} + \frac{(m_Q^2 v^*_{\mathrm{MG}} + m_{Q2}^2 v_{\mathrm{MG\_min}})}{(m_Q^2 + m_{Q2}^2)}. \tag{3.17}$$

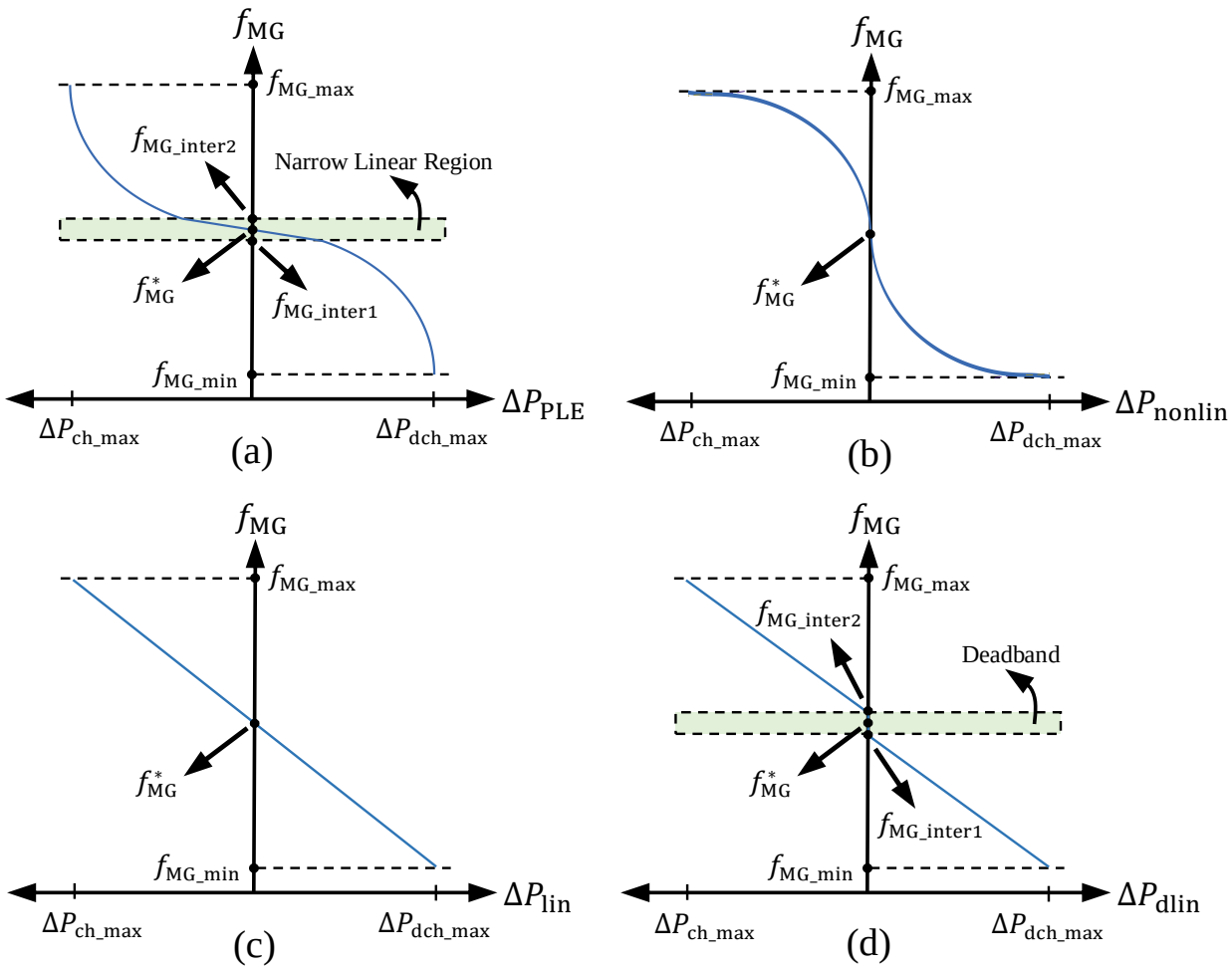

Figure 3.8: PLE *P-f* droop versus other conventional *P-f* droops for dynamic-response enhancement in islanded microgrids. (a) PLE, (b) Nonlinear, (c) Linear, (d) Linear with deadband [95].

Besides, equalizing (3.14) and (3.15) results in $v_{\mathrm{MG\_inter2}}$ as follows:

$$v_{\mathrm{MG\_inter2}} = \frac{\sqrt{4(m_Q^2 v^*_{\mathrm{MG}} + m_{Q2}^2 v_{\mathrm{MG\_max}})^2 - 4(m_Q^2 + m_{Q2}^2)((m_Q^2 - m_{Q2}^2)v^{*2}_{\mathrm{MG}} + 2m_{Q2}^2 v^*_{\mathrm{MG}} v_{\mathrm{MG\_max}})}}{2(m_Q^2 + m_{Q2}^2)} + \frac{(m_Q^2 v^*_{\mathrm{MG}} + m_{Q2}^2 v_{\mathrm{MG\_max}})}{(m_Q^2 + m_{Q2}^2)}. \tag{3.18}$$

3.1.3 PLE Droops vs. Other Conventional Droops

This subsection provides a comparison between the proposed PLE droops and other conventional droops employed for dynamic-behavior improvement in islanded microgrids, see Figs. 3.8 and 3.9. As can be found from Figs. 3.8(b) and 3.9(b), compared with proposed PLE droops, implementing nonlinear droops [98] results in injecting/absorbing less amount of active and reactive power during abnormal conditions. This means that the system will need more time to restore the voltage and frequency after a severe condition. Therefore, the nonlinear droop methods are typically utilized in dc and ac microgrids for achieving an enhanced power sharing between different DG units during the steady-state

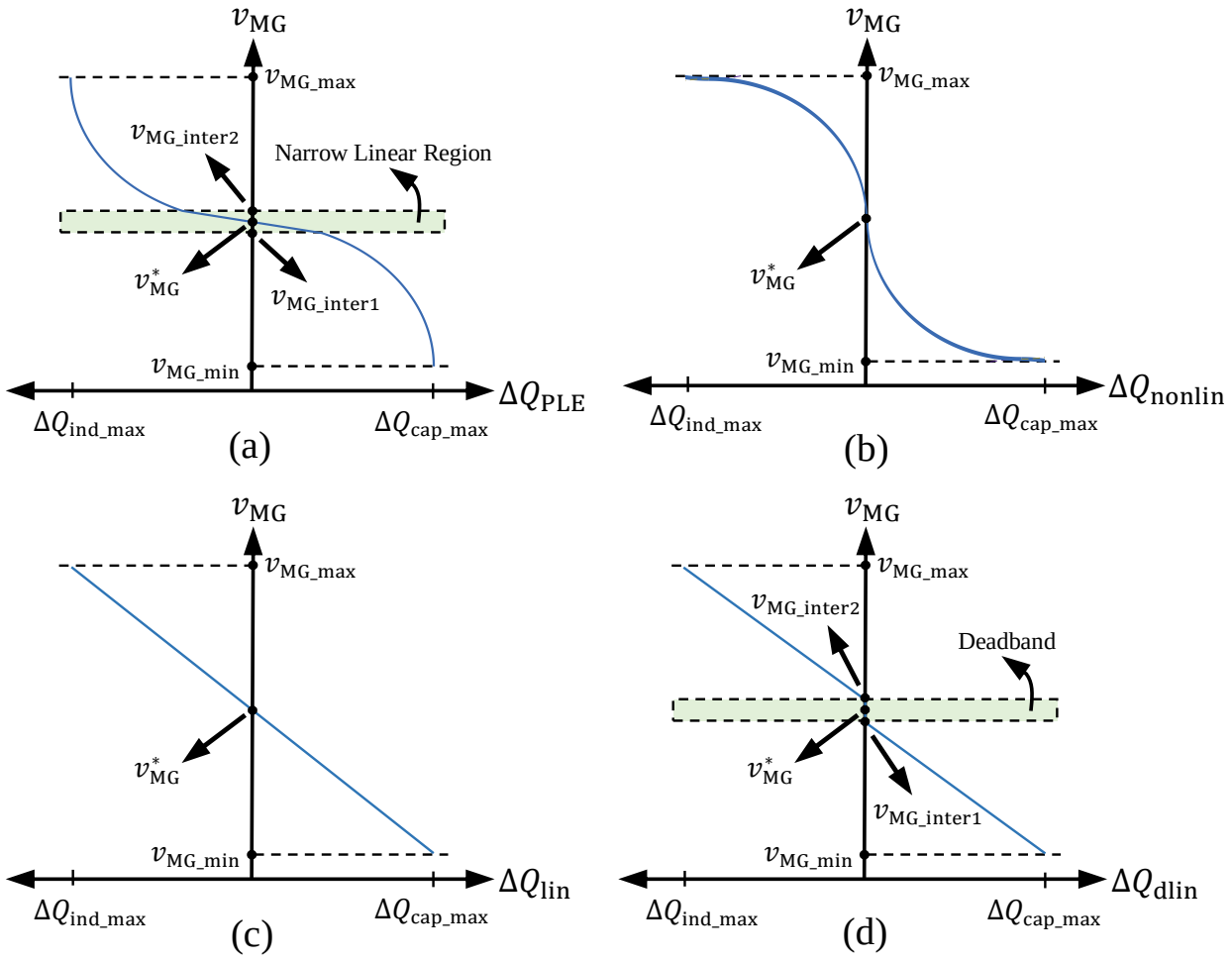

Figure 3.9: PLE Q-v droop versus other conventional Q-v droops for dynamic-response enhancement in islanded microgrids. (a) PLE, (b) Nonlinear, (c) Linear, (d) Linear with deadband.

condition [99, 100]. On the other hand, in some applications, the linear trajectories are implemented with a deadband around the nominal voltage and frequency, see Figs. 3.8(d) and 3.9(d). The injected/absorbed active and reactive power by BESS for the aforementioned linear droops with deadband are given below:

$$\triangle P_{\text{dlin}} = \begin{cases} \dfrac{(f_{\text{MG\_inter1}} - f_{\text{MG}})(f^*_{\text{MG}} - f_{\text{MG\_min}})}{m_P(f_{\text{MG\_inter1}} - f_{\text{MG\_min}})} > 0 & \text{if } f_{\text{MG\_min}} < f_{\text{MG}} < f_{\text{MG\_inter1}} \\ 0 & \text{if } f_{\text{MG\_inter1}} \leq f_{\text{MG}} \leq f_{\text{MG\_inter2}} \\ \dfrac{(f_{\text{MG\_inter2}} - f_{\text{MG}})(f^*_{\text{MG}} - f_{\text{MG\_max}})}{m_P(f_{\text{MG\_inter2}} - f_{\text{MG\_max}})} < 0 & \text{if } f_{\text{MG\_inter2}} < f_{\text{MG}} < f_{\text{MG\_max}} \end{cases} \tag{3.19}$$

$$\triangle Q_{\text{dlin}} = \begin{cases} \dfrac{(v_{\text{MG\_inter1}} - v_{\text{MG}})(v^*_{\text{MG}} - v_{\text{MG\_min}})}{m_Q(v_{\text{MG\_inter1}} - v_{\text{MG\_min}})} > 0 & \text{if } v_{\text{MG\_min}} < v_{\text{MG}} < v_{\text{MG\_inter1}} \\ 0 & \text{if } v_{\text{MG\_inter1}} \leq v_{\text{MG}} \leq v_{\text{MG\_inter2}} \\ \dfrac{(v_{\text{MG\_inter2}} - v_{\text{MG}})(v^*_{\text{MG}} - v_{\text{MG\_max}})}{m_Q(v_{\text{MG\_inter2}} - v_{\text{MG\_max}})} < 0 & \text{if } v_{\text{MG\_inter2}} < v_{\text{MG}} < v_{\text{MG\_max}} \end{cases} \tag{3.20}$$

Comparing (3.1) and (3.10), respectively, with (3.19) and (3.20) leads to the fact that implementation of deadbands results in injection/absorption of less active and reactive power by BESS which is not preferable during abnormal conditions. Besides, the system performance is very dependent to the length of the deadband, and larger deadbands might cause abrupt changes in the active and reactive power of BESS while the voltage and frequency of ac bus are going back and forth inside the deadband and outside of it. In contrast, the presence of narrow linear regions in the proposed PLE droops helps the BESS to operate smoother during abnormal conditions.

3.2 PV Fed Smart Inverters for Enhanced Voltage and Frequency Regualtion in Islanded Mixed-Inertia Microgrids

In this section, the traditional controller of PV units is deployed to enhance the dynamic response of islanded mixed-inertia microgrids by mitigating the voltage and frequency fluctuations. An APD is proposed and employed in PV units to achieve a faster active power balance between generation and consumption during abnormalities, leading to an enhanced frequency response. Besides, a Q-v droop is implemented in the reactive-power control loop of PV units enabling them to inject/absorb reactive power during abnormalities and participate in voltage-profile enhancement of the system.

3.2.1 Dynamic-Response Enhancement

The schematic of islanded mixed-inertia microgrid under study is shown in Fig. 3.10. A diesel generator is responsible for the primary voltage and frequency control of the main ac bus using an AVR and governor. The BESS is operating as a backup to inject/absorb the deficit/extra power during the steady-state condition. In addition, the system consists of n paralleled PV units equipped with the proposed droops to deal with voltage and frequency variations of ac bus in case of abnormal conditions. This utilization of droops changes the operation mode of PV units from grid-feeding control mode to grid-supporting control mode. The frequency deviations of ac bus during the settling time of $t_{\rm s}$ are shown in Fig. 3.11(a). At point A, the system operates at its nominal frequency, i.e., $f^{*}_{\rm MG}$. However, during the transients, the frequency of ac bus deviates which might lead to blackouts. For instance, at point B, the ac-bus frequency is lower than its nominal value, whereas the system suffers from high frequency at point C. As illustrated in Fig. 3.11(b), the ac-bus frequency, i.e., $f_{\rm MG}$, and injected active power, i.e., $P_{\rm PV}$, are independent of each other when the PV unit is operating in grid-feeding control mode. Thus, in order to mitigate these short-term frequency

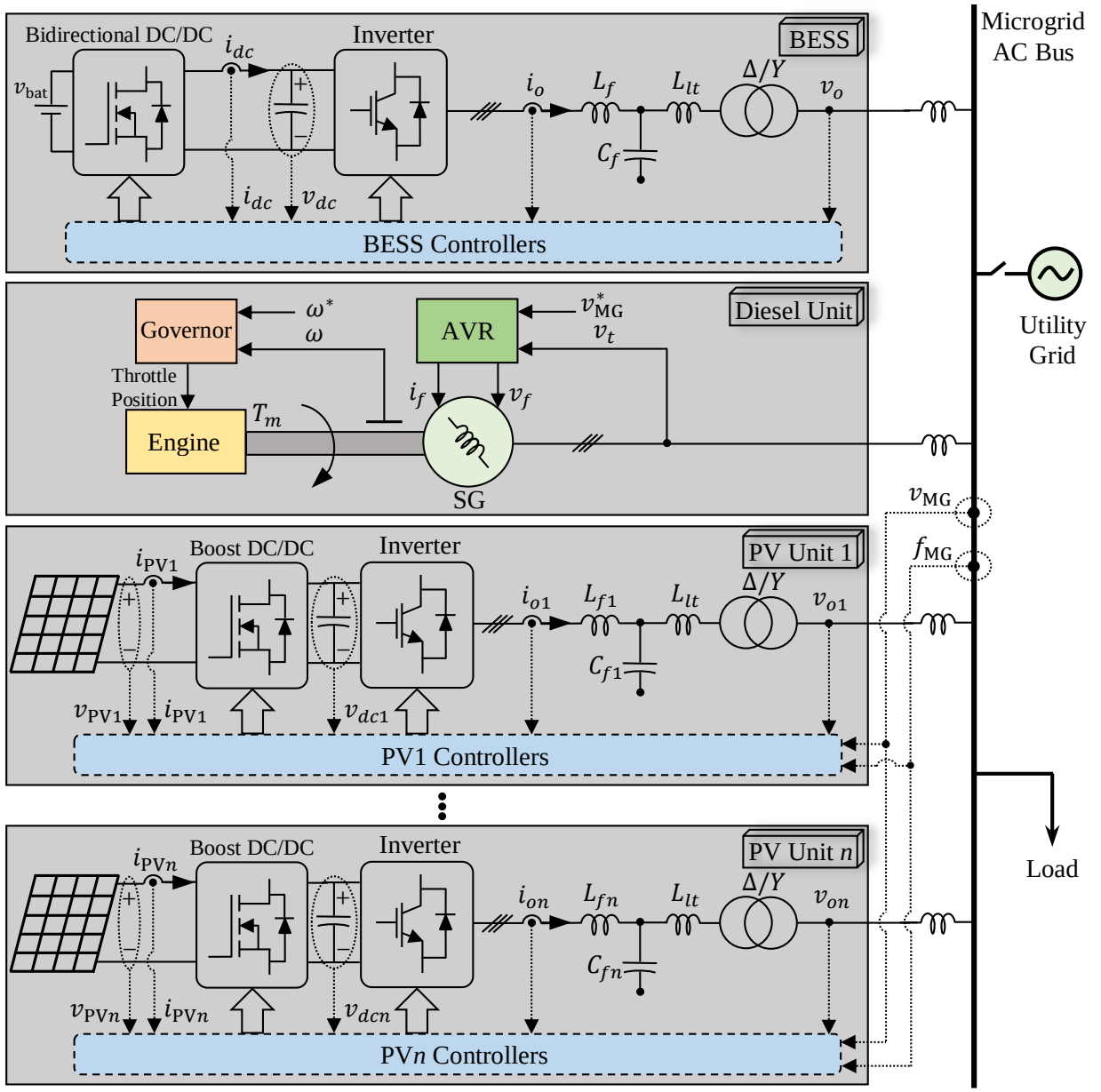

Figure 3.10: Configuration of the islanded mixed-inertia microgrid with paralleled PV units [101].

fluctuations, the APD is implemented in PV unit to cover the active power mismatches between generation and consumption during abnormalities, see Fig. 3.11(b).

Depending on the frequency of ac bus, three modes of operation can be defined for PV unit: under frequency (UF), over frequency (OF), and steady state. As can be found from Fig. 3.11(b), in case of UF, the increased amount of active power by PV unit for compensating the deficit active power can be obtained as follows:

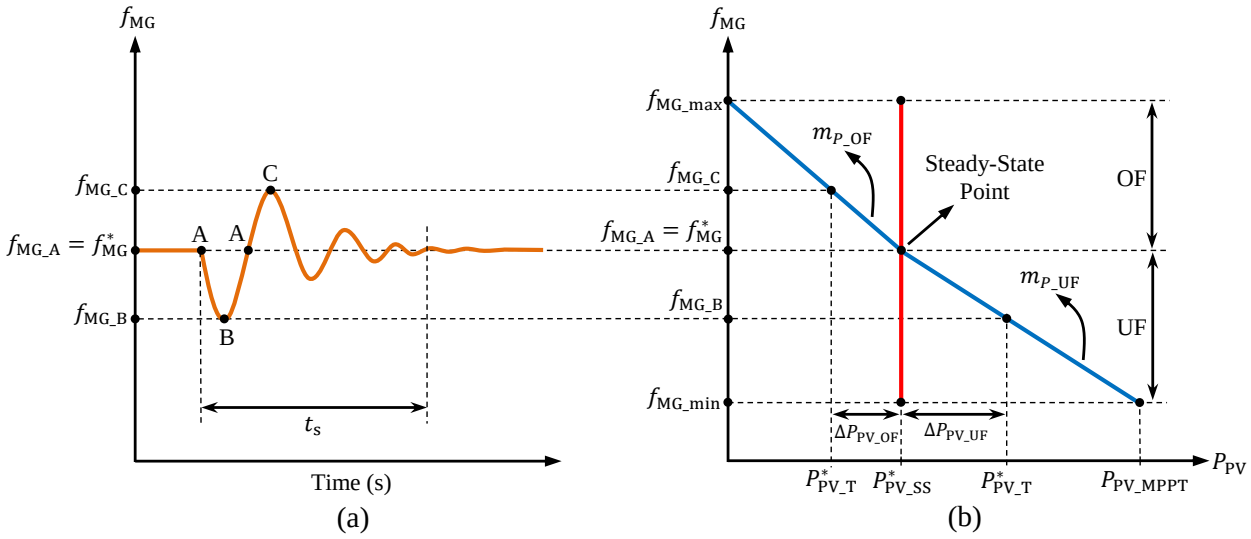

Figure 3.11: (a) Frequency variations of ac bus caused by abnormal conditions, and (b) the proposed APD for grid-supporting controlled PV unit (blue line) versus *P-f* characteristic of grid-feeding controlled PV unit (red line).

$$\triangle P_{\mathrm{PV\_UF}} = \frac{f^*_{\mathrm{MG}} - f_{\mathrm{MG}}}{m_{P\_\mathrm{UF}}} > 0, \tag{3.21}$$

where f_{MG} and f^*_{MG} are the frequency of ac bus and its nominal value, respectively. m_{P_UF} is the droop coefficient of APD during UF, which can be calculated as follows:

$$m_{P\_\mathrm{UF}} = \frac{f^*_{\mathrm{MG}} - f_{\mathrm{MG\_min}}}{P_{\mathrm{PV\_MPPT}} - P^*_{\mathrm{PV\_SS}}}, \tag{3.22}$$

where $P_{\mathrm{PV\_MPPT}}$ is the maximum available power that can be injected by PV unit obtained by the maximum power point tracking (MPPT) algorithm, and $P^*_{\mathrm{PV\_SS}}$ is the active-power setpoint of PV unit during the steady-state condition.

Similarly, as illustrated in Fig. 3.11(b), during the OF, the active-power setpoint of PV unit decreases by a certain amount, which can be obtained as follows:

$$\triangle P_{\mathrm{PV\_OF}} = \frac{f^*_{\mathrm{MG}} - f_{\mathrm{MG}}}{m_{P\_\mathrm{OF}}} < 0, \tag{3.23}$$

where m_{P_OF} is the droop coefficient of APD during OF, and can be calculated as follows:

$$m_{P\_\mathrm{OF}} = \frac{f_{\mathrm{MG\_max}} - f^*_{\mathrm{MG}}}{P^*_{\mathrm{PV\_SS}}}. \tag{3.24}$$

The increased/decreased amount of PV active power from its steady-state setpoint can be obtained from (3.21), (3.22), (3.23), and (3.24) as given below:

$$\triangle P_{\mathrm{PV}} = \begin{cases} \triangle P_{\mathrm{PV\_UF}} = \dfrac{(P_{\mathrm{PV\_MPPT}} - P^*_{\mathrm{PV\_SS}})(f^*_{\mathrm{MG}} - f_{\mathrm{MG}})}{f^*_{\mathrm{MG}} - f_{\mathrm{MG\_min}}} > 0 & \text{if } f_{\mathrm{MG\_min}} < f_{\mathrm{MG}} < f^*_{\mathrm{MG}} \\ 0 & \text{if } f_{\mathrm{MG}} = f^*_{\mathrm{MG}} \\ \triangle P_{\mathrm{PV\_OF}} = \dfrac{P^*_{\mathrm{PV\_SS}}(f^*_{\mathrm{MG}} - f_{\mathrm{MG}})}{f_{\mathrm{MG\_max}} - f^*_{\mathrm{MG}}} < 0 & \text{if } f^*_{\mathrm{MG}} < f_{\mathrm{MG}} < f_{\mathrm{MG\_max}} \end{cases} \tag{3.25}$$

The APDs of PV unit 1 to PV unit n are shown in Fig. 3.12. These curves can be combined into a single equivalent APD that describes the behavior of all paralleled PV units during abnormal conditions. Hence, the total increase/decrease in active-power setpoint of PV units during abnormalities can be obtained as follows:

$$\triangle P_{\mathrm{PV\_eq}} = \triangle P_{\mathrm{PV1}} + \triangle P_{\mathrm{PV2}} + ... + \triangle P_{\mathrm{PV}n} = \sum_{i=1}^{n} \triangle P_{\mathrm{PV}i}. \tag{3.26}$$

According to (3.25), (3.26) can be rewritten as follows:

$$\triangle P_{\mathrm{PV\_eq}} = \begin{cases} \dfrac{(\sum_{i=1}^{n} P_{\mathrm{PV}i\_\mathrm{MPPT}} - \sum_{i=1}^{n} P^*_{\mathrm{PV}i\_\mathrm{SS}})(f^*_{\mathrm{MG}} - f_{\mathrm{MG}})}{f^*_{\mathrm{MG}} - f_{\mathrm{MG\_min}}} > 0 & \text{if } f_{\mathrm{MG\_min}} < f_{\mathrm{MG}} < f^*_{\mathrm{MG}} \\ 0 & \text{if } f_{\mathrm{MG}} = f^*_{\mathrm{MG}} \\ \dfrac{\sum_{i=1}^{n} P^*_{\mathrm{PV}i\_\mathrm{SS}}(f^*_{\mathrm{MG}} - f_{\mathrm{MG}})}{f_{\mathrm{MG\_max}} - f^*_{\mathrm{MG}}} < 0 & \text{if } f^*_{\mathrm{MG}} < f_{\mathrm{MG}} < f_{\mathrm{MG\_max}} \end{cases} \tag{3.27}$$

In order to improve the voltage profile of the system during abnormalities, a linear Q-v droop with coefficient of m_Q can be defined. The injected/absorbed reactive power by PV unit during under voltage (UV), over voltage (OV), and steady-state conditions can be obtained as follows:

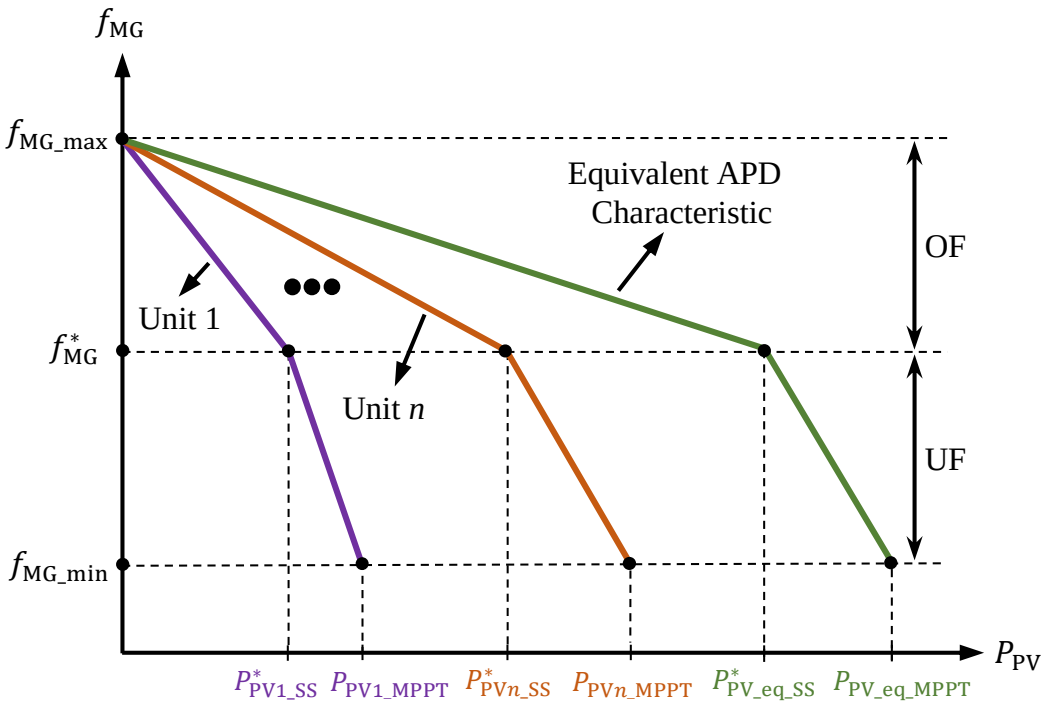

Figure 3.12: The APDs of PV units and the equivalent APD of all paralleled PV units representing their behavior during abnormal conditions.

$$\triangle Q_{PV} = \frac{v^*_{MG} - v_{MG}}{m_Q} = \begin{cases} \triangle Q_{PV\_UV} > 0 & \text{if } v_{MG} < v^*_{MG} \text{ (UV)} \\ 0 & \text{if } v_{MG} = v^*_{MG} \text{ (steady state)} \\ \triangle Q_{PV\_OV} < 0 & \text{if } v_{MG} > v^*_{MG} \text{ (OV)} \end{cases} \tag{3.28}$$

The modified control scheme of an individual PV unit equipped with proposed droops is illustrated in Fig. 3.13. Employing the proposed droops results in adding/subtracting $\triangle P^*_{PV}$ and $\triangle Q^*_{PV}$ to/from $P^*_{PV\_SS}$ and $Q^*_{PV\_SS}$, respectively. This leads to an improved dynamic response for islanded microgrids during abnormal conditions.

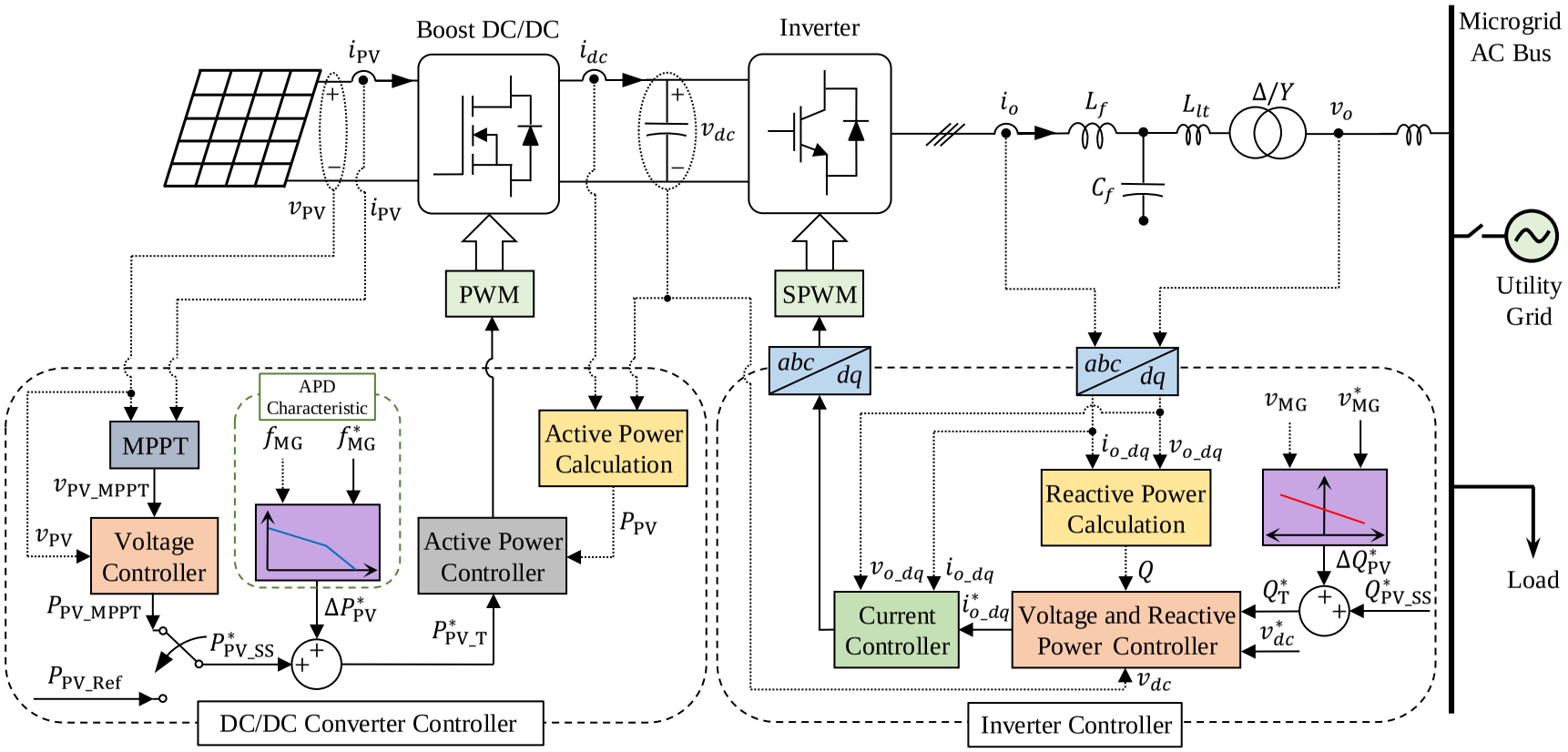

Figure 3.13: Modified control scheme of an individual PV unit equipped with proposed droops.

Table 3.1: System Parameters for Islanded Microgrid shown in Fig. 3.1

	Parameter	Value
DGs	Battery Operating Voltage Range	360-600 V
	Battery Rated Energy	101 kWh
	PV Maximum Power	50 kW
	Diesel Generator Maximum Power	127 kW
	Diesel Generator Inertia Constant (H)	0.3 s
Linear and PLE Droops	f^*_{MG}	60 Hz
	$f_{\text{MG\_min}}$	58 Hz
	$f_{\text{MG\_max}}$	62 Hz
	v^*_{MG} (line − to − line)	480 V
	$v_{\text{MG\_min}}$ (line − to − line)	400 V
	$v_{\text{MG\_max}}$ (line − to − line)	560 V
	m_P	0.05 Hz/kW
	m_{P2}	0.02 Hz/kW
	m_Q	13 V/kVAr
	m_{Q2}	4 V/kVAr

3.3 Verification

This section investigates the viability of proposed droop control methods in dynamic-response enhancement of islanded mixed-inertia microgrids. To this end, first, the case study results for cooperative role of BESS equipped with PLE droops are presented, and then, the effectiveness of utilizing APD in control scheme of PV units is demonstrated.

3.3.1 PLE Droops

In this subsection, different case studies are carried out to compare the performance of linear and PLE droops in dynamic-response enhancement of microgrids. For this purpose, the detailed model of islanded microgrid shown in Fig. 3.1 is developed in PSCAD/EMTDC environment, with the parameters listed in Table 3.1. Due to the fast response of BESS, the linear (with and without deadband) and PLE droops are implemented in it (one at a time) to inject the active/reactive power during under frequency/voltage, and absorb the active/reactive power in case of over frequency/voltage.

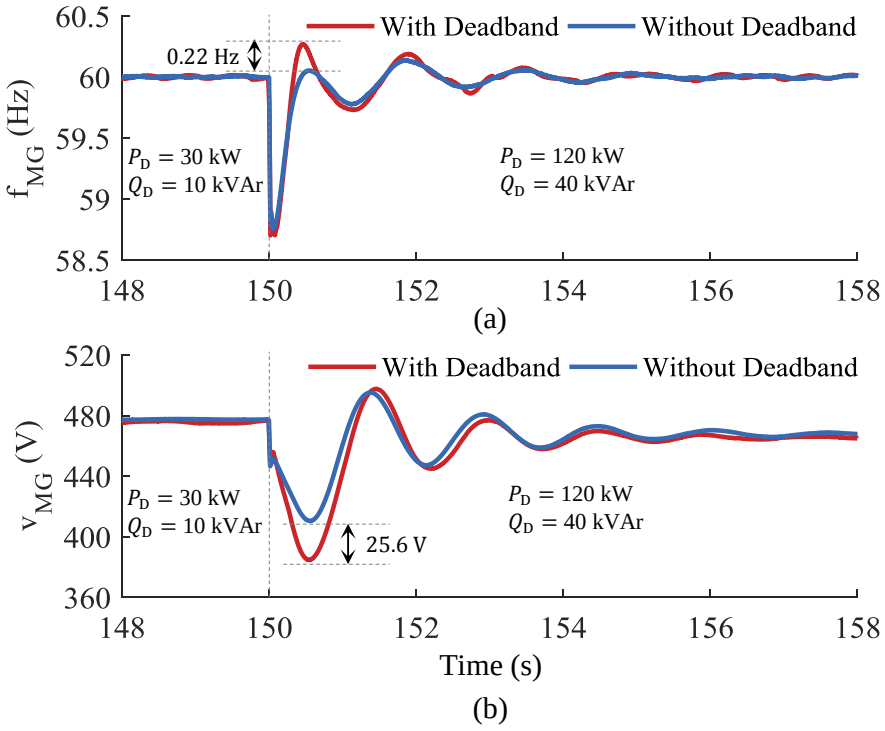

Figure 3.14: Case study 1: (a) frequency and (b) voltage variations of ac bus in the presence and absence of deadbands in linear droops when the load demand is stepped up.

3.3.1.1 Case Study 1: Linear Droops with and without Deadband

The first case study investigates the dynamic performance of the system with and without implementation of deadband in linear droops. Due to the islanding operation of microgrid, the diesel generator is responsible for primary regulation of voltage and frequency. The active and reactive power demand, i.e., P_{D} and Q_{D}, are initially 30 kW and 10 kVAr. At $t = 150$ s, the active and reactive power demand step up to 120 kW and 30 kVAr. As indicated in Fig. 3.14, both voltage and frequency profiles are improved in the absence of deadbands, which is due to the injection/absorption of more active and reactive power during abnormal conditions. It can be observed that the frequency overshoot is decreases from 60.27 Hz to 60.05 Hz, while the voltage drop is increased from 384.8 V to 410.4 V.

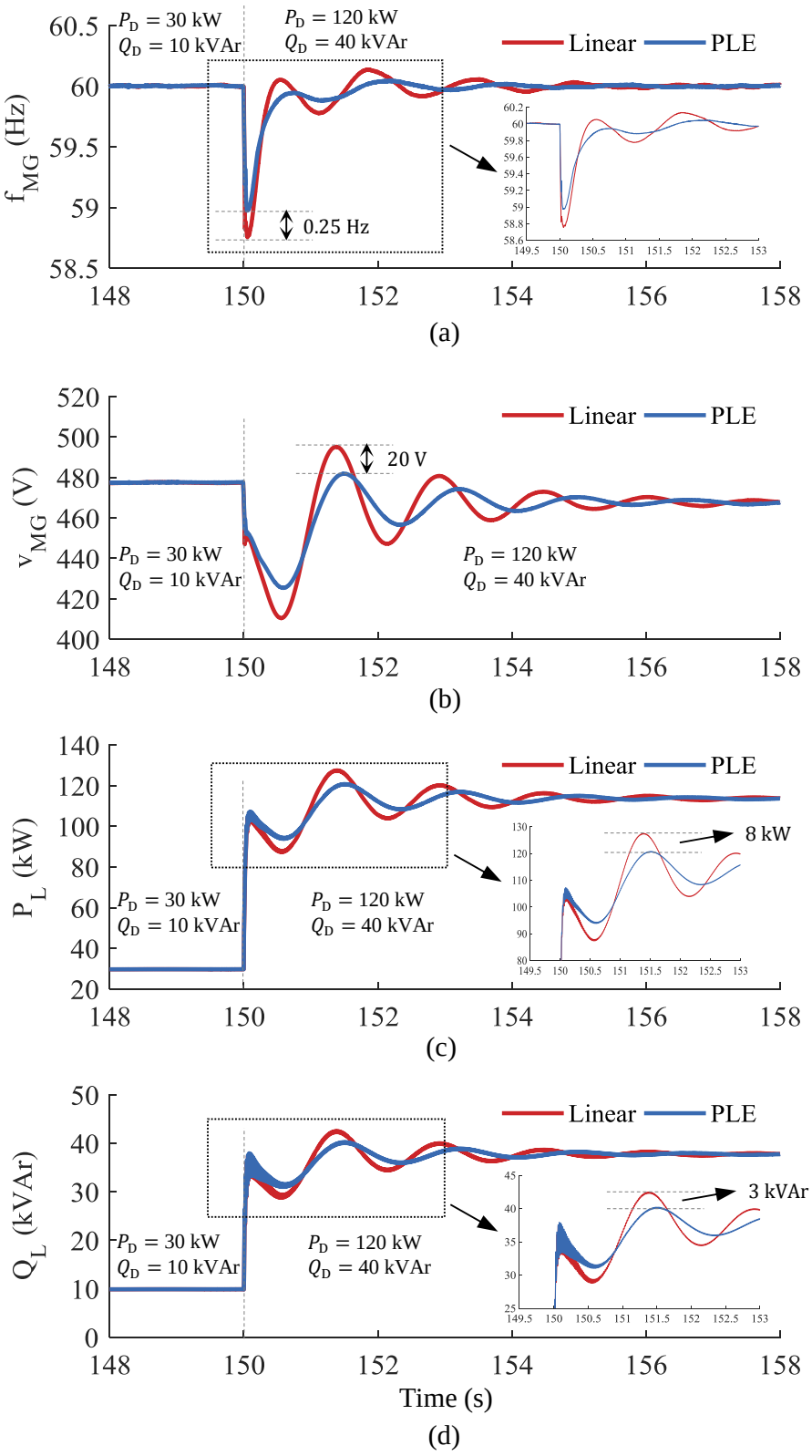

Figure 3.15: Case study 2: comparison between linear and PLE droops in dynamic-performance improvement of the system when the load demand is stepped up. (a) AC-bus frequency. (b) AC-bus voltage. (c) Load active power. (d) Load reactive power.

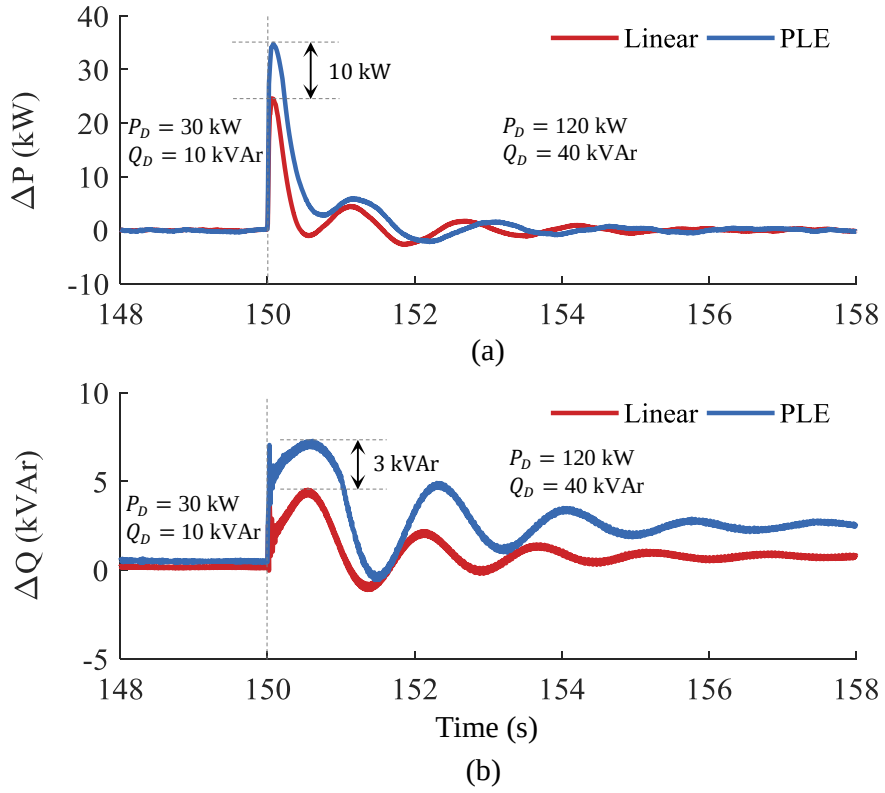

Figure 3.16: Case study 2: comparison between the injected/absorbed (a) active and (b) reactive power by BESS when the load demand is stepped up.

3.3.1.2 Case Study 2: PLE Droops vs. Linear Droops for Load Step-Up

This case study compares the effect of utilizing linear and PLE droops on dynamic-performance improvement of the system when the load demand is stepped up. The load step change is same as the previous case study, and as indicated in Figs. 3.15(a) and 3.15(b), the proposed PLE droops help the system to have enhanced frequency and voltage responses with shorter settling times. Compared to the case with linear P-f droop, implementing the PLE P-f droop results in improving the frequency nadir by about 0.25 Hz, see Fig. 3.15(a). Moreover, as illustrated in Fig. 3.15(b), the fluctuations of ac-bus voltage are significantly mitigated by employing the proposed PLE Q-v droop, while the voltage amplitude is reduced by about 20 V. The active and reactive power of the load, i.e., P_{L} and Q_{L}, are shown in Figs. 3.15(c) and 3.15(d), respectively, comparing the linear and PLE droops. It can be seen that by employing the PLE droops, the system requires less amount of time to meet the new load

Table 3.2: Case Study 2: Dynamic Performance Comparison of Microgrid with Linear and PLE Droops for a Step Change in Load Demand

	With Linear		**With PLE**	
	Settling Time	Overshoot	Settling Time	Overshoot
f_{MG}	6 s	0.1371 Hz	2 s	0.0472 Hz
v_{MG}	4 s	30 V	2.5 s	10 V
P_{L}	4 s	17 kW	3 s	9 kW
Q_{L}	4 s	5 kVAr	3 s	2 kVAr

demand, while the active and reactive power fluctuations of the load are mitigated. This improvement in the dynamic behavior of the system is due to the injecting/absorbing more active and reactive power by BESS, i.e., $\triangle P$ and $\triangle Q$, when the PLE droops are applied, see Figs. 3.16(a) and 3.16(b). Table 3.2 summarizes the comparison between the effect of utilizing linear and PLE droops on dynamic-performance enhancement of islanded microgrid, based on the results demonstrated in Fig. 3.15. From Table 3.2, utilizing the proposed PLE droops results in remarkable improvement in the dynamic behavior of microgrid for a step change in load demand.

3.3.1.3 Case Study 3: PLE Droops vs. Linear Droops for Load Step-Down

This case study investigates the dynamic response of microgrid to a large load step-down. Before $t = 150$ s, the active and reactive power demand are $P_{\mathrm{D}} = 120$ kW and $Q_{\mathrm{D}} = 40$ kVAr. At $t = 150$ s, the active and reactive power demand step down to 30 kW and 10 kVAr, resulting in short-term frequency and voltage fluctuations, see Figs. 3.17(a) and 3.17(b). As shown in Fig. 3.17(a), employing the PLE *P-f* droop reduces the frequency peak by about 0.3 Hz, leading to a significant enhancement in the frequency response of the system. On the other hand, as illustrated in Fig. 3.17(b), a considerable mitigation in voltage variations of ac bus is achieved by utilizing the proposed PLE *Q-v* droop. It can also be observed that with implementation of linear *Q-v* droop, the system requires almost 9 s to restore the voltage, and this is due to the inertia of diesel generator. However, the proposed PLE droop helps the system to reduce the settling time of voltage response to less than 4 s. Figs. 3.17(c) and 3.17(d) demonstrate the effectiveness of the proposed PLE droops in

mitigating the fluctuations of load active and reactive power, i.e., P_{L} and Q_{L}, when the load demand is stepped down.

3.3.1.4 Case Study 4: PLE Droops vs. Linear Droops for Transition from Grid-Connected to Islanded Mode

Low-inertia power generation units make islanded microgrids more vulnerable to the voltage and frequency fluctuations in comparison with grid-connected microgrids. This case study investigates the merits of proposed PLE characteristics in suppressing the short-term voltage and frequency variations during the transition from grid-connected to islanded mode of operation. The load demand remains constant during this case study ($P_{\mathrm{D}} = 60$ kW and $Q_{\mathrm{D}} = 20$ kVAr). The microgrid is initially operating in grid-connected mode and at $t = 150$ s, the grid operator disconnects it from the utility grid.

Fig. 3.18 compares the effect of utilizing linear and PLE droops in dynamic-response improvement of the system. As can be seen in Fig. 3.18(a), with the implementation of PLE *P-f* droop, a faster frequency restoration is achieved, while the frequency overshoot is decreased from 61.1 Hz to 60.8 Hz. Similarly, as shown in Fig. 3.18(b), the proposed PLE *Q-v* characteristic suppresses the voltage fluctuations of ac bus during the transition from grid-connected to islanded mode, while the voltage amplitude is reduced from 540 V to 523 V. Moreover, without implementation of PLE droop, the system requires almost 9 s to restore the voltage. However, the proposed PLE characteristic helps the system to restore the ac-bus voltage in less than 5 s, see Fig. 3.18(b). The fluctuations of P_{L} and Q_{L} are analyzed in Figs. 3.18(c) and 3.18(d), respectively, comparing the linear and PLE droops. It can be observed that equipping BESS with the proposed PLE droops leads to a considerable mitigation in fluctuations of P_{L} and Q_{L} during abnormal conditions. As illustrated in Figs. 3.19(a) and 3.19(b), when the system is connected to the grid, the injected/absorbed active and reactive power by BESS, i.e., $\triangle P$ and $\triangle Q$, are almost equal to zero, and this is because of the tight regulation of both voltage and frequency at their nominal values by the utility grid. However, after disconnecting the system from the grid, the BESS starts injecting/absorbing active and

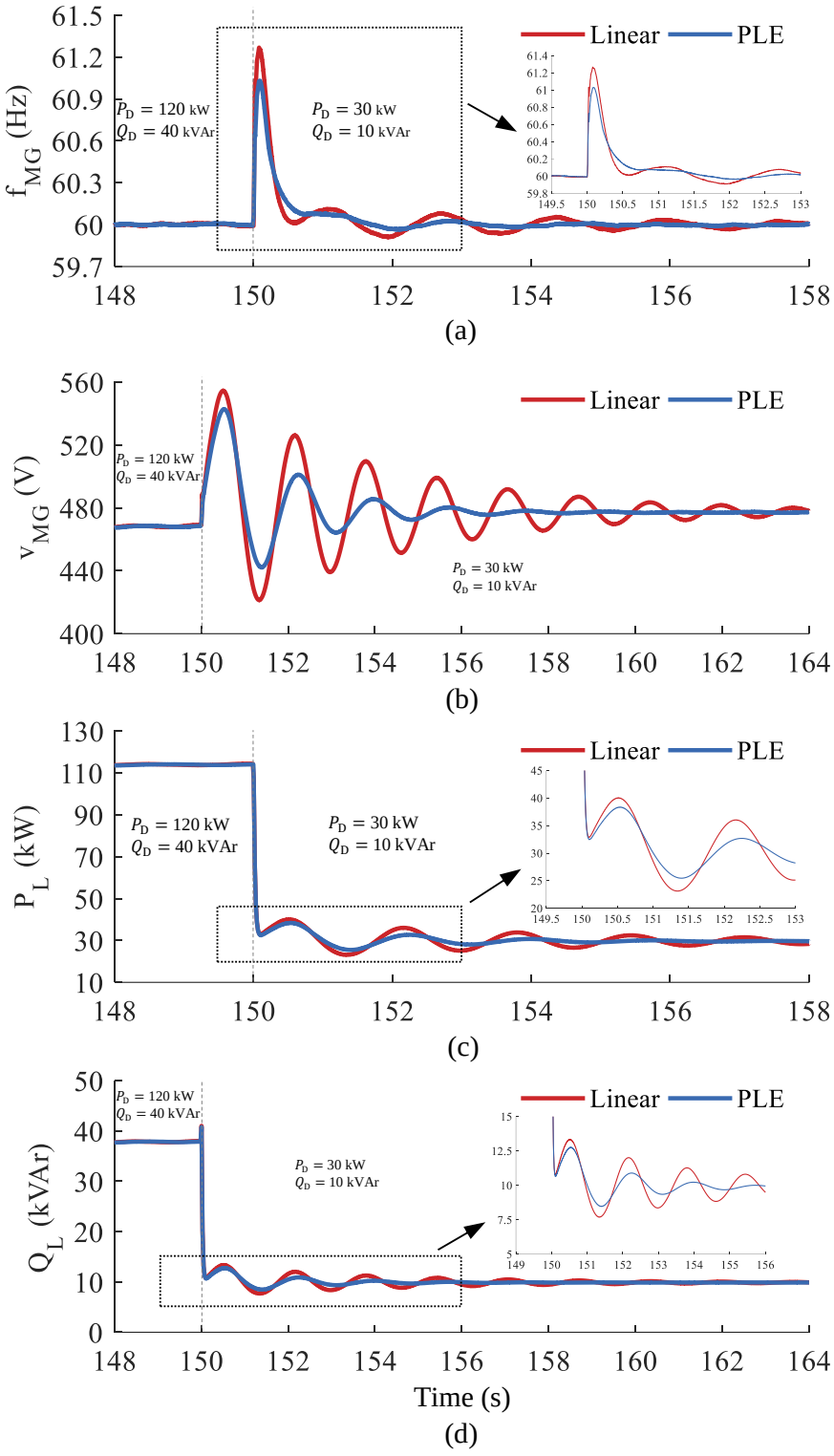

Figure 3.17: Case study 3: comparison between linear and PLE droops in dynamic-performance improvement of the system when the load demand is stepped down. (a) AC-bus frequency. (b) AC-bus voltage. (c) Load active power. (d) Load reactive power.

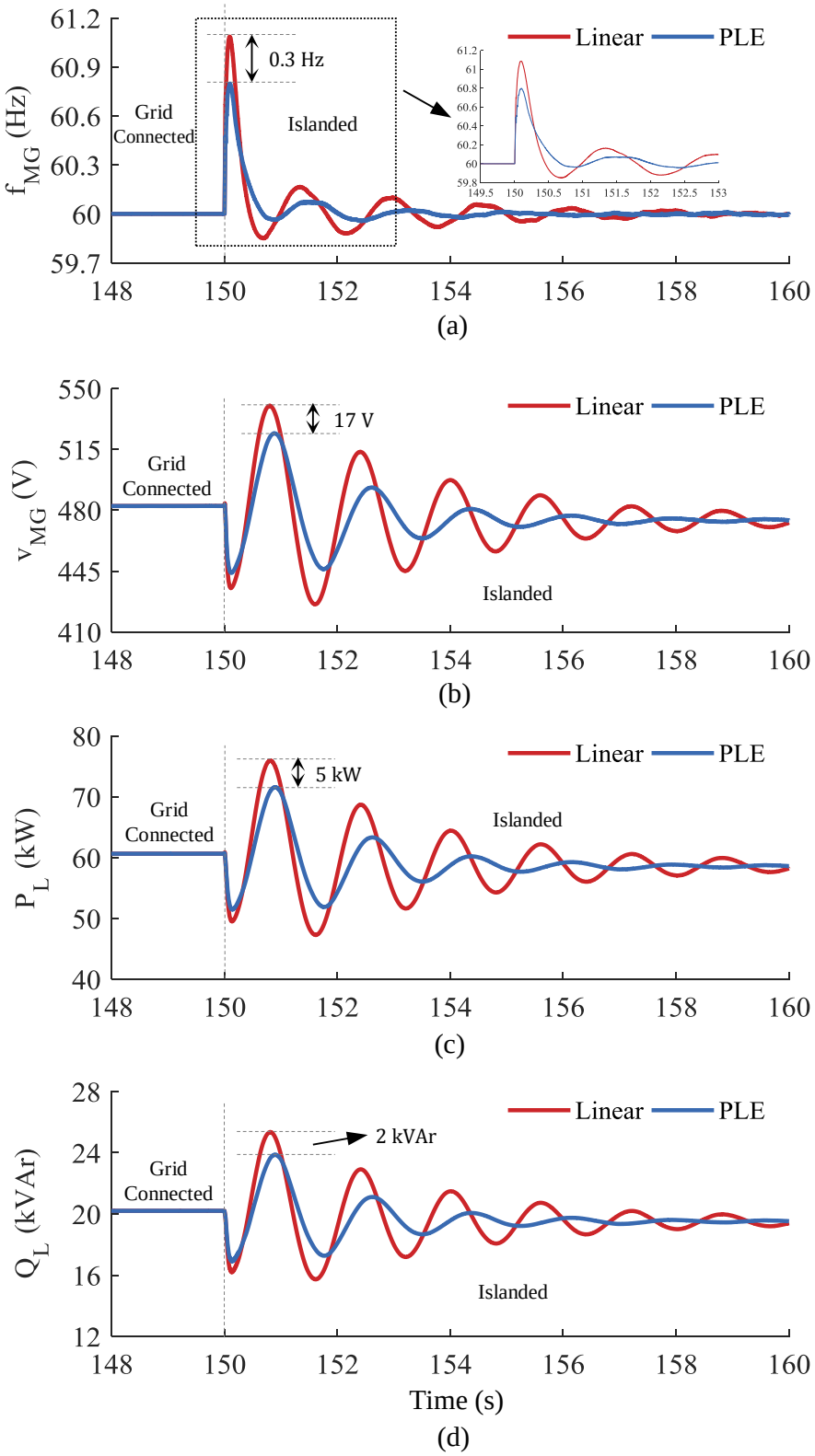

Figure 3.18: Case study 4: comparison between linear and PLE droops in dynamic-performance improvement of the system during transition from grid-connected to islanded mode. (a) AC-bus frequency. (b) AC-bus voltage. (c) Load active power. (d) Load reactive power.

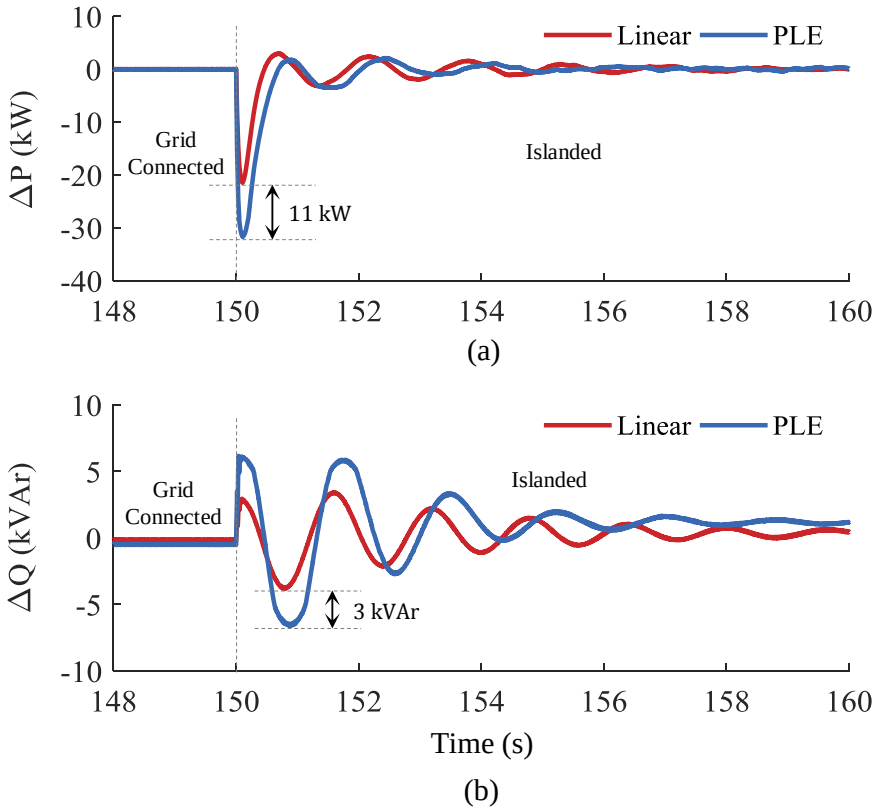

Figure 3.19: Case study 4: comparison between the injected/absorbed (a) active and (b) reactive power by BESS during transition from grid-connected to islanded mode.

reactive power. It can be observed that more active and reactive power are injected/absorbed by BESS when the PLE droops are employed, leading to a significant reduction in voltage and frequency variations. Table 3.3 investigates the effect of utilizing the proposed PLE droops in dynamic-performance improvement of microgrid based on the results demonstrated in Fig. 3.18. The provided comparison analysis in Table 3.3 indicates that the proposed PLE droops are an effective solution for dealing with the stability challenges and improving the dynamic behavior of islanded microgrids during transition from grid-connected to islanded mode of operation.

3.3.1.5 Case Study 5: Change in the Length of Narrow Linear Regions

This case study investigates the effect of change in the length of narrow linear regions on the dynamic behavior of the system. As shown in Figs. 3.4 and 3.7, the proposed

Table 3.3: Case Study 4: Dynamic Performance Comparision of Microgrid with Linear and PLE Droops During Transition from Grid-connected to Islanded Mode

	With Linear		**With PLE**	
	Settling Time	Overshoot	Settling Time	Overshoot
f_{MG}	7 s	1.1 Hz	3 s	0.8 Hz
v_{MG}	9 s	70 V	5 s	53 V
P_{L}	8 s	15 kW	4 s	10 kW
Q_{L}	9 s	6 kVAr	4 s	4 kVAr

PLE droops include narrow linear regions around the nominal voltage and frequency. The presence of narrow linear regions prevents the abrupt changes in the active and reactive power injected/absorbed by BESS for small variations of voltage and frequency. As the result, a smoother operation by BESS during the abnormal conditions can be achieved. Figs. 3.20 and 3.21 illustrate the effect of change in droop coefficients of narrow linear regions, i.e., m_{P2} and m_{Q2}, on the mitigation of frequency and voltage variations, respectively, when there is a step change in load demand. An increase in m_{P2} and m_{Q2} results in an increase in the length of narrow linear regions. In other words, increasing m_{P2} and m_{Q2} adds more linearity to the PLE droops which results in injection/absorption of less amount active and reactive power during abnormal conditions. Thus, in order to achieve an enhanced dynamic behavior, smaller values of m_{P2} and m_{Q2} are preferable. However, due to the sudden changes in the active and reactive power of BESS for very small values of m_{P2} and m_{Q2} (or extremely narrowed linear regions), the minimum allowable values of m_{P2} and m_{Q2}, i.e., $m_{P2\_\min}$ and $m_{Q2\_\min}$, are required. Figs. 3.20 and 3.21 illustrate $m_{P2\_\min}$ and $m_{Q2\_\min}$ at which there is a trade-off between linearity of PLE droops and dynamic-response enhancement of the system.

3.3.2 APD Characteristic

This subsection investigates the merits of proposed approach in suppressing the short-term voltage and frequency variations using PV units. For this purpose, the detailed model of islanded mixed-inertia microgrid shown in Fig. 3.10 (including two paralleled PV units) is developed in PSCAD/EMTDC environment, with the parameters listed in Table 3.4.

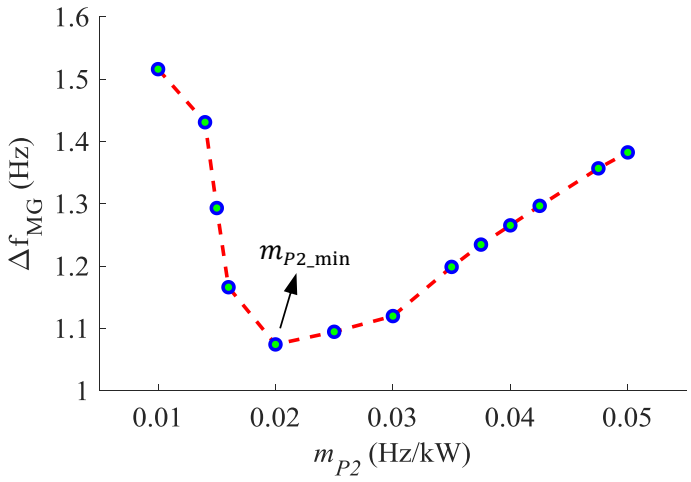

Figure 3.20: Case study 5: effect of change in m_{P2} (or length of narrow linear region) on the frequency variations of ac bus when $m_P = 0.05$ Hz/kW.

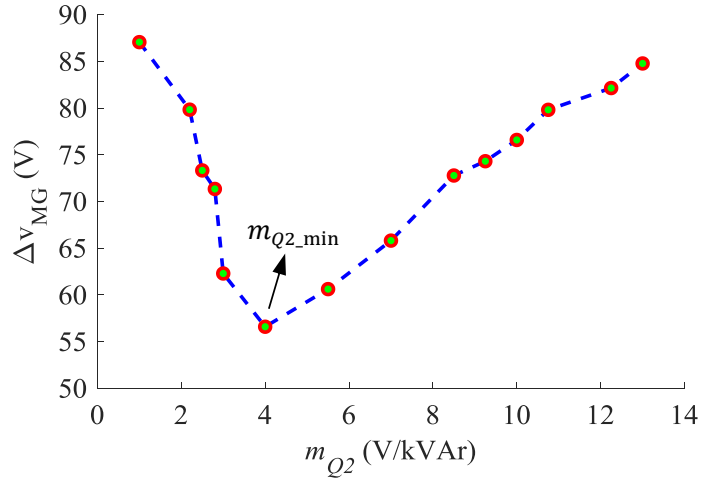

Figure 3.21: Case study 5: effect of change in m_{Q2} (or length of narrow linear region) on the voltage variations of ac bus when $m_Q = 13$ V/kVAr.

3.3.2.1 Case Study 6: Grid-Feeding vs. Grid-Supporting PV Units for Load Step Change

This case study presents a comparison between the conventional grid-feeding PV units and the suggested grid-supporting PV units equipped with proposed droops in dynamic-performance improvement of the system when the load demand is stepped up. The PV unit 1 operates in MPPT mode, while PV unit 2 works in power-reference mode ($P^*_{\text{PV2\_SS}} = 10$ kW and $Q^*_{\text{PV2\_SS}} = 0$ kVAr). The active and reactive power demand, i.e., P_{D} and Q_{D}, are initially

Table 3.4: System Parameters for Islanded Microgrid shown in Fig. 3.10

	Parameter	Value
DGs	Battery Operating Voltage Range	360-600 V
	Battery Rated Energy	101 kWh
	PVs Maximum Power	50 kW
	Diesel Generator Maximum Power	127 kW
	Diesel Generator Inertia Constant (H)	0.3 s
Droop Characteristics	f^*_{MG}	60 Hz
	$f_{\text{MG\_min}}$	58 Hz
	$f_{\text{MG\_max}}$	62 Hz
	v^*_{MG} (line $-$ to $-$ line)	480 V
	$v_{\text{MG\_min}}$ (line $-$ to $-$ line)	400 V
	$v_{\text{MG\_max}}$ (line $-$ to $-$ line)	560 V
	m_Q	13 V/kVAr
	$Q^*_{\text{PV\_SS}}$	0 kVAr
	v^*_{dc}	1000 V

60 kW and 20 kVAr. At instant $t = 30$ s, the active and reactive power demand step up to 120 kW and 40 kVAr.

Figs. 3.22(a) and 3.22(b) show the injected active power by PV unit 1 and 2, respectively. As can be seen in Fig. 3.22(a), stepping up the load demand does not affect the provided active power by PV unit 1, and this is due to its operation in MPPT mode. However, as illustrated in Fig. 3.22(b), implementing the APD results in injecting more active power by PV unit 2 to compensate the instantaneous active-power imbalance between generation and consumption. In other words, by setting the active-power setpoint of PV unit 2, i.e., $P^*_{\text{PV2\_SS}}$, below its MPP, the reserve power is released during abnormal conditions. On the other hand, implementing the linear Q-v droops in PV systems results in injecting/absorbing reactive power during abnormalities which can help to achieve an enhance voltage profile, see Figs. 3.22(c) and 3.22(d).

The effectiveness of proposed droops in dynamic-response enhancement of the system is investigated in Fig. 3.23. As can be seen in Fig. 3.23(a), a faster frequency restoration is achieved, while the frequency nadir is improved by about 0.25 Hz. Moreover, the fluctuations of load active power, i.e., P_{L}, are analyzed in Fig. 3.23(c), with and without the

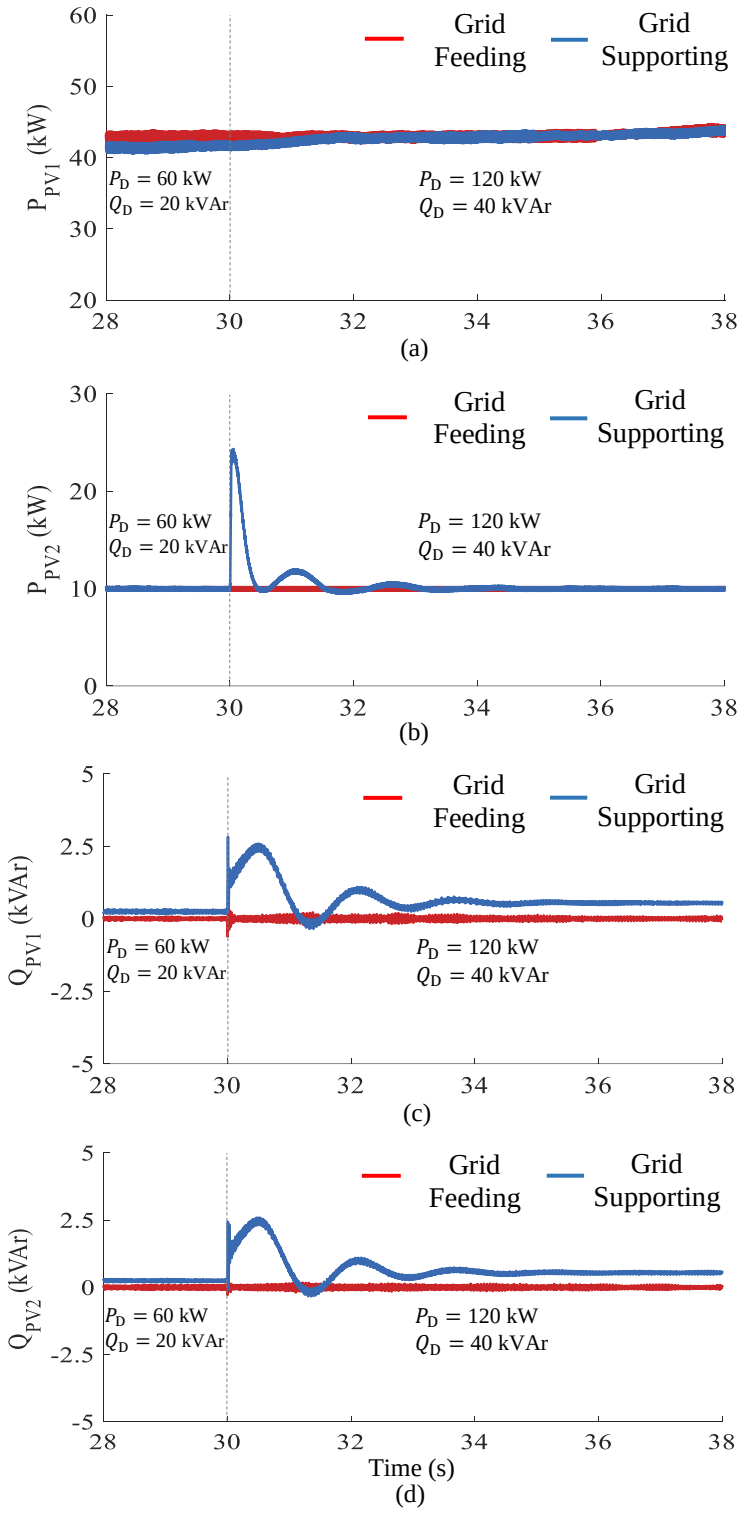

Figure 3.22: Case study 6: evaluating the performance of PV units operating in grid-feeding and grid-supporting modes when there is a load step change. (a) Active power of PV unit 1. (b) Active power of PV unit 2. (c) Reactive power of PV unit 1. (d) Reactive power of PV unit 2.

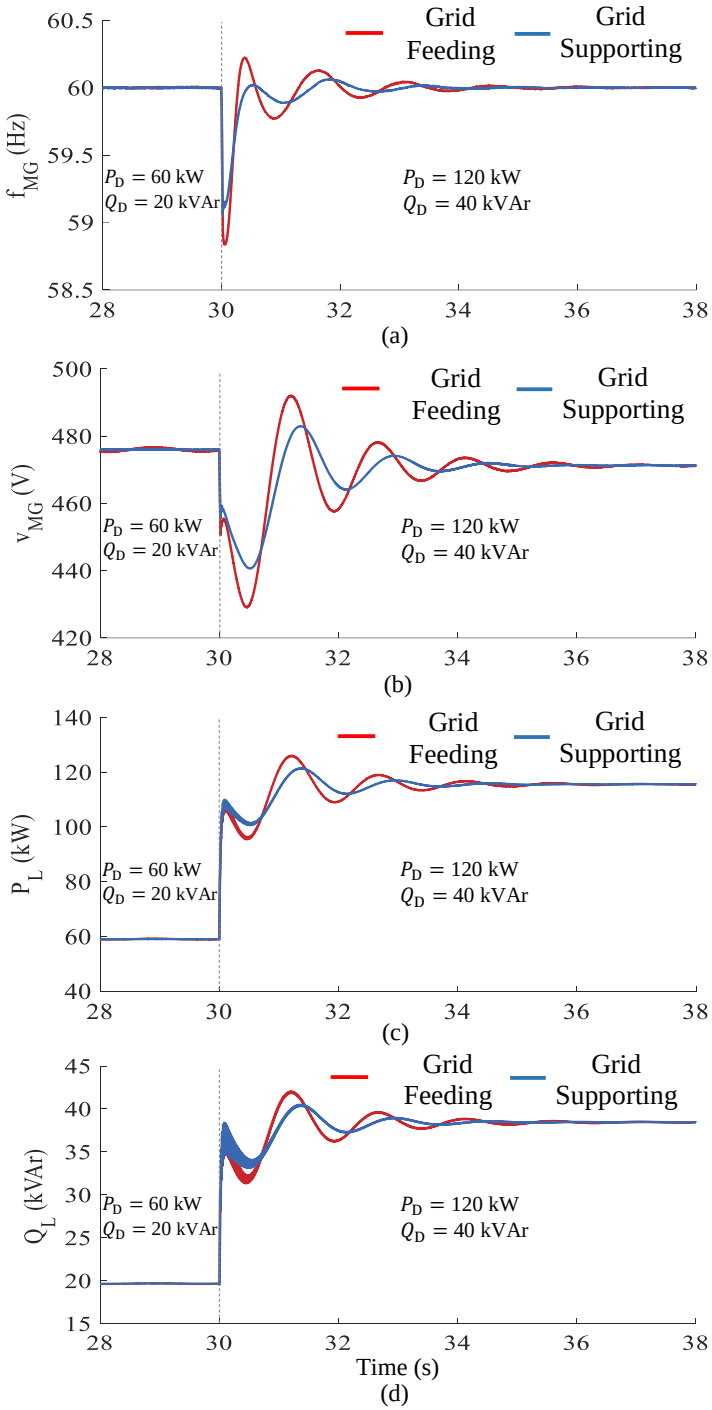

Figure 3.23: Case study 6: evaluating the performance of PV units operating in grid-feeding and grid-supporting modes when there is a load step change. (a) AC-bus frequency. (b) AC-bus voltage. (c) Load active power. (d) Load reactive power.

proposed APD. It can be observed that equipping PV units with the proposed APD leads to a considerable mitigation in fluctuations of P_{L} during abnormalities. Similarly, as shown in

Figs. 3.23(b) and 3.23(d), employing the proposed linear Q-v droop leads to a considerable mitigation in fluctuations of ac-bus voltage and load reactive power, i.e., v_{MG} and Q_{L}, during abnormal conditions.

3.4 Conclusion

In this chapter, the cooperative role of BESS and PV units in improving the dynamic behavior of islanded mixed-inertia microgrids during abnormalities has been studied. For this purpose, two PLE droops, i.e., P-f and Q-v, have been proposed for BESS to mitigate the voltage and frequency variations during abnormal conditions such as sudden load changes and transition from grid-connected to islanded mode. It has been demonstrated that instead of any linear droop with a specified droop coefficient, a PLE droop can be defined using the presented approach in this chapter. Compared with linear droops, significant mitigation in voltage and frequency fluctuations has been achieved, when the BESS is equipped with the proposed PLE droops. Besides, an APD has been proposed for PV units to mitigate the frequency variations during abnormal conditions. A significant mitigation in frequency fluctuations has been achieved, when the PV units are equipped with the proposed APD. In addition, a Q-v droop has been implemented in PV units to cope with voltage oscillations during abnormal conditions. Utilizing the proposed droops turns the conventional inverters employed in BESS and PV units into smart inverters capable of coping with abnormalities. Different case studies have been carried out to validate the effectiveness and superiority of the proposed droop control approaches in dynamic-performance improvement of islanded microgrids.

Chapter 4

Improved Dynamics in Single-Phase/Residential Microgrids

This chapter proposes an approach to form a unified single-phase microgrid from three isolated single-phase feeders at distribution level. To this end, a seamless transition algorithm is presented which monitors the system condition in real time, and coordinates the operation of all inverter-based DG units in residential microgrid accordingly during transitions. Any abnormal condition on the grid side results in isolating the residential microgrid from utility grid, and giving the full responsibility of supplying household loads to local DG units. However, in such condition, some phases might face the challenge of meeting local load demand due to the lack of enough power generation, resulting in voltage drop and frequency variation across household loads. In order to resolve this issue, the proposed method in this chapter seamlessly interconnects all three single-phase feeders during islanded mode and forms a unified single-phase residential microgrid. Consequently, the load demands in all three phases are met, leading to enhanced voltage and frequency profiles. On the other hand, the proposed approach is capable of deforming the single-phase formed residential microgrid to a residential community with three separate phases, and subsequently, synchronize each phase voltage with its respective grid-side voltage in order to seamlessly reconnect to the main grid. Several case studies are carried out in PSCAD/EMTDC environment to verify

the validity of proposed method.

This chapter includes five sections. Section 4.1 describes the overall configuration of residential community equipped with proposed seamless transition algorithm. The control scheme of single-phase inverters without implementation of proposed approach is presented in Section 4.2. The proposed seamless transition technique along with the modified controller of single-phase inverters are provided in Section 4.3. The validity of proposed approach is confirmed in Section 4.4 via different case studies, while Section 4.5 concludes this chapter.

4.1 Residential Microgrid Equipped with Proposed Seamless Transition Algorithm

The schematic of residential microgrid capable of seamlessly transfer between different operation modes is shown in Fig. 4.1. The residential community is derived through a step-down transformer to meet the voltage level for residential customers. The residential microgrid includes a group of houses which are equipped with different DG units. Each DG unit consists of an energy source, e.g. rooftop PV panel, connected to its respective phase through PEIs. Table 4.1 summarizes different operation modes of residential microgrid. During grid-connected mode, both voltage and frequency of the system are regulated by the main grid. In such condition, DG units typically operate in PQ (or grid following) control mode to cooperate in supplying their respective household loads. However, when the system is islanded, it is necessary to make DG units responsible for maintaining the voltage and frequency of the system by transferring their operation mode from PQ control to vf (or grid forming) control. As can be seen in Fig. 4.1, the incorporated DG units and loads are different for each residence. Moreover, there might be some houses which still have not incorporated any DG unit. Thus, each residence has different amounts of local generation and consumption, and consequently, some phases might suffer from power imbalance between supply and demand when the residential community is disconnected from utility grid, i.e., islanded mode.

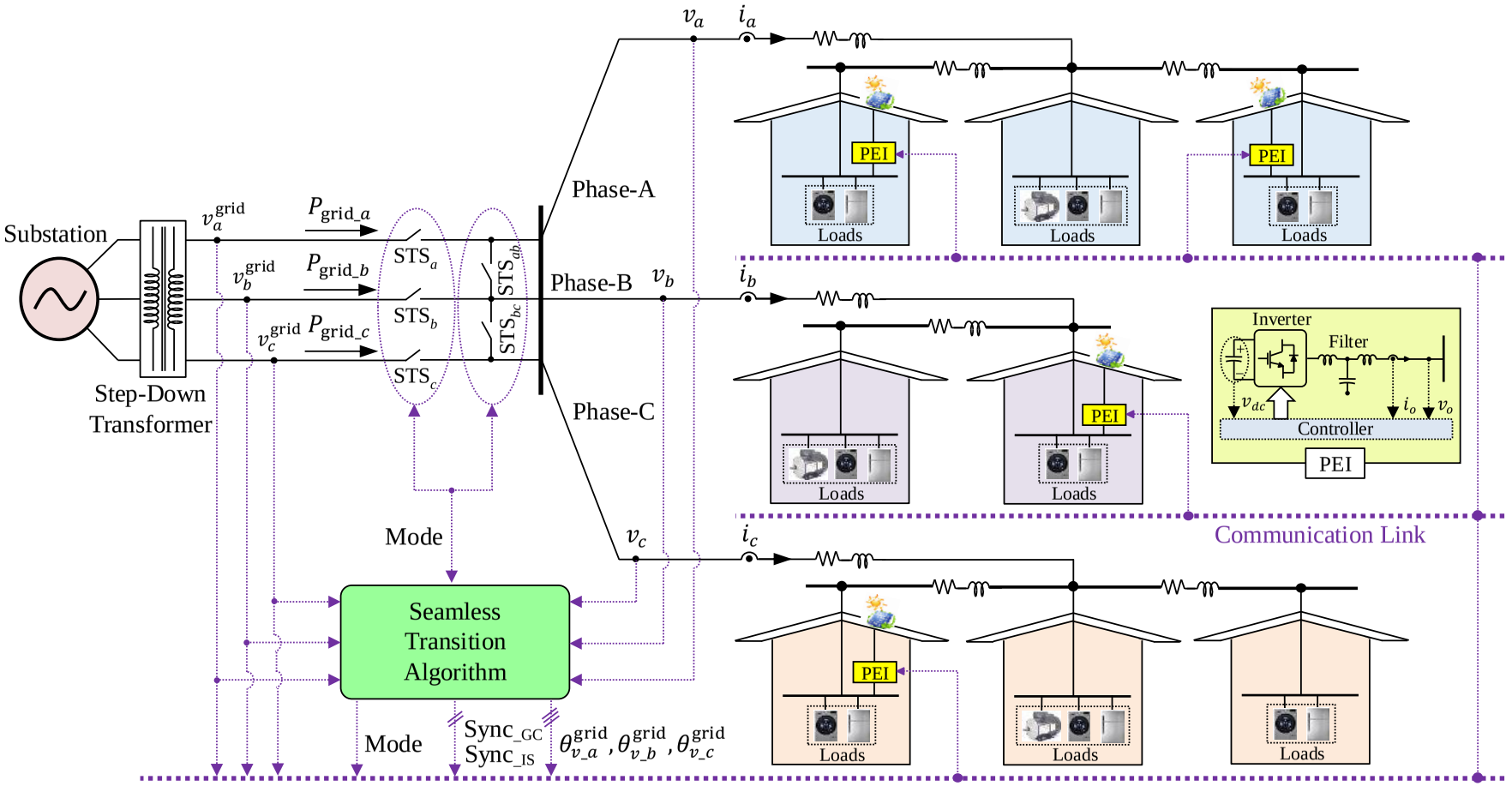

Figure 4.1: Schematic of residential microgrid equipped with proposed seamless transition algorithm.

Table 4.1: Different Operation Modes of Residential Microgrid

Grid STSs ($\mathbf{STS_a}$, $\mathbf{STS_b}$, $\mathbf{STS_c}$)	**Inter − Phase STSs** ($\mathbf{STS_{ab}}$, $\mathbf{STS_{bc}}$)	**Mode**
Off	Off	Islanded (00)
Off	On	Inter−Phase Connected (01)
On	Off	Grid Connected (10)

The residential community shown in Fig. 4.1 is connected to the main grid via STSs, i.e., STS_a, STS_b, and STS_c, enabling residential community to get isloated from the grid in case of abnormal conditions. As previously mentioned, the unavailability of utility grid in an islanded residential microgrid can lead to power imbalance inside the phases. Thus, in order to cope with potential power imbalances during islanded operation, two STSs, i.e., STS_{ab} and STS_{bc}, are employed in the architecture to interconnect the three phases, i.e., inter-phase connected mode. Considering the fact that each phase is regulated at its respective voltage and frequency during islanded mode, a mechanism is implemented in controllers of single-phase inverters in order to synchronize all three phases before closing the aforementioned inter-phase STSs and transferring to inter-phase connected mode. In addition, the controllers of single-phase inverters are modified to prepare the residential microgrid for a seamless reconnection to the main grid. The seamless transition algorithm is responsible to send appropriate commands to the STSs once its predefined criteria are satisfied.

4.2 Principles of Controller Design for Single-Phase Inverters

This section explains the control scheme of each single-phase inverter during grid-connected and islanded modes without incorporation of proposed seamless transition approach. The outer-loop controllers are different for grid-connected and islanded modes, while the inner-loop current controller of each single-phase inverter is formulated using the dq reference frame transformation [89, 102] for both grid-connected and islanded modes. The d-axis and

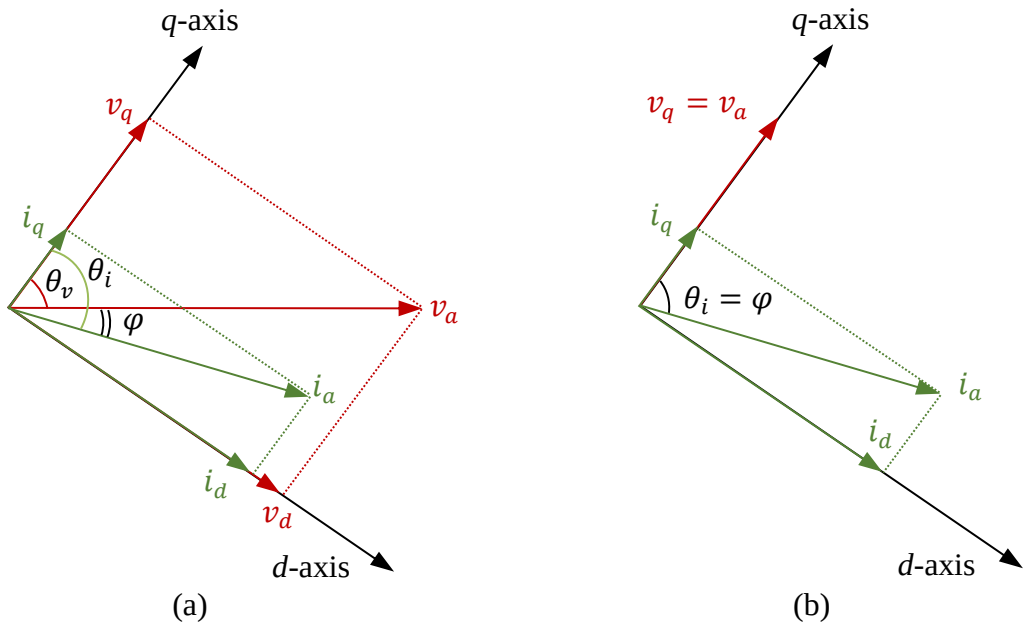

Figure 4.2: The phase current and voltage in (a) an arbitrary d-axis and q-axis, and (b) the q-axis locked to the voltage.

q-axis components of voltages and currents can be calculated using the phasor diagrams shown in Fig. 4.2. Assuming that $d\theta_v/dt = \omega$ is the angular frequency of the system, i.e., q-axis is locked to the phase voltage, the dq components of phase voltage and current can be obtained as follows:

$$v_q = v_m \tag{4.1}$$

$$v_d = 0 \tag{4.2}$$

$$i_q = i_m \cos\varphi \tag{4.3}$$

$$i_d = i_m \sin\varphi \tag{4.4}$$

where v_m and i_m are the amplitudes of phase voltage and current, respectively, and φ is the

phase shift between phase voltage and current.

Using (4.1), (4.2), (4.3), and (4.4), the active and reactive power in single-phase system can be calculated as follows:

$$P = \frac{1}{2} v_m i_m \cos\varphi = \frac{1}{2} v_q i_q \tag{4.5}$$

$$Q = \frac{1}{2} v_m i_m \sin\varphi = \frac{1}{2} v_q i_d \tag{4.6}$$

The residential microgrid consists of multiple inverter-based DG units which need to be equipped with a control scheme that enables them to operate during both grid-connected and islanded modes. Fig. 4.3 shows the control scheme of an individual single-phase inverter which selects proper values to be controlled depending on the operation mode of the system.

4.2.1 Grid-Connected Mode

Due to the tight regulation of voltage and frequency by utility grid during grid-connected mode, the signal command "Mode" is set to "1" to force the inverter to operate in PQ control mode, see Fig. 4.3. In such condition, the desired active power, i.e., P^*, can be provided by a supervising EMS [105], while the desired reactive power, i.e., Q^*, is typically set to zero to achieve a unity power factor. Using (4.5) and (4.6), the reference values for dq components of inverter output current, i.e., $i^*_{d\_\mathrm{GC}}$ and $i^*_{q\_\mathrm{GC}}$, are determined and fed into the inner-loop current controller to obtain the desired values for PWM of the inverter, i.e., $v^*_{\mathrm{inv}\_d}$ and $v^*_{\mathrm{inv}\_q}$. Besides, the angles of inverter output voltage and current, i.e., θ_{v_GC} and θ_{i_GC}, are extracted using PLLs.

4.2.2 Islanded Mode

When the residential microgrid is islanded from utility grid, i.e., Mode = 0, both voltage and frequency of the system need to be maintained by the inverter-based DG units, see Fig. 4.3. For this purpose and due to the predominance of resistive lines over inductive lines

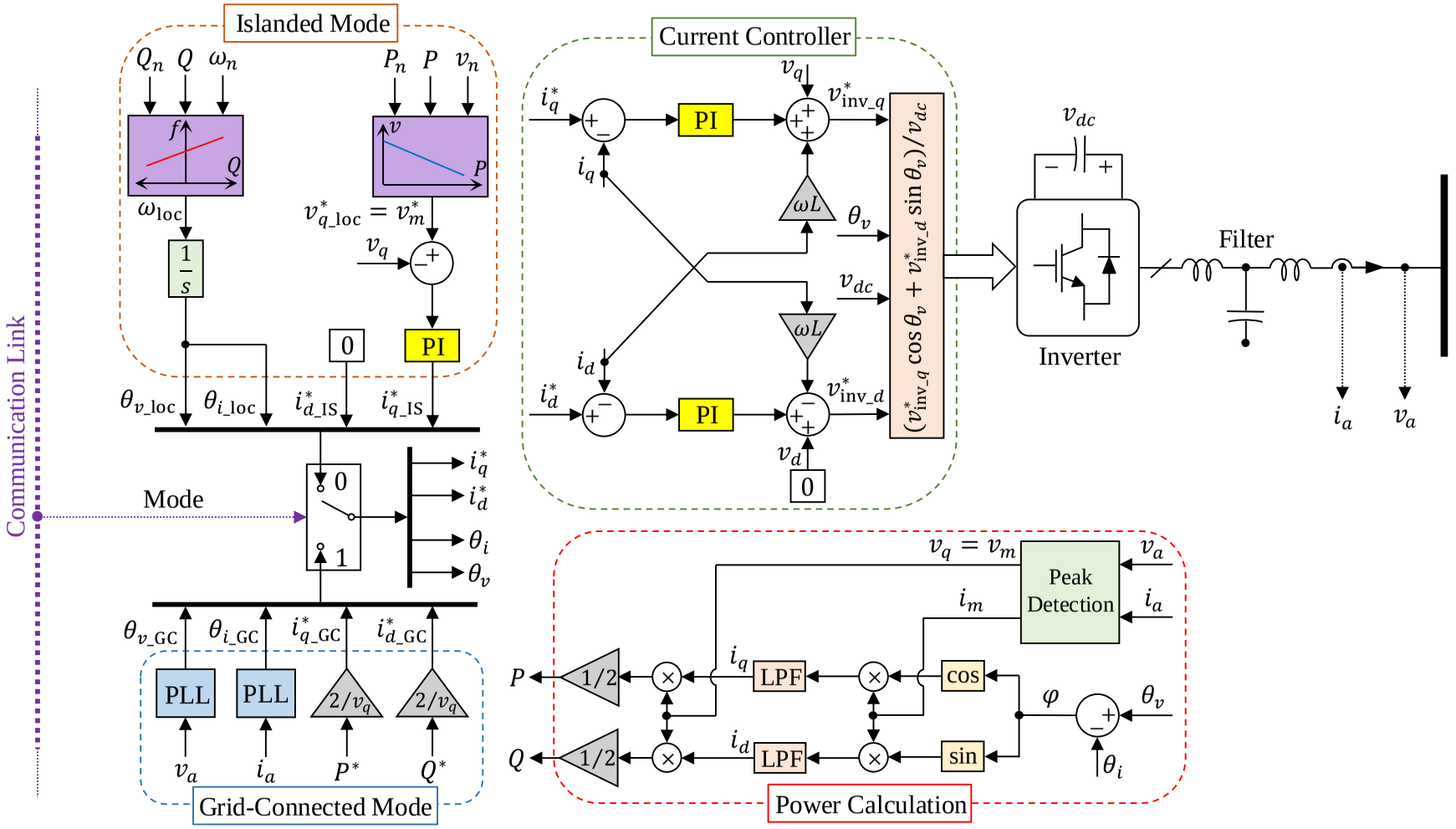

Figure 4.3: Control scheme of an individual single-phase inverter (in Phase-A) capable of operating in both grid-connected and islanded modes without implementation of proposed seamless transition approach [103, 104].

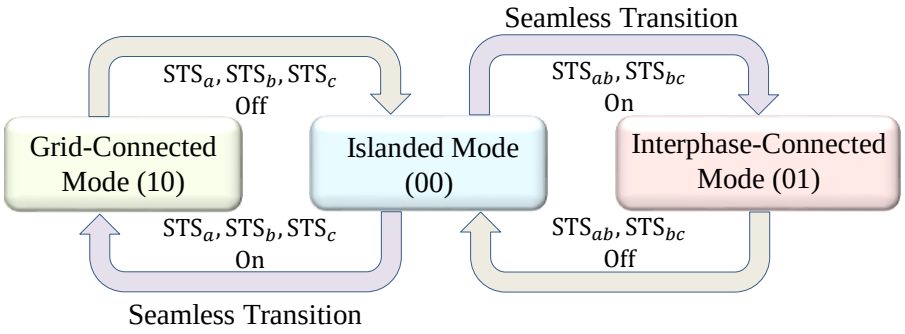

Figure 4.4: Mode-transition approach.

in residential communities, two inverse/reverse droop characteristics, i.e., P-v and Q-f, are implemented in the control scheme of single-phase inverters to achieve the desired voltage amplitude and angular frequency as follows:

$$v^*_{q\_\mathrm{loc}} = v^*_m = \sqrt{2}(v_n - m_P(P - P_n)) \tag{4.7}$$

$$\omega_{\mathrm{loc}} = \omega_n + m_Q(Q - Q_n) \tag{4.8}$$

where P and Q are the active and reactive power output of the inverter, respectively, obtained by (4.5) and (4.6). v_n and ω_n are the nominal values of inverter output voltage and its angular frequency, respectively, while P_n and Q_n are, respectively, the dispatched active and reactive power at v_n and ω_n. Also, m_P and m_Q are the droop coefficients of P-v and Q-f characteristics, respectively. As illustrated in Fig. 4.3, the reference value for q-axis component of inverter output current, i.e., $i^*_{q\_\mathrm{IS}}$, is obtained by passing the subtraction of $v^*_{q\_\mathrm{loc}}$ and v_q through a proportional-integral (PI) controller, while the reference value for d-axis component of inverter output voltage is set to zero. Besides, the angles of inverter output voltage and current, i.e., θ_{v_loc} and θ_{i_loc}, are generated locally by integrating ω_{loc}.

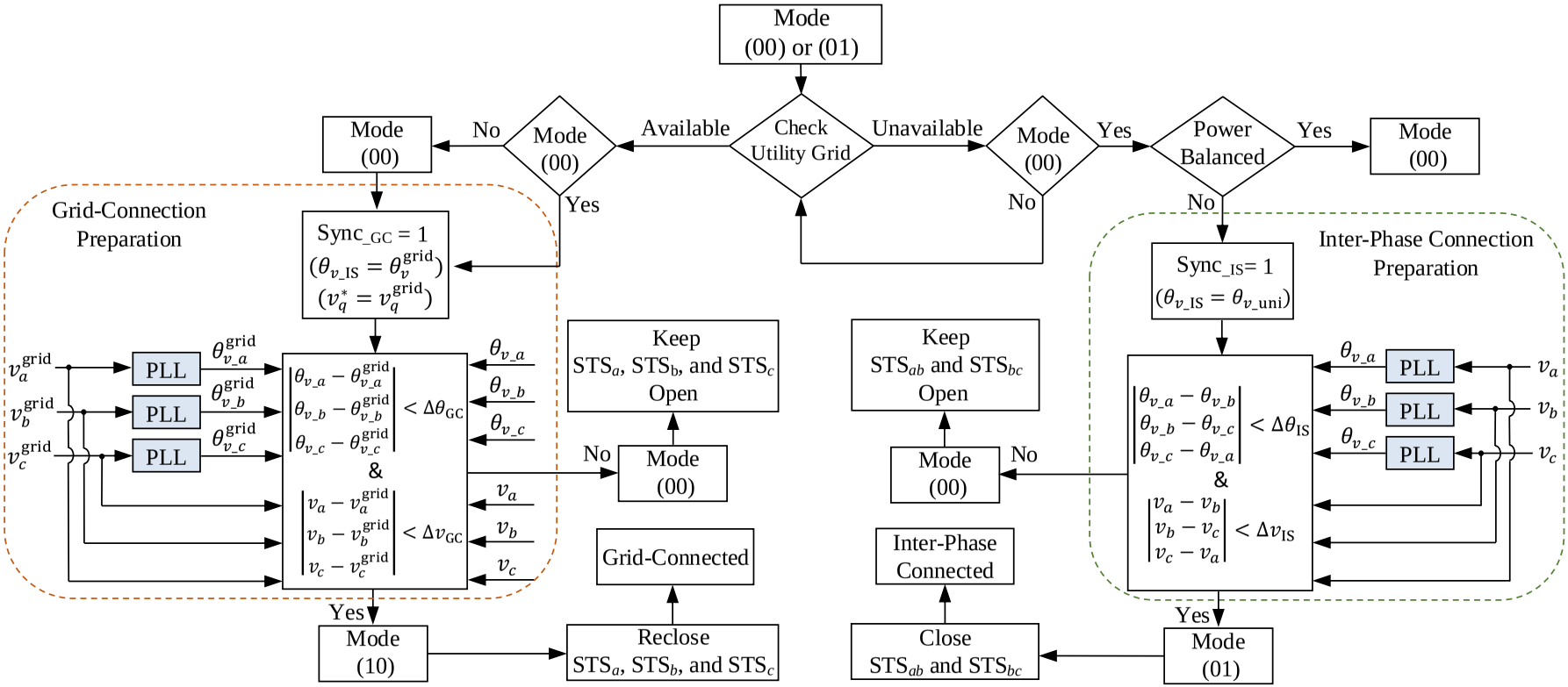

Figure 4.5: The proposed algorithm for seamless transitions between different operation modes, i.e., islanded mode (00), inter-phase connected mode (01), and grid-connected mode (10).

4.3 Seamless Transitions Between Different Operation Modes

This section discusses the necessity of achieving a residential microgrid which can seamlessly transfer between different operation modes, and proposes a seamless transition algorithm along with an improved control scheme for single-phase inverters to attain this.

4.3.1 Seamless Transition Algorithm

A general overview of mode-transition approach is presented in Fig. 4.4. Besides, the proposed technique to achieve seamless transitions while transferring between different operation modes is shown in Fig. 4.5. This seamless transition algorithm has two main objectives. First, seamless interconnection of all three single-phase feeders and forming a unified single-phase residential microgrid, i.e., inter-phase connected mode, when the system is islanded and there is a power imbalance in at least one of the phases. Second, deforming the single-phase formed residential microgrid to a residential community in which the angle difference between the phases is 120 degrees, and preparing it to reconnect to the main grid seamlessly, i.e., grid-connected mode.

The unavailability of enough power generation units in either of the phases during islanded mode can lead to power imbalance, resulting in voltage and frequency variations over household loads. This situation is not desirable, especially for the critical loads in the system [48]. In such condition, as illustrated in Fig. 4.5, the signal command "Sync_IS" is set to "1" to be sent to the controllers of all DG units. As the result, the locally generated voltage angle of each DG unit, i.e., θ_{v_loc}, is replaced by a unified voltage angle, i.e., θ_{v_uni}, which is a periodical ramp signal varying from 0 to 2π with the frequency of 60 Hz. θ_{v_uni} is fed to the controllers and once the difference between voltage magnitudes of all three phases is below $\triangle v_{\mathrm{IS}}$ and their angle subtraction is less than $\triangle\theta_{\mathrm{IS}}$, the signal "Mode" changes from "00" to "01" to close the inter-phase STSs, i.e., STS_{ab} and STS_{bc} in Fig. 4.1, and form a single-phase residential microgrid.

After resolving the abnormal condition on the grid side, the residential microgrid can reconnect to the main grid, i.e., grid-connected mode. For this purpose, as shown in Fig. 4.5, first, the signal "Mode" is set to "00", i.e., islanded mode, to open the inter-phase STSs, in case they have been closed due to the power imbalance in the system. Then, the signal "Sync_GC" is set to "1" and transferred to the controllers of all inverters through communication links. Changing "Sync_GC" from "0" to "1" allows the DG units in each phase to take the amplitude and angle of their respective grid-side voltage, i.e., v_a^{grid}, v_b^{grid}, and v_c^{grid}, as the reference for their controllers. As can be seen in Fig. 4.5, the signal command "Mode" is set to "10" right after synchronization of grid voltages with phase voltages of residential microgrid. This results in reclosing the grid STSs and switching to grid-connected mode seamlessly.

4.3.2 Seamless Transition to Inter-Phase Connected Mode and Forming a Single-Phase Residential Microgrid

Any abnormal condition on the grid side can result in isolating the residential microgrid from utility grid. In such condition, the signal "Mode" is changed from "10" to "00" and transferred through communication links to all inverters in order to enable them to operate in *vf* control mode instead of *PQ* control mode, see Figs. 4.1 and 4.3. During islanded mode, there might be one phase or even more facing the challenge of meeting the local load demand due to the lack of enough power generation units. In such condition, a potential solution to ensure power balance within all three phases is inter-phase connection. However, due to the local control of voltage and frequency during islanded mode, the amplitude and/or angle of voltage for each phase might be different at the time of inter-phase connection, leading to considerable transients across the loads. Therefore, it is necessary to modify the controllers of DG units to achieve a seamless transition while interconnecting all three phases and forming a single-phase residential microgrid. For this purpose and before closing the inter-phase STSs, i.e., STS_{ab} and STS_{bc} in Fig. 4.1, the voltages of all three phases must be synchronized with each other. To this end, as illustrated by the modified control

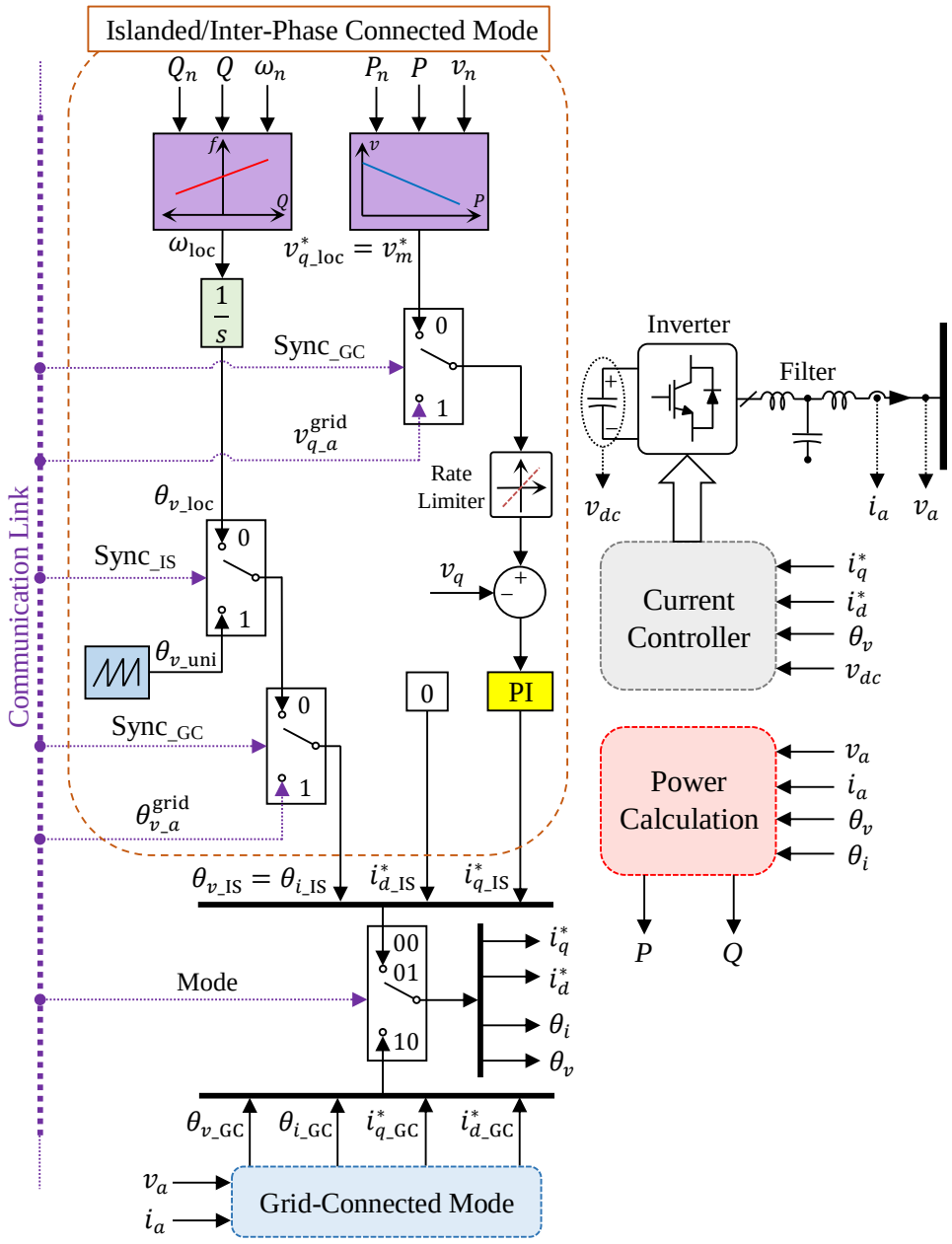

Figure 4.6: Modified control scheme of an individual single-phase inverter (in Phase-A) capable of operating in grid-connected, islanded, and inter-phase connected modes with implementation of proposed seamless transition approach.

scheme of an individual single-phase inverter in Fig. 4.6, the unified voltage angle of θ_{v_uni} with the frequency of 60 Hz is fed to the controllers of all inverters by switching the signal command "Sync$_{_\text{IS}}$" from "0" to "1". Once the voltages of all three single-phase feeders are synchronized, and their magnitude and angle subtractions are less than prespecified values, i.e., $\triangle v_{\text{IS}}$ and $\Delta\theta_{\text{IS}}$, the seamless transition algorithm allows the inter-phase connection by

closing STS_{ab} and STS_{bc}.

4.3.3 Seamless Transition to Grid-Connected Mode

In order to avoid severe transients introduced by closing the grid STSs, the phase voltages of residential microgrid, i.e., v_a, v_b, and v_c in Fig. 4.1, should be synchronized with their respective grid-side voltages, i.e., v_a^{grid}, v_b^{grid}, and v_c^{grid} in Fig. 4.1, before reconnecting the residential community to the main grid. However, due to the lack of enough power generation units in some phases during islanded mode, there might be some cases in which the whole residential community is formed as a single-phase microgrid by closing the inter-phase STSs, i.e., inter-phase connected mode. In such condition and before closing the grid STSs, the residential microgrid should transfer to islanded mode and turn into a residential community in which the angle difference between the phases is 120 degrees. For this purpose, the signal command "Sync_{GC}" is switched from "0" to "1" right after opening the inter-phase STSs, and transferred to the controllers of all DG units through communication links. As can be found from Fig. 4.6, this results in feeding the angles of grid voltages, i.e., $\theta_{v\_a}^{\text{grid}}$, $\theta_{v\_b}^{\text{grid}}$, and $\theta_{v\_c}^{\text{grid}}$, to the controllers and taking the q-axis components of grid-side voltages, i.e., $v_{q\_a}^{\text{grid}}$, $v_{q\_b}^{\text{grid}}$, and $v_{q\_c}^{\text{grid}}$, as the reference for v_q. Once each phase voltage is synchronized with its respective grid voltage, the seamless transition algorithm allows the residential microgrid to reconnect to the main grid by changing the signal "Mode" from "00" to "10" and reclosing the grid STSs.

4.4 Verification

This section investigates the viability of proposed method in semaless forming of a single-phase microgrid from three isolated single-phase feeders, and also, seamless reconnection of residential microgrid to utility grid after resolving the abnormal conditions on the grid side. For this purpose, the detailed model of a residential microgrid, with the parameters listed in Table 4.2, is developed in PSCAD/EMTDC environment. Phase-A of the developed res-

Table 4.2: System Parameters

Parameter	Symbol	Value
Nominal Voltage (Line to Neutral)	v_n	240 V
Nominal Angular Frequency	ω_n	377 rad/s
P-v Droop Coefficient of 1st DG in Phase-A	$m_{P\text{DG1}-a}$	0.0006 kV/kW
Q-f Droop Coefficient of 1st DG in Phase-A	$m_{Q\text{DG1}-a}$	0.009 Hz/kVAr
P-v Droop Coefficient of 2nd DG in Phase-A	$m_{P\text{DG2}-a}$	0.0003 kV/kW
Q-f Droop Coefficient of 2nd DG in Phase-A	$m_{Q\text{DG2}-a}$	0.0048 Hz/kVAr
P-v Droop Coefficient of 1st DG in Phase-B	$m_{P\text{DG1}-b}$	0.0003 kV/kW
Q-f Droop Coefficient of 1st DG in Phase-B	$m_{Q\text{DG1}-b}$	0.0048 Hz/kVAr
P-v Droop Coefficient of 1st DG in Phase-C	$m_{P\text{DG1}-c}$	0.0003 kV/kW
Q-f Droop Coefficient of 1st DG in Phase-C	$m_{Q\text{DG1}-c}$	0.0048 Hz/kVAr

idential community consists of two DG units, i.e., DG1-a and DG2-a, while Phase-B and Phase-C each include one DG unit, i.e., DG1-b and DG1-c. A delay of 4 ms is considered for the STSs. The equivalent load resistances in Phase-A, Phase-B, and Phase-C are, respectively, 3.84 Ω, 2.304 Ω, and 1.152 Ω, while the equivalent load inductances in Phase-A, Phase-B, and Phase-C are 30.6 mH, 15.3 mH, and 10.2 mH, respectively. Consequently, considering the nominal voltage of 240 V for single-phase feeders, the total load demands in Phase-A, Phase-B, and Phase-C are 15kW+j5kVAr, 25kW+j10kVAr, and 50kW+j15kVAr, respectively.

4.4.1 Case Study 1: Residential Microgrid Performance Under Power Imbalance Condition in Phase-C

The first case study investigates the operation of residential microgrid during grid-connected and islanded modes, while the generated power in Phase-C is not enough to supply the load during islanded operation. The residential microgrid is initially in grid-connected mode, i.e., Mode (10), and at $t = 20$ s, it gets disconnected from utility grid, i.e., Mode (00).

The active and reactive power flows of Phase-C are shown in Figs. 4.7(a) and 4.7(b), respectively. It can be observed that during grid-connected mode, DG1-c generates the exact amount of active and reactive power dictated by its desired values, i.e., 20 kW and 0 kVAr.

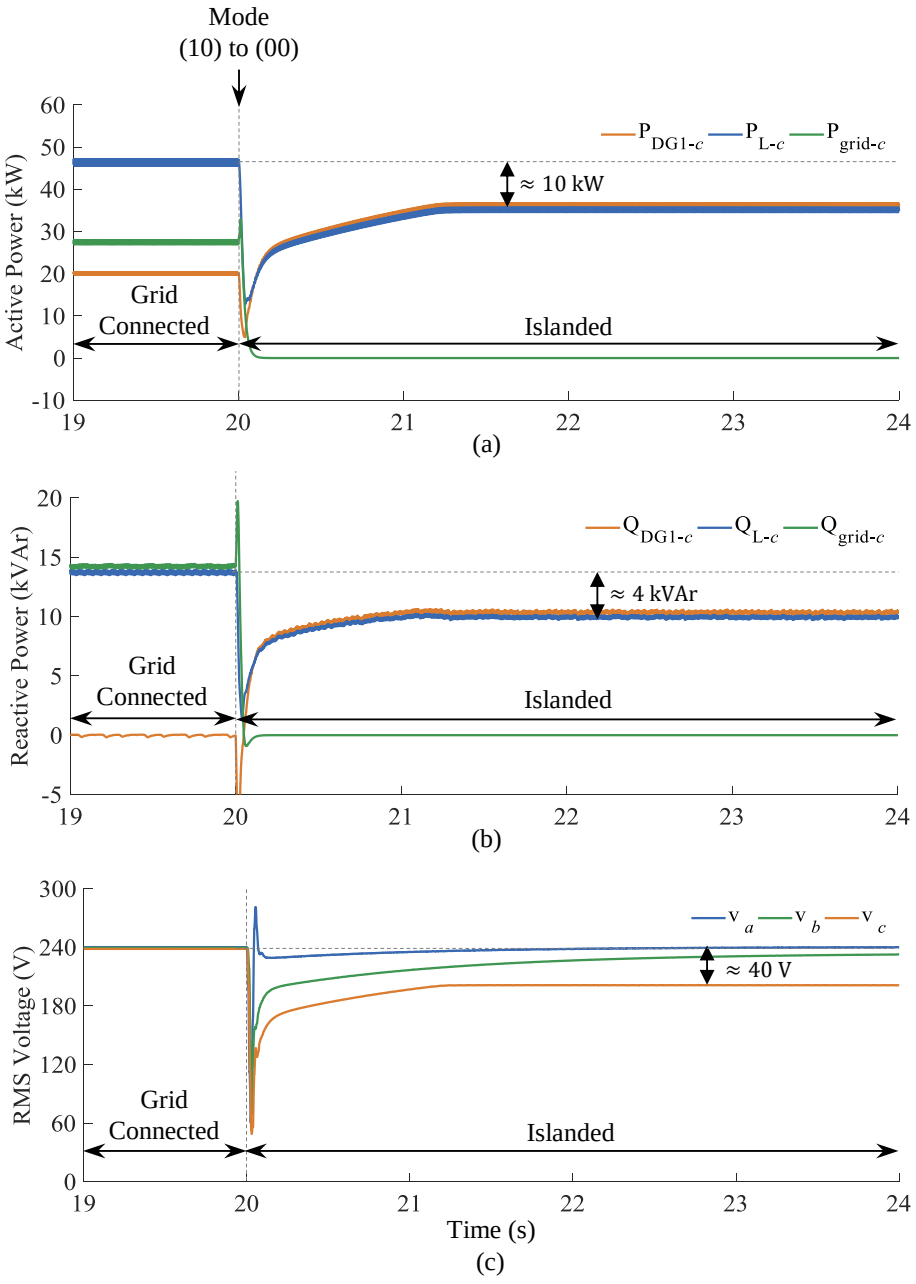

Figure 4.7: Case study 1: residential microgrid performance under power imbalance condition in Phase-C during islanded mode. (a) Active power flow in Phase-C. (b) Reactive power flow in Phase-C. (c) Phase voltages.

In such condition, the utility grid injects/absorbs the deficit/extra active and reactive power. After transferring to islanded mode, DG1-c starts operating in vf control mode and takes the responsibility of supplying local loads in Phase-C. However, as can be seen in Figs. 4.7(a) and 4.7(b), there is a power imbalance between the load demand and power generation in Phase-

C during islanded mode. In other words, although the active and reactive power demand in Phase-C are 50 kW and 15 kVAr, respectively, DG1-c is only capable of generating about 37 kW and 10 kVAr. As the result, the household loads in Phase-C suffer from a voltage drop of 40 V from their nominal value during islanded mode, whereas the required voltage level is perfectly met in the other two phases, see Fig. 4.7(c). A potential solution to solve this issue is to interconnect all three single-phase feeders during islanded operation and form a unified single-phase residential microgrid, i.e., inter-phase connected mode.

4.4.2 Case Study 2: Seamless Transition to Inter-Phase Connected Mode and Forming a Single-Phase Residential Microgrid

This case study evaluates the performance of the system during transition to inter-phase connected mode with and without the proposed seamless transition approach, see Figs. 4.8 and 4.9. As shown in Fig. 4.8, at $t = 20$ s, the residential microgrid transfers from grid-connected to islanded mode by switching the signal command "Mode" from "10" to "00". After 2 s, i.e., at $t = 22$ s, the operator observes power imbalance and voltage drop in Phase-C, and thus, interconnects all three single-phase feeders by changing the signal "Mode" from "00" to "01". As illustrated in Figs. 4.8(a) and 4.8(b), despite providing the required active and reactive power of the loads after inter-phase connection, huge transients in generated active and reactive power of DG units can be observed. This is due to the lack of synchronization between the phase voltages, which leads to considerable overcurrents inside the phases, see Figs. 4.8(c) and 4.8(d).

Fig. 4.9 demonstrates the effectiveness of proposed technique for seamless interconnection of all three single-phase feeders and forming a unified single-phase residential microgrid. After transferring to islanded mode at $t = 20$ s, the seamless transition algorithm shown in Fig. 4.5 identifies the power imbalance in Phase-C at $t = 22$ s, and subsequently, changes the signal "Sync$_{_\text{IS}}$" from "0" to "1". As the result, the locally generated voltage angle of each DG unit, i.e., θ_{v_loc}, is replaced by a unified voltage angle, i.e., θ_{v_uni}, with the frequency of 60 Hz. The predefined criteria of seamless transition algorithm are satisfied after 0.09 s, i.e., at t

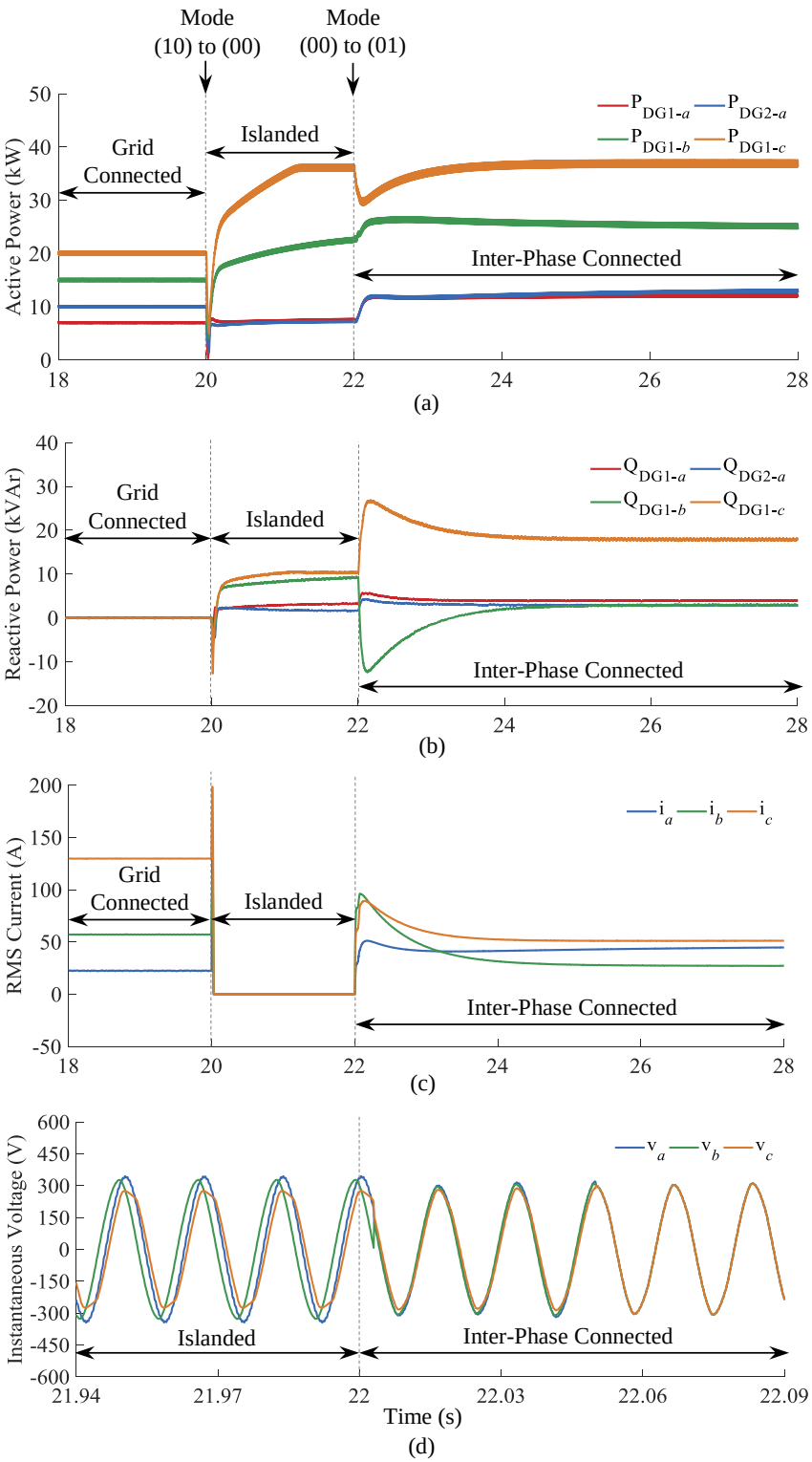

Figure 4.8: Case study 2: transferring to inter-phase connected mode and forming a single-phase residential microgrid without implementation of proposed seamless transition approach. (a) Active power of DG units. (b) Reactive power of DG units. (c) Phase currents. (d) Phase voltages.

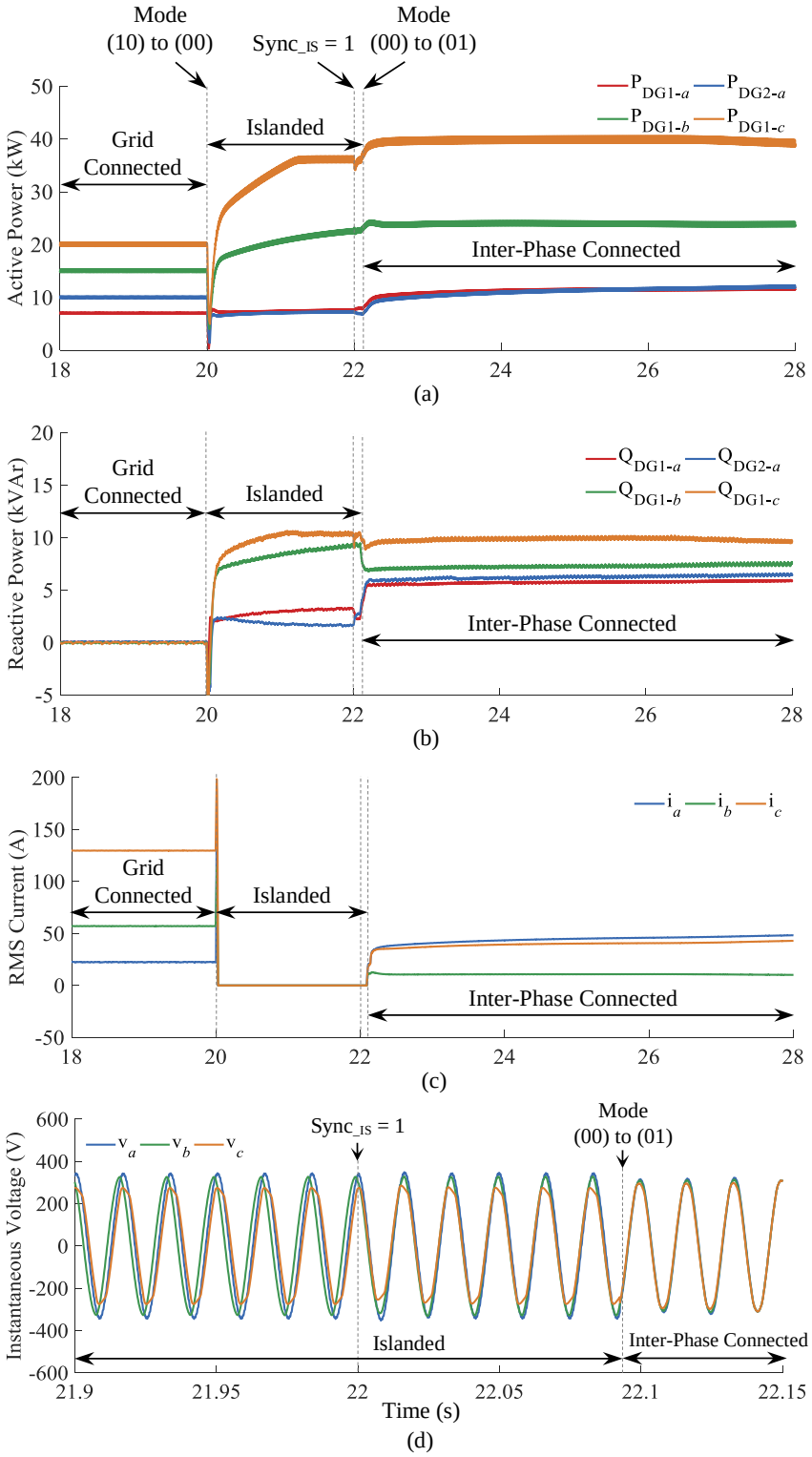

Figure 4.9: Case study 2: transferring to inter-phase connected mode and forming a single-phase residential microgrid with implementation of proposed seamless transition approach. (a) Active power of DG units. (b) Reactive power of DG units. (c) Phase currents. (d) Phase voltages.

= 22.09 s, resulting in closing the inter-phase STSs by changing signal "Mode" from "00" to "01". Compared to Figs. 4.8(a) and 4.8(b), a significant mitigation in transients of generated active and reactive power by DG units can be seen in Figs. 4.9(a) and 4.9(b), while the loads in all three phases are supplied sufficiently. This dynamic-performance improvement is due to the voltage synchronization of all three single-phase feeders before closing the inter-phase STSs, resulting in suppression of overcurrents inside the phases, see Figs. 4.9(c) and 4.9(d).

4.4.3 Case Study 3: Seamless Transition to Grid-Connected Mode

This case study evaluates the performance of the system during transition to grid-connected mode with and without the proposed seamless transition method, see Figs. 4.10 and 4.11. As shown in Fig. 4.10, while the system is still in inter-phase connected mode and at $t = 40$ s, the operator disconnects all three single-phase feeders from each other, i.e., Mode (00), and at $t = 42.5$ s, reconnects the residential microgrid to the main grid, i.e., Mode (10). Consequently, as illustrated in Figs. 4.10(a) and 4.10(b), the DG units in Phase-A and Phase-C, i.e., DG1-a, DG2-a, and DG1-c, become unstable right after reconnecting to the utility grid. On the other hand, although the DG unit in Phase-B, i.e., DG1-b, follows its desired active and reactive power values during grid-connected mode, i.e., 15 kW and 0 kVAr, it is still suffering from huge transients after reclosing the grid STSs. This is due to the lack of synchronization between the phase voltages, i.e., v_a, v_b, and v_c, and grid-side voltages, i.e., v_a^{grid}, v_b^{grid}, and v_c^{grid}, resulting in highly distorted power and current transferred to the main grid, see Figs. 4.10(c)-4.10(f).

The viability of proposed approach in seamless reconnecting the residential microgrid to the main grid is demonstrated in Fig. 4.11. Based on the introduced seamless transition algorithm shown in Fig. 4.5, after the availability of grid and at $t = 40$ s, the signal "Mode" is set to "00" to disconnect the phases from each other. Subsequently, the signal "Sync$_{\text{_GC}}$" is changed from "0" to "1" in order to synchronize the phase voltages with grid voltages. The predefined criteria for the difference between magnitudes and angles of phase voltages and grid voltages are satisfied at $t = 42.5$ s, leading to grid-connected mode by switching

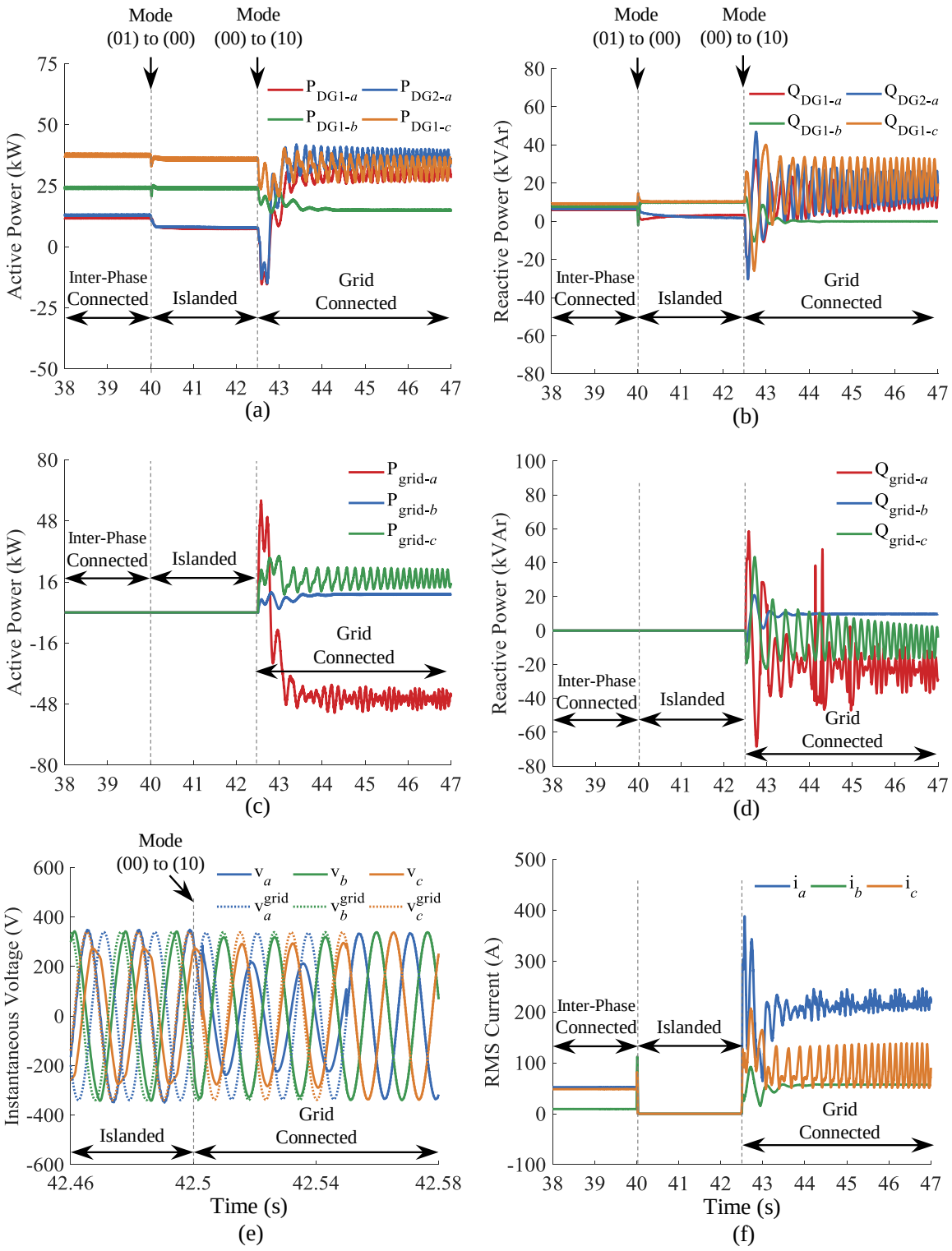

Figure 4.10: Case study 3: transferring to grid-connected mode without implementation of proposed seamless transition approach. (a) Active power of DG units. (b) Reactive power of DG units. (c) Active power of grid. (d) Reactive power of grid. (e) Phase voltages. (f) Phase currents.

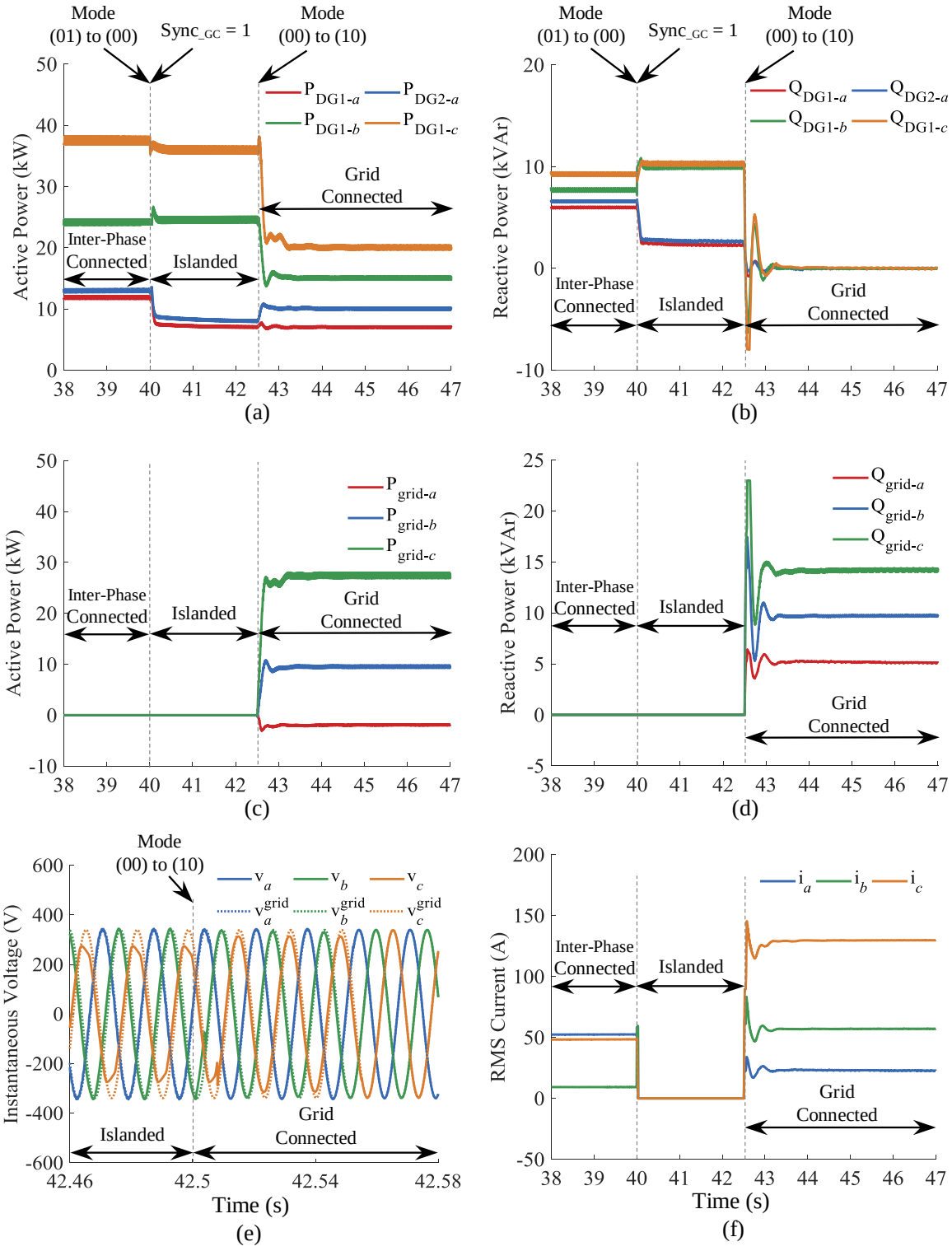

Figure 4.11: Case study 3: transferring to grid-connected mode with implementation of proposed seamless transition approach. (a) Active power of DG units. (b) Reactive power of DG units. (c) Active power of grid. (d) Reactive power of grid. (e) Phase voltages. (f) Phase currents.

the signal command "Mode" from "00" to "10". As illustrated in Figs. 4.11(a)-4.11(d), the DG units start generating their desired active and reactive power right after transferring to grid-connected mode, while the quality of power delivered to/from utility grid is significantly improved. This is because of synchronizing the phase voltages with their respective grid-side voltages before reconnecting to the main grid, see Fig. 4.11(e). A comparison between Figs. 4.10(f) and 4.11(f) leads to the fact that implementing the proposed seamless transition approach results in injecting much less distorted currents to the grid, while overcurrents are significantly mitigated.

4.5 Conclusion

In this chapter, a seamless transition approach has been presented for residential communities which are suffering from power imbalance inside the phases during islanded mode. To this end, the proposed method has enabled seamless interconnection of all three phases of residential community during islanded mode. This has led to supplying the local loads in all three phases at their desired voltage level. This new operation mode is called inter-phase connected mode. On the other hand, after resolving the abnormal condition on the grid side, the residential microgrid has been reconnected to the utility grid seamlessly. Employing the proposed approach has ensured the stable operation of DG units during transitions, while the power quality has improved significantly. A seamless transition algorithm has been introduced which monitors the system condition in real time and sends appropriate signal commands to the STSs in order to ensure seamless transitions. Different case studies have been carried out to validate the effectiveness and superiority of proposed method in achieving seamless transitions in residential microgrids.

Chapter 5

Conclusions and Suggestions for Future Work

The main contributions and accomplishments of this dissertation are highlighted in this chapter, followed by suggestions for possible future research topics. Section 5.1 summarizes the main contributions of dissertation. Besides, suggestions for possible future works are provided in Section 5.2.

5.1 Summary and Conclusions

In this dissertation, different techniques have been proposed to improve the dynamic behavior of microgrids during abnormal consditions such as sudden load changes, loss of generation, and transitions between different operation modes. In the introductory chapter, the role of microgrids as an inportant part of energy infrastructure along with the necessity of improving their dynamic response has been discussed. Besides, a review of the existing state-of-the-art solutions to address the aforementioned challenges and a summary of the main contributions of dissertation are provided as an introduction.

A new configuration and control scheme for smart loads has been presented in this dissertation to cope with abnormal conditions in a fleet of nanogrids. A significant improvement

in the dynamics of nanogrids has been achieved when incorporating the proposed smart loads. The small-signal state-space model of smart loads has been developed considering the switching process of three-phase inverter. This model has been used for eigenvalue analysis of smart loads to investigate their stability region and robustness. The effect of employing smart loads on the stability of overall system could be studied by incorporating the derived model into the models of nanogrids. Furthermore, it has been indicated that the proposed smart load configuration can be an effective solution to increase the lifetime and reduce the size of the central battery bank. Different case studies have been carried out to confirm the merits of the proposed smart loads in small-scale microgrids known as nanogrids.

Furthermore, the conventional control schemes of BESS and PV units have been modified in this dissertation to investigate their cooperative role in dynamic-response enhancement of islanded microgrids. To this end, two PLE droops, i.e., P-f and Q-v, have been proposed for BESS to suppress the voltage and frequency fluctuations during abnormalities. Using the proposed approach, any linear droop characteristic with a specified droop coefficient can be replaced by a PLE droop. It has been demonstarted that equipping BESS with the proposed PLE droops leads to a considerable reduction in voltage and frequency variations in comparison with linear droops. Moreover, the cooperative role of PV units in improving the dynamic behavior of islanded microgrids has been investigated by deploying their conventional control schemes. For this purpose, an APD curve has been presented for PV units to reduce the frequency fluctuations during abnormal conditions. A significant suppression in frequency variations has been achieved, when the the proposed APD has been implemented in the controller of PV units. In addition, a Q-v droop has been employed in PV units to deal with voltage deviations during abnormal conditions. The merits of proposed approaches in improving the dynamics of islanded microgrids has been verified by case study results.

Moreover, a method has been proposed in this dissertation to seamlessly interconnect three islolated single-phase feeders at distribution level and form a unified residential commulity in case of power imbalance in at least one of the feeders. This has led to maintaining the voltage of household loads at their desired level in all three phases. In addition, after resolving the abnormal condition on the grid side, the residential community has been recon-

nected to the main grid seamlessly. The stable operation of DG units during transitions has been ensured by implementing the proposed method, and the power quality has been improved significantly. A seamless transition algorithm has been proposed which monitors the system condition in real time and sends appropriate signal commands to the STSs in order to guarantee the seamless transitions. Various case studies have been carried out to confirm the effectiveness and superiority of proposed approach in achieving seamless transitions in residential microgrids.

In conclusion, this dissertation has been focused on dynamic-response enhancement of microgrids during abnormalities, and to attain this, different approaches have been proposed to be employed in a fleet of nanogrids, islanded microgrids, and single-phase residential microgrids. The validity of proposed methods has been verified using PSCAD/EMTDC.

5.2 Suggestions for Future Work

The work presented in this dissertation has advanced the state-of-the-art in impoving the dynamic behavior of microgrids during abnormal conditions. While the viability of proposed approches has been validated by employing numerous case studies, there are some opportunities to further build upon the work presented herein.

The proposed control scheme of smart loads in Chapter 2 can be modified for further improvement of voltage profiles across the critical loads. Therefore, one potential avenue of future research could be to design a self-tune current controller for smart loads by online estimation of critical load impedance and overcome the short-term transients caused by load variations. On the other hand, the developed small-signal state-space model of smart loads could be incorporated into the models of nanogrids in order to achieve a general state-space model for GNG equipped with the proposed smart loads.

The presented PLE droops in Chapter 3 follow an elliptic trajectory for further mitigation of voltage and frequency fluctuations in islanded microgrids. Nevertheless, the nonlinear droops are not limited to the elliptic path, and thus, proposing different nonlinear trajectories can be the topic of a future work. Besides, the conventional P-f and Q-v characteristics could

be replaced by the inverse/reverse droops, i.e., P-v and Q-f, to further analyze and compare their performance.

The proposed approach in Chapter 4 achieves seamless transitions between different operation modes in residential microgrids by utilizing a centralized seamless transition algorithm and sending appropriate signal commands to single-phase inverters through communication links. However, a more comprehensive advance in the research can be achieved by reducing the communication requirements of the system. One solution to attain this could be incorporation of online estimation techniques to estimate the voltage angles of feeders and the grid locally.

Bibliography

[1] M. Ban, M. Shahidehpour, J. Yu, and Z. Li, "A cyber-physical energy management system and optimal sizing of networked nanogrids with battery swapping stations," *IEEE Trans. Sustain. Energy*, vol. 10, no. 1, pp. 491–502, 2017.

[2] M. R. Sandgani and S. Sirouspour, "Energy management in a network of grid-connected microgrids/nanogrids using compromise programming," *IEEE Trans. Smart Grid*, vol. 9, no. 3, pp. 2180–2191, 2016.

[3] A. Werth, N. Kitamura, and K. Tanaka, "Conceptual study for open energy systems: distributed energy network using interconnected DC nanogrids," *IEEE Trans. Smart Grid*, vol. 6, no. 4, pp. 1621–1630, 2015.

[4] T. Morstyn, B. Hredzak, and V. G. Agelidis, "Control strategies for microgrids with distributed energy storage systems: An overview," *IEEE Trans. Smart Grid*, vol. 9, no. 4, pp. 3652–3666, 2016.

[5] M. B. Shadmand, R. S. Balog, and M. D. Johnson, "Predicting variability of high-penetration photovoltaic systems in a community microgrid by analyzing high-temporal rate data," *IEEE Trans. Sustain. Energy*, vol. 5, no. 4, pp. 1434–1442, 2014.

[6] R. Tonkoski, D. Turcotte, and T. H. El-Fouly, "Impact of high PV penetration on voltage profiles in residential neighborhoods," *IEEE Trans. Sustain. Energy*, vol. 3, no. 3, pp. 518–527, 2012.

[7] Y. Riffonneau, S. Bacha, F. Barruel, and S. Ploix, "Optimal power flow management for grid connected PV systems with batteries," *IEEE Trans. Sustain. Energy*, vol. 2, no. 3, pp. 309–320, 2011.

[8] S. Eftekharnejad, V. Vittal, G. T. Heydt, B. Keel, and J. Loehr, "Impact of increased penetration of photovoltaic generation on power systems," *IEEE Trans. Power Syst.*, vol. 28, no. 2, pp. 893–901, 2013.

[9] P. Palensky and D. Dietrich, "Demand side management: Demand response, intelligent energy systems, and smart loads," *IEEE Trans. Ind. Informat.*, vol. 7, no. 3, pp. 381–388, 2011.

[10] D. Westermann and A. John, "Demand matching wind power generation with wide-area measurement and demand-side management," *IEEE Trans. Energy Convers.*, vol. 22, no. 1, pp. 145–149, 2007.

[11] J. Sachs and O. Sawodny, "A two-stage model predictive control strategy for economic diesel-PV-battery island microgrid operation in rural areas," *IEEE Trans. Sustain. Energy*, vol. 7, no. 3, pp. 903–913, 2016.

[12] B. Singh, G. Pathak, and B. K. Panigrahi, "Seamless transfer of renewable-based microgrid between utility grid and diesel generator," *IEEE Trans. Power Electron.*, vol. 33, no. 10, pp. 8427–8437, 2018.

[13] Y.-Y. Hong and R.-C. Lian, "Optimal sizing of hybrid wind/PV/diesel generation in a stand-alone power system using markov-based genetic algorithm," *IEEE Trans. Power Del.*, vol. 27, no. 2, pp. 640–647, 2012.

[14] A. Aderibole, H. H. Zeineldin, M. S. El-Moursi, J. C.-H. Peng, and M. Al Hosani, "Domain of stability characterization for hybrid microgrids considering different power sharing conditions," *IEEE Trans. Energy Convers.*, vol. 33, no. 1, pp. 312–323, 2018.

[15] R. Engleitner, A. Nied, M. S. M. Cavalca, and J. P. da Costa, "Dynamic analysis of small wind turbines frequency support capability in a low-power wind-diesel microgrid," *IEEE Trans. Ind. Appl.*, vol. 54, no. 1, pp. 102–111, 2018.

[16] Q. Fu, L. F. Montoya, A. Solanki, A. Nasiri, V. Bhavaraju, T. Abdallah, and C. Y. David, "Microgrid generation capacity design with renewables and energy storage addressing power quality and surety," *IEEE Trans. Smart Grid*, vol. 3, no. 4, pp. 2019–2027, 2012.

[17] O. Dag and B. Mirafzal, "On stability of islanded low-inertia microgrids," in *2016 Clemson University Power Systems Conference (PSC)*, 2016, pp. 1–7.

[18] Z. Miao, A. Domijan, and L. Fan, "Investigation of microgrids with both inverter interfaced and direct ac-connected distributed energy resources," *IEEE Trans. Power Del.*, vol. 26, no. 3, pp. 1634–1642, 2011.

[19] H. Mahmood, D. Michaelson, and J. Jiang, "Strategies for independent deployment and autonomous control of PV and battery units in islanded microgrids," *IEEE J. Emerg. Sel. Topics Power Electron.*, vol. 3, no. 3, pp. 742–755, 2015.

[20] A. Adib, B. Mirafzal, X. Wang, and F. Blaabjerg, "On stability of voltage source inverters in weak grids," *IEEE Access*, vol. 6, pp. 4427–4439, 2018.

[21] A. Singh and B. Mirafzal, "An efficient grid-connected three-phase single-stage boost current source inverter," *IEEE Power and Energy Technology Systems Journal*, vol. 6, no. 3, pp. 142–151, 2019.

[22] J. Lamb, B. Mirafzal, and F. Blaabjerg, "PWM common mode reference generation for maximizing the linear modulation region of CHB converters in islanded microgrids," *IEEE Trans. Ind. Electron.*, vol. 65, no. 7, pp. 5250–5259, 2018.

[23] K. Tan, P. So, Y. Chu, and M. Chen, "Coordinated control and energy management of distributed generation inverters in a microgrid," *IEEE Trans. Power Del.*, vol. 28, no. 2, pp. 704–713, 2013.

[24] D. Photovoltaics and E. Storage, "IEEE standard for interconnection and interoperability of distributed energy resources with associated electric power systems interfaces," *IEEE Std*, pp. 1547–2018, 2018.

[25] G. G. Talapur, H. M. Suryawanshi, L. Xu, and A. B. Shitole, "A reliable microgrid with seamless transition between grid connected and islanded mode for residential community with enhanced power quality," *IEEE Trans. Ind. Appl.*, vol. 54, no. 5, pp. 5246–5255, 2018.

[26] S. A. Raza and J. Jiang, "Intra-and inter-phase power management and control of a residential microgrid at the distribution level," *IEEE Trans. Smart Grid*, vol. 10, no. 6, pp. 6839–6848, 2019.

[27] A. Adib and B. Mirafzal, "Virtual inductance for stable operation of grid-interactive voltage source inverters," *IEEE Trans. Ind. Electron.*, vol. 66, no. 8, pp. 6002–6011, 2018.

[28] S. George and V. Agarwal, "A DSP-based control algorithm for series active filter for optimized compensation under nonsinusoidal and unbalanced voltage conditions," *IEEE Trans. Power Del.*, vol. 22, no. 1, pp. 302–310, 2007.

[29] S.-R. Rafiei, H. A. Toliyat, R. Ghazi, and T. Gopalarathnam, "An optimal and flexible control strategy for active filtering and power factor correction under non-sinusoidal line voltages," *IEEE Trans. Power Del.*, vol. 16, no. 2, pp. 297–305, 2001.

[30] C. Hochgraf and R. H. Lasseter, "STATCOM controls for operation with unbalanced voltages," *IEEE Trans. Power Del.*, vol. 13, no. 2, pp. 538–544, 1998.

[31] L. Gyugyi, C. D. Schauder, and K. K. Sen, "Static synchronous series compensator: a solid-state approach to the series compensation of transmission lines," *IEEE Trans. Power Del.*, vol. 12, no. 1, pp. 406–417, 1997.

[32] L. F. Costa, G. De Carne, G. Buticchi, and M. Liserre, "The smart transformer: A solid-state transformer tailored to provide ancillary services to the distribution grid," *IEEE Power Electron. Mag.*, vol. 4, no. 2, pp. 56–67, 2017.

[33] X. She, A. Q. Huang, and R. Burgos, "Review of solid-state transformer technologies and their application in power distribution systems," *IEEE J. Emerg. Sel. Topics Power Electron.*, vol. 1, no. 3, pp. 186–198, 2013.

[34] S. Y. Hui, C. K. Lee, and F. F. Wu, "Electric springs-a new smart grid technology," *IEEE Trans. Smart Grid*, vol. 3, no. 3, pp. 1552–1561, 2012.

[35] J. C. Sanchez, M. Barnes, and J. Apsley, "Virtual energy storage: Converting an AC drive to a smart-load," *IEEE Trans. Energy Convers.*, vol. 33, no. 3, pp. 1342–1353, 2018.

[36] A. Elrayyah, F. Cingoz, and Y. Sozer, "Smart loads management using droop-based control in integrated microgrid systems," *IEEE J. Emerg. Sel. Topics Power Electron.*, vol. 5, no. 3, pp. 1142–1153, 2017.

[37] B. V. Solanki, A. Raghurajan, K. Bhattacharya, and C. A. Canizares, "Including smart loads for optimal demand response in integrated energy management systems for isolated microgrids," *IEEE Trans. Smart Grid*, vol. 8, no. 4, pp. 1739–1748, 2017.

[38] O. Hafez and K. Bhattacharya, "Integrating EV charging stations as smart loads for demand response provisions in distribution systems," *IEEE Trans. Smart Grid*, vol. 9, no. 2, pp. 1096–1106, 2018.

[39] A. Mondal, M. S. Illindala, A. S. Khalsa, D. A. Klapp, and J. H. Eto, "Design and operation of smart loads to prevent stalling in a microgrid," *IEEE Trans. Ind. Appl.*, vol. 52, no. 2, pp. 1184–1192, 2016.

[40] Y. Guan, J. C. Vasquez, J. M. Guerrero, Y. Wang, and W. Feng, "Frequency stability of hierarchically controlled hybrid photovoltaic-battery-hydropower microgrids," *IEEE Trans. Ind. Appl.*, vol. 51, no. 6, pp. 4729–4742, 2015.

[41] A. Mondal and M. S. Illindala, "Improved frequency regulation in an islanded mixed source microgrid through coordinated operation of DERs and smart loads," *IEEE Trans. Ind. Appl.*, vol. 54, no. 1, pp. 112–120, 2018.

[42] C. Sun, G. Joos, and F. Bouffard, "Adaptive coordination for power and SoC limiting control of energy storage in islanded AC microgrid with impact load," *IEEE Trans. Power Del.*, vol. 35, no. 2, pp. 580–591, 2019.

[43] P. Mercier, R. Cherkaoui, and A. Oudalov, "Optimizing a battery energy storage system for frequency control application in an isolated power system," *IEEE Trans. Power Syst.*, vol. 24, no. 3, pp. 1469–1477, 2009.

[44] P. F. Frack, P. E. Mercado, M. G. Molina, E. H. Watanabe, R. W. De Doncker, and H. Stagge, "Control strategy for frequency control in autonomous microgrids," *IEEE J. Emerg. Sel. Topics Power Electron.*, vol. 3, no. 4, pp. 1046–1055, 2015.

[45] M. Datta, T. Senjyu, A. Yona, T. Funabashi, and C.-H. Kim, "A frequency-control approach by photovoltaic generator in a PV-diesel hybrid power system," *IEEE Trans. Energy Convers.*, vol. 26, no. 2, pp. 559–571, 2011.

[46] A. Elmitwally and M. Rashed, "Flexible operation strategy for an isolated PV-diesel microgrid without energy storage," *IEEE Trans. Energy Convers.*, vol. 26, no. 1, pp. 235–244, 2011.

[47] M. Farrokhabadi, C. A. Canizares, and K. Bhattacharya, "Frequency control in isolated/islanded microgrids through voltage regulation," *IEEE Trans. Smart Grid*, vol. 8, no. 3, pp. 1185–1194, 2017.

[48] M. S. Pilehvar, M. B. Shadmand, and B. Mirafzal, "Analysis of smart loads in nanogrids," *IEEE Access*, vol. 7, pp. 548–562, 2019.

[49] K. A. Alobeidli, M. H. Syed, M. S. El Moursi, and H. H. Zeineldin, "Novel coordinated voltage control for hybrid micro-grid with islanding capability," *IEEE Trans. Smart Grid*, vol. 6, no. 3, pp. 1116–1127, 2015.

[50] H. R. Esmaeilian and R. Fadaeinedjad, "A remedy for mitigating voltage fluctuations in small remote wind-diesel systems using network theory concepts," *IEEE Trans. Smart Grid*, vol. 9, no. 5, pp. 4162–4171, 2018.

[51] J.-Y. Kim, J.-H. Jeon, S.-K. Kim, C. Cho, J. H. Park, H.-M. Kim, and K.-Y. Nam, "Cooperative control strategy of energy storage system and microsources for stabilizing the microgrid during islanded operation," *IEEE Trans. Power Electron.*, vol. 25, no. 12, pp. 3037–3048, 2010.

[52] Y.-S. Kim, E.-S. Kim, and S.-I. Moon, "Frequency and voltage control strategy of standalone microgrids with high penetration of intermittent renewable generation systems," *IEEE Trans. Power Syst.*, vol. 31, no. 1, pp. 718–728, 2016.

[53] H. M. Ibrahim, M. S. El Moursi, and P.-H. Huang, "Adaptive roles of islanded microgrid components for voltage and frequency transient responses enhancement," *IEEE Trans. Ind. Informat.*, vol. 11, no. 6, pp. 1298–1312, 2015.

[54] Q. Sun, J. Zhou, J. M. Guerrero, and H. Zhang, "Hybrid three-phase/single-phase microgrid architecture with power management capabilities," *IEEE Trans. Power Electron.*, vol. 30, no. 10, pp. 5964–5977, 2014.

[55] S. Anwar, A. Elrayyah, and Y. Sozer, "Efficient single-phase harmonics elimination method for microgrid operations," *IEEE Trans. Ind. Appl.*, vol. 51, no. 4, pp. 3394–3403, 2015.

[56] C. Wang, P. Yang, C. Ye, Y. Wang, and Z. Xu, "Voltage control strategy for three/single phase hybrid multimicrogrid," *IEEE Trans. Energy Convers.*, vol. 31, no. 4, pp. 1498–1509, 2016.

[57] R. Majumder, "Reactive power compensation in single-phase operation of microgrid," *IEEE Trans. Ind. Electron.*, vol. 60, no. 4, pp. 1403–1416, 2012.

[58] S. M. Ashabani and Y. A.-R. I. Mohamed, "A flexible control strategy for grid-connected and islanded microgrids with enhanced stability using nonlinear microgrid stabilizer," *IEEE Trans. Smart Grid*, vol. 3, no. 3, pp. 1291–1301, 2012.

[59] D. S. Ochs, B. Mirafzal, and P. Sotoodeh, "A method of seamless transitions between grid-tied and stand-alone modes of operation for utility-interactive three-phase inverters," *IEEE Trans. Ind. Appl.*, vol. 50, no. 3, pp. 1934–1941, 2014.

[60] T. L. Vandoorn, B. Meersman, J. D. De Kooning, and L. Vandevelde, "Transition from islanded to grid-connected mode of microgrids with voltage-based droop control," *IEEE Trans. Power Syst.*, vol. 28, no. 3, pp. 2545–2553, 2013.

[61] S. H. Lee, G. Son, and J.-W. Park, "Power management and control for grid-connected DGs with intentional islanding operation of inverter," *IEEE Trans. Power Syst.*, vol. 28, no. 2, pp. 1235–1244, 2012.

[62] C.-T. Lee, R.-P. Jiang, and P.-T. Cheng, "A grid synchronization method for droop-controlled distributed energy resource converters," *IEEE Trans. Ind. Appl.*, vol. 49, no. 2, pp. 954–962, 2013.

[63] T. M. L. Assis and G. N. Taranto, "Automatic reconnection from intentional islanding based on remote sensing of voltage and frequency signals," *IEEE Trans. Smart Grid*, vol. 3, no. 4, pp. 1877–1884, 2012.

[64] J. M. Bloemink and M. R. Iravani, "Control of a multiple source microgrid with built-in islanding detection and current limiting," *IEEE Trans. Power Del.*, vol. 27, no. 4, pp. 2122–2132, 2012.

[65] X. Hou, Y. Sun, J. Lu, X. Zhang, L. H. Koh, M. Su, and J. M. Guerrero, "Distributed hierarchical control of AC microgrid operating in grid-connected, islanded and their transition modes," *IEEE Access*, vol. 6, pp. 77 388–77 401, 2018.

[66] C. Papadimitriou, V. Kleftakis, and N. Hatziargyriou, "Control strategy for seamless transition from islanded to interconnected operation mode of microgrids," *J. Modern Power Syst. Clean Energy*, vol. 5, no. 2, pp. 169–176, 2017.

[67] M. Pipattanasomporn, H. Feroze, and S. Rahman, "Multi-agent systems in a distributed smart grid: Design and implementation," in *2009 IEEE/PES Power Systems Conference and Exposition*, 2009, pp. 1–8.

[68] A. Elmitwally, M. Elsaid, M. Elgamal, and Z. Chen, "A fuzzy-multiagent self-healing scheme for a distribution system with distributed generations," *IEEE Trans. Power Syst.*, vol. 30, no. 5, pp. 2612–2622, 2014.

[69] A. Micallef, M. Apap, C. Spiteri-Staines, and J. M. Guerrero, "Single-phase microgrid with seamless transition capabilities between modes of operation," *IEEE Trans. Smart Grid*, vol. 6, no. 6, pp. 2736–2745, 2015.

[70] J. Kim, J. M. Guerrero, P. Rodriguez, R. Teodorescu, and K. Nam, "Mode adaptive droop control with virtual output impedances for an inverter-based flexible ac microgrid," *IEEE Trans. Power Electron.*, vol. 26, no. 3, pp. 689–701, 2010.

[71] J. C. Vasquez, J. M. Guerrero, A. Luna, P. RodrÃguez, and R. Teodorescu, "Adaptive droop control applied to voltage-source inverters operating in grid-connected and islanded modes," *IEEE Trans. Ind. Electron.*, vol. 56, no. 10, pp. 4088–4096, 2009.

[72] H. Han, X. Hou, J. Yang, J. Wu, M. Su, and J. M. Guerrero, "Review of power sharing control strategies for islanding operation of ac microgrids," *IEEE Trans. Smart Grid*, vol. 7, no. 1, pp. 200–215, 2016.

[73] S. A. Raza and J. Jiang, "A benchmark distribution system for investigation of residential microgrids with multiple local generation and storage devices," *IEEE Open Access J. Power and Energy*, vol. 7, pp. 41–50, 2019.

[74] B. Mirafzal and A. Adib, "On grid-interactive smart inverters: Features and advancements," *IEEE Access*, vol. 8, pp. 160 526–160 536, 2020.

[75] A. Adib, J. Lamb, and B. Mirafzal, "Ancillary services via VSIs in microgrids with maximum DC-bus voltage utilization," *IEEE Trans. Ind. Appl.*, vol. 55, no. 1, pp. 648–658, 2018.

[76] A. Adib, J. Lamb, and B. Mirafzal, "Atypical PWM for maximizing 2l-VSI DC-bus utilization in inverter-based microgrids with ancillary services," in *2018 IEEE Applied Power Electronics Conference and Exposition (APEC)*, 2018, pp. 2343–2348.

[77] F. Sadeque, J. Benzaquen, A. Adib, and B. Mirafzal, "Direct phase-angle detection for three-phase inverters in asymmetrical power grids," *IEEE J. Emerg. Sel. Topics Power Electron.*, 2020.

[78] A. Adib, F. Fateh, and B. Mirafzal, "Smart inverter stability enhancement in weak grids using adaptive virtual-inductance," *IEEE Trans. Ind. Appl.*, 2020.

[79] G. De Carne, G. Buticchi, M. Liserre, and C. Vournas, "Load control using sensitivity identification by means of smart transformer," *IEEE Trans. Smart Grid*, vol. 9, no. 4, pp. 2606–2615, 2018.

[80] Z.-X. Zou, G. De Carne, G. Buticchi, and M. Liserre, "Smart transformer-fed variable frequency distribution grid," *IEEE Trans. Ind. Electron.*, vol. 65, no. 1, pp. 749–759, 2018.

[81] M. S. Pilehvar, M. B. Shadmand, and B. Mirafzal, "Smart loads for power quality and battery lifetime improvement in nanogrids," in *2019 IEEE Applied Power Electronics Conference and Exposition (APEC)*, 2019, pp. 2029–2034.

[82] J. Soni and S. K. Panda, "Electric spring for voltage and power stability and power factor correction," *IEEE Trans. Ind. Appl.*, vol. 53, no. 4, pp. 3871–3879, 2017.

[83] R. S. Pawar, S. Gawande, S. Kadwane, M. A. Waghmare, and R. Nagpure, "Electric spring configurations: Comprehensive analysis," in *2018 International Conference on Power, Instrumentation, Control and Computing (PICC)*, 2018, pp. 1–6.

[84] Z. Akhtar, B. Chaudhuri, and S. Y. R. Hui, "Smart loads for voltage control in distribution networks," *IEEE Trans. Smart Grid*, vol. 8, no. 2, pp. 937–946, 2017.

[85] L. Liang, Y. Hou, and D. J. Hill, "Enhancing flexibility of an islanded microgrid with electric springs," *IEEE Trans. Smart Grid*, vol. 10, no. 1, pp. 899–909, 2019.

[86] T. Yang, K.-T. Mok, S.-C. Tan, C. K. Lee, and S. Y. Hui, "Electric springs with coordinated battery management for reducing voltage and frequency fluctuations in microgrids," *IEEE Trans. Smart Grid*, vol. 9, no. 3, pp. 1943–1952, 2018.

[87] S. Yan, S.-C. Tan, C.-K. Lee, B. Chaudhuri, and S. R. Hui, "Electric springs for reducing power imbalance in three-phase power systems," *IEEE Trans. Power Electron.*, vol. 30, no. 7, pp. 3601–3609, 2015.

[88] P. Krause, O. Wasynczuk, S. D. Sudhoff, and S. Pekarek, *Analysis of electric machinery and drive systems*. John Wiley & Sons, 2013, vol. 75.

[89] R. H. Park, "Two-reaction theory of synchronous machines generalized method of analysis-part I," *Transactions of the American Institute of Electrical Engineers*, vol. 48, no. 3, pp. 716–727, 1929.

[90] A. Adib, B. Mirafzal, X. Wang, and F. Blaabjerg, "On stability of voltage source inverters in weak grids," *IEEE Access*, vol. 6, pp. 4427–4439, 2018.

[91] A. Singh, A. K. Kaviani, and B. Mirafzal, "On dynamic models and stability analysis of three-phase phasor PWM-based CSI for stand-alone applications," *IEEE Trans. Ind. Electron.*, vol. 62, no. 5, pp. 2698–2707, 2015.

[92] M. S. Pilehvar, J. Benzaquen, M. B. Shadmand, A. Pahwa, B. Mirafzal, J. McDaniel, D. Rogge, and J. Erickson, "Modeling, control, and stability of smart loads toward grid of nanogrids for smart cities," *in Proc. 44th Annu. Conf. IEEE Ind. Electron. Soc. (IECON)*, 2018.

[93] H. A. Catherino, F. F. Feres, and F. Trinidad, "Sulfation in lead acid-batteries," *J. Power Sources*, vol. 129, no. 1, pp. 113–120, 2004.

[94] D. Wu, R. Todd, and A. J. Forsyth, "Adaptive rate-limit control for energy storage systems," *IEEE Trans. Industrial Electron.*, vol. 62, no. 7, pp. 4231–4240, 2015.

[95] M. S. Pilehvar and B. Mirafzal, "Frequency and voltage supports by battery-fed smart inverters in mixed-inertia microgrids," *Electronics*, vol. 9, p. 1755, 2020.

[96] M. S. Pilehvar and B. Mirafzal, "A frequency control method for islanded microgrids using energy storage systems," in *2020 IEEE Applied Power Electronics Conference and Exposition (APEC)*, 2020, pp. 2327–2332.

[97] M. S. Pilehvar and B. Mirafzal, "Energy-storage fed smart inverters for mitigation of voltage fluctuations in islanded microgrids," *in 2020 IEEE Electric Power and Energy Conference (EPEC)*, 2020.

[98] N. Soni, S. Doolla, and M. C. Chandorkar, "Improvement of transient response in microgrids using virtual inertia," *IEEE Trans. Power Del.*, vol. 28, no. 3, pp. 1830–1838, 2013.

[99] F. Chen, R. Burgos, D. Boroyevich, J. C. Vasquez, and J. M. Guerrero, "Investigation of nonlinear droop control in dc power distribution systems: Load sharing, voltage regulation, efficiency, and stability," *IEEE Trans. Power Electron.*, vol. 34, no. 10, pp. 9404–9421, 2019.

[100] F. Cingoz, A. Elrayyah, and Y. Sozer, "Plug-and-play nonlinear droop construction scheme to optimize islanded microgrid operations," *IEEE Trans. Power Electron.*, vol. 32, no. 4, pp. 2743–2756, 2016.

[101] M. S. Pilehvar and B. Mirafzal, "PV-fed smart inverters for mitigation of voltage and frequency fluctuations in islanded microgrids," in *2020 IEEE International Conference on Smart Grids and Energy Systems (SGES)*, 2020.

[102] J. Benzaquen, M. B. Shadmand, and B. Mirafzal, "Ultrafast rectifier for variable-frequency applications," *IEEE Access*, vol. 7, pp. 9903–9911, 2019.

[103] M. S. Pilehvar and B. Mirafzal, "Interconnection of three single-phase feeders in North America distribution systems," in *2020 IEEE International Conference on Smart Grids and Energy Systems (SGES)*, 2020.

[104] M. S. Pilehvar and B. Mirafzal, "Smart inverters for seamless reconnection of isolated residential microgrids to utility grid," *in 2020 IEEE Electric Power and Energy Conference (EPEC)*, 2020.

[105] J. Ahmad, M. Tahir, and S. K. Mazumder, "Improved dynamic performance and hierarchical energy management of microgrids with energy routing," *IEEE Trans. Ind. Informat.*, vol. 15, no. 6, pp. 3218–3229, 2018.

[106] A. Singh, A. A. Milani, and B. Mirafzal, "Voltage regulation in single-stage boost inverter for stand-alone applications," in *2014 IEEE Applied Power Electronics Conference and Exposition - APEC 2014*, 2014, pp. 3011–3016.

[107] A. Singh and B. Mirafzal, "A generator-converter topology with zero dc-link impedance for direct drive wind turbines," *IEEE Trans. Energy Convers.*, vol. 32, no. 4, pp. 1620–1623, 2017.

[108] A. Singh and B. Mirafzal, "Three-phase single-stage boost inverter for direct drive wind turbines," in *2016 IEEE Energy Conversion Congress and Exposition (ECCE)*, 2016, pp. 1–7.

[109] A. Singh and B. Mirafzal, "Indirect boost matrix converter and low-voltage generator for direct drive wind turbines," *The Journal of Engineering*, vol. 2018, no. 1, pp. 10–16, 2018.

[110] A. Singh, J. Benzaquen, and B. Mirafzal, "Current source generator-converter topology for direct-drive wind turbines," *IEEE Trans. Ind. Appl.*, vol. 54, no. 2, pp. 1663–1670, 2018.

[111] A. Singh, A. K. Kaviani, and B. Mirafzal, "On dynamic models and stability analysis of three-phase phasor PWM-based CSI for stand-alone applications," *IEEE Trans. Ind. Electron.*, vol. 62, no. 5, pp. 2698–2707, 2015.

[112] J. Lamb and B. Mirafzal, "Open-circuit IGBT fault detection and location isolation for cascaded multilevel converters," *IEEE Trans. Ind. Electron.*, vol. 64, no. 6, pp. 4846–4856, 2017.

[113] J. Lamb and B. Mirafzal, "An adaptive SPWM technique for cascaded multilevel converters with time-variant DC sources," *IEEE Trans. Ind. Appl.*, vol. 52, no. 5, pp. 4146–4155, 2016.

[114] J. Lamb and B. Mirafzal, "Grid-interactive cascaded H-bridge multilevel converter PQ plane operating region analysis," *IEEE Trans. Ind. Appl.*, vol. 53, no. 6, pp. 5744–5752, 2017.

[115] J. Lamb and B. Mirafzal, "An adaptive SPWM technique for cascaded multilevel converters," in *2015 IEEE Energy Conversion Congress and Exposition (ECCE)*, 2015, pp. 703–708.

[116] J. Lamb and B. Mirafzal, "Active and reactive power operational region for grid-interactive cascaded H-bridge multilevel converters," in *2016 IEEE Energy Conversion Congress and Exposition (ECCE)*, 2016, pp. 1–6.

[117] M. H. Rashid, *Alternative energy in power electronics*. Butterworth-Heinemann, 2014.

[118] J. Liu, Y. Miura, and T. Ise, "Comparison of dynamic characteristics between virtual synchronous generator and droop control in inverter-based distributed generators," *IEEE Trans. Power Electron.*, vol. 31, no. 5, pp. 3600–3611, 2015.

[119] P. Kundur, N. J. Balu, and M. G. Lauby, *Power system stability and control*. McGraw-hill New York, 1994, vol. 7.

[120] I. S. 421.5., "Ieee recommended practice for excitation system models for power system stability studies," 2005.

[121] C. M. Model, "C65 user's manual," *Capstone Turbine Corporation: Chatsworth, CA, USA*, 2007.

Appendix A

State-Space Matrices of Smart Loads

In this appendix, the full-form of matrices introduced in the state-space model of smart loads throughout Section 2.4 are provided. To this end, the full-form of matrices A_v, $B1_v$, $B2_v$, and $B3_v$ in (2.14) can be expressed as follows:

$$A_v = \begin{bmatrix} 0 & 0 \\ 0 & 0 \end{bmatrix}, \tag{A.1}$$

$$B1_v = \begin{bmatrix} 1 & 0 \\ 0 & 1 \end{bmatrix}, \tag{A.2}$$

$$B2_v = \begin{bmatrix} -R & -\omega L \\ \omega L & -R \end{bmatrix}, \tag{A.3}$$

$$B3_v = \begin{bmatrix} -Li_{\mathrm{CL\_}d} \\ Li_{\mathrm{CL\_}q} \end{bmatrix}. \tag{A.4}$$

The full-form of matrices C_v, $D1_v$, $D2_v$, and $D3_v$ introduced in (2.15) can be obtained as follows:

$$C_v = \begin{bmatrix} K_{Ivq} & 0 \\ 0 & K_{Ivd} \end{bmatrix}, \tag{A.5}$$

$$D1_v = \begin{bmatrix} K_{Pvq} & 0 \\ 0 & K_{Pvd} \end{bmatrix}, \tag{A.6}$$

$$D2_v = \begin{bmatrix} -RK_{Pvq} & -\omega LK_{Pvq} \\ \omega LK_{Pvd} & -RK_{Pvd} \end{bmatrix}, \tag{A.7}$$

$$D3_v = \begin{bmatrix} -LK_{Pvq} i_{\mathrm{CL\_}d} \\ LK_{Pvd} i_{\mathrm{CL\_}q} \end{bmatrix}. \tag{A.8}$$

Matrix M in (2.24) can be expressed as follows:

$$M = \begin{bmatrix} V_{\mathrm{bat}} \cos(\psi) & -mV_{\mathrm{bat}} \sin(\psi) \\ -V_{\mathrm{bat}} \sin(\psi) & -mV_{\mathrm{bat}} \cos(\psi) \end{bmatrix}. \tag{A.9}$$

The full-form of matrices A_{OL}, $B1_{\mathrm{OL}}$, $B2_{\mathrm{OL}}$, and $B3_{\mathrm{OL}}$ introduced in (2.26) are provided below:

$$A_{\mathrm{OL}} = \begin{bmatrix} -\frac{3R_{f1}+R_{f2}}{3L_f} & -\omega & -\frac{1}{2L_f} & \frac{\sqrt{3}}{6L_f} & \frac{R_{f2}}{3L_f} & 0 & 0 & 0 \\ \omega & -\frac{3R_{f1}+R_{f2}}{3L_f} & -\frac{\sqrt{3}}{6L_f} & -\frac{1}{2L_f} & 0 & \frac{R_{f2}}{3L_f} & 0 & 0 \\ \frac{1}{2C_f} & \frac{\sqrt{3}}{6C_f} & 0 & -\omega & -\frac{1}{2C_f} & -\frac{\sqrt{3}}{6C_f} & 0 & 0 \\ -\frac{\sqrt{3}}{6C_f} & \frac{1}{2C_f} & \omega & 0 & \frac{\sqrt{3}}{6C_f} & -\frac{1}{2C_f} & 0 & 0 \\ \frac{R_{f2}}{3L_t} & 0 & \frac{1}{2L_t} & -\frac{\sqrt{3}}{6L_t} & -\frac{3R_t+R_{f2}}{3L_t} & -\omega & 0 & 0 \\ 0 & \frac{R_{f2}}{3L_t} & \frac{\sqrt{3}}{6L_t} & \frac{1}{2L_t} & \omega & -\frac{3R_t+R_{f2}}{3L_t} & 0 & 0 \\ 0 & 0 & 0 & 0 & 0 & 0 & -\frac{R}{L} & -\omega \\ 0 & 0 & 0 & 0 & 0 & 0 & \omega & -\frac{R}{L} \end{bmatrix}, \tag{A.10}$$

$$B1_{\mathrm{OL}} = \begin{bmatrix} \frac{V_{\mathrm{bat}}\cos(\psi)}{\sqrt{3}L_f} & -\frac{V_{\mathrm{bat}}\sin(\psi)}{\sqrt{3}L_f} & 0 & 0 & 0 & 0 & 0 & 0 \\ -\frac{mV_{\mathrm{bat}}\sin(\psi)}{\sqrt{3}L_f} & -\frac{mV_{\mathrm{bat}}\cos(\psi)}{\sqrt{3}L_f} & 0 & 0 & 0 & 0 & 0 & 0 \end{bmatrix}^T, \tag{A.11}$$

$$B2_{\mathrm{OL}} = \begin{bmatrix} 0 & 0 & 0 & 0 & -\frac{1}{2L_t} & -\frac{\sqrt{3}}{6L_t} & -\frac{1}{L} & 0 \\ 0 & 0 & 0 & 0 & \frac{\sqrt{3}}{6L_t} & -\frac{1}{2L_t} & 0 & -\frac{1}{L} \\ 0 & 0 & 0 & 0 & 0 & 0 & \frac{1}{L} & 0 \\ 0 & 0 & 0 & 0 & 0 & 0 & 0 & \frac{1}{L} \end{bmatrix}^T, \tag{A.12}$$

$$B3_{\mathrm{OL}} = \begin{bmatrix} -i_{\mathrm{EDp\_}d} & i_{\mathrm{EDp\_}q} & -v_{\mathrm{EDp\_}d} & v_{\mathrm{EDp\_}q} & -i_{\mathrm{ED\_}d} & i_{\mathrm{ED\_}q} & -i_{\mathrm{CL\_}d} & i_{\mathrm{CL\_}q} \end{bmatrix}^T. \tag{A.13}$$

The full-form of matrices $A_{\mathrm{SCL}i}$, $B1_{\mathrm{SCL}i}$, $B2_{\mathrm{SCL}i}$, $B3_{\mathrm{SCL}i}$, and $\triangle x_{\mathrm{SCL}i}$ in (2.27) can be expressed as follows:

$$A_{\mathrm{SCL}i} = \begin{bmatrix} [0]_{2\times2} & [0]_{2\times2} & \begin{bmatrix} [0]_{2\times6} & B2_{vi} \end{bmatrix}_{2\times8} \\ B1_{ci}C_{vi} & [0]_{2\times2} & \begin{bmatrix} [0]_{2\times6} & B1_{ci}D2_{vi} + B2_{ci} \end{bmatrix}_{2\times8} \\ B1_{\mathrm{OL}i}M_i^{-1}D1_{ci}C_{vi} & B1_{\mathrm{OL}i}M_i^{-1}C_{ci} & A_{\mathrm{OL}i} + \begin{bmatrix} [0]_{8\times6} & B1_{\mathrm{OL}i}M_i^{-1}\left[D1_{ci}D2_{vi} + D2_{ci}\right] \end{bmatrix}_{8\times8} \end{bmatrix}_{12\times12} \tag{A.14}$$

$$B1_{\mathrm{SCL}i} = \begin{bmatrix} B1_{vi} \\ B1_{ci}D1_{vi} \\ B1_{\mathrm{OL}i}M_i^{-1}D1_{ci}D1_{vi} \end{bmatrix}_{12\times2}, \tag{A.15}$$

$$B2_{\mathrm{SCL}i} = \begin{bmatrix} [0]_{2\times4} \\ [0]_{2\times4} \\ B2_{\mathrm{OL}i} + \begin{bmatrix} [0]_{8\times2} & B1_{\mathrm{OL}i}M_i^{-1}D3_{ci} \end{bmatrix}_{8\times4} \end{bmatrix}_{12\times4}, \tag{A.16}$$

$$B3_{\mathrm{SCL}i} = \begin{bmatrix} B3_{vi} \\ B1_{ci}D3_{vi} \\ B3_{\mathrm{OL}i} + B1_{\mathrm{OL}i}M_i^{-1}D1_{ci}D3_{vi} \end{bmatrix}_{12\times 1}, \tag{A.17}$$

$$\Delta x_{\mathrm{SCL}i} = \begin{bmatrix} \Delta\chi_{i\_qd} & \Delta y_{i\_qd} & \Delta i_{\mathrm{EDp}i\_qd} & \Delta v_{\mathrm{EDp}i\_qd} & \Delta i_{\mathrm{ED}i\_qd} & \Delta i_{\mathrm{CL}i\_qd} \end{bmatrix}^T. \tag{A.18}$$

Appendix B

Modeling and Control of BESS, PV Units, Diesel Generator, and Microturbine System

The main objective of this appendix is to explain in detail the control schemes of DG units which have not been expanded through the main context of the dissertation. To this end, the detailed control schemes of BESS, PV units, diesel generator, and microturbine system shown in Figs. 2.14, 3.1, 2.18, and 3.10 are provided in this appendix.

B.1 Modeling and Control of BESS

The BESSs employed on the generation sides of nanogrids and microgrids shown in Figs. 2.14, 2.18, and 3.10 operate in PQ control (or grid following) mode as an energy buffer to inject/absorb the deficit/extra power during the steady-state condition. During normal operation and in the presence of renewable energy resources, when a nanogrid/microgrid is connected to the main grid, BESS is necessary to ensure that none of the energy generated goes to waste. For example, if a solar panel is connected to the grid without energy storage, no excess power produced will be used locally. If the sun moves behind a cloud or the

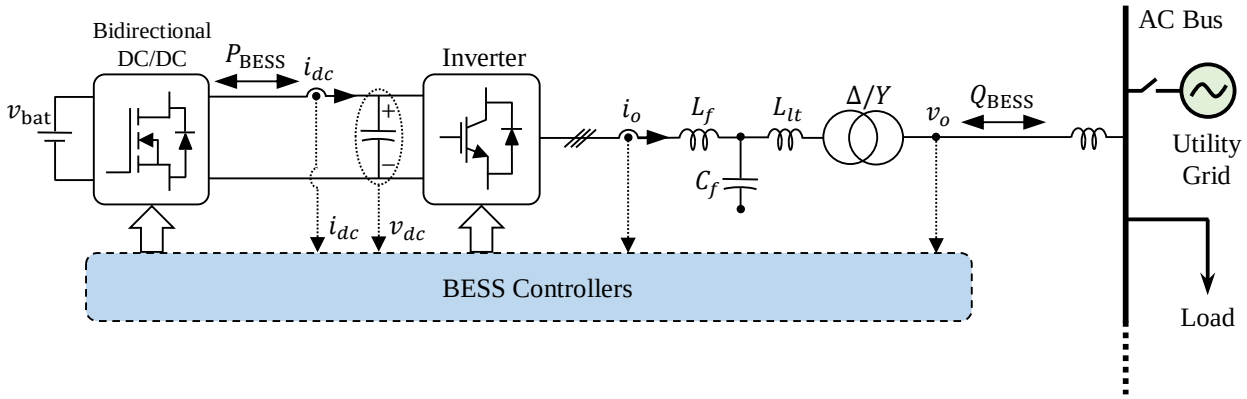

Figure B.1: Basic structure of BESS operating in grid-following mode.

wind stops blowing, a nanogrid/microgrid can engage its stored energy while waiting for the alternative generation source to come back online.

B.1.1 Basic Structure of BESS

The basic structure of BESSs which are employed as a back up during the steady-state condition in this dissertation is shown in Fig. B.1. This system consists of a battery bank, which is connected to the ac bus through a bidirectional dc-dc converter and a dc-ac inverter. Herein, the inverter implies the conventional two-level voltage source inverter. However, current source inverter [106–111] and multilevel voltage source inverter [112–116] are the other conventional inverters. The bidirectional dc-dc converter is crucial for the charging/discharging operation of BESS. During the discharge mode, the battery bank supplies power, the dc-dc converter boosts the voltage to the level required for the proper operation of the dc-ac inverter. During the charge mode, the direction of power flow through BESS changes and the dc link acts as the input voltage source for the dc-dc converter. The bidirectional dc-dc converter then operates in buck mode, chopping the dc-link voltage to the specifications of the battery bank. The dc-dc converter consists of two switches which control the charge/discharge process. Both dc-dc converter and dc-ac inverter have their own controllers which enable the BESS to inject/absorb the predefined active and reactive power during the steady-state condition.

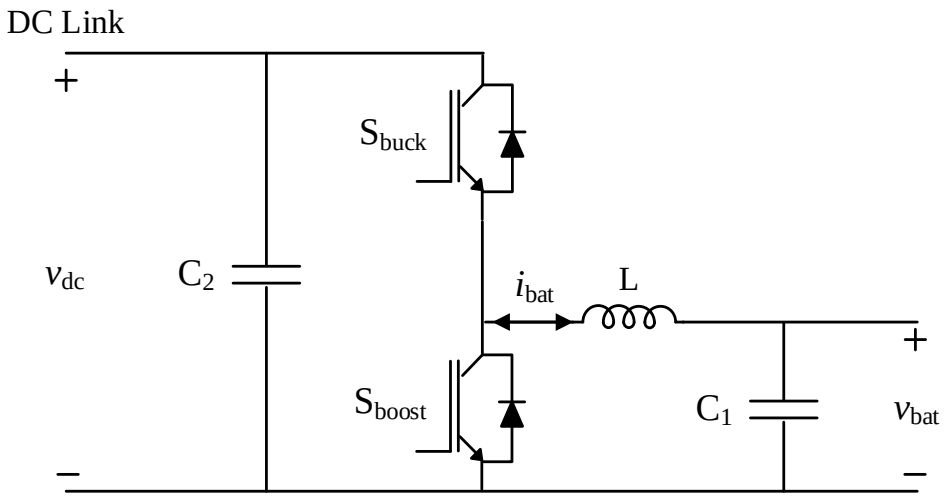

Figure B.2: Bidirectional dc-dc converter in BESS.

B.1.2 Control Scheme of BESS

This subsection explains the detailed control schemes of bidirectional dc-dc converter and dc-ac inverter implemented in BESS.

B.1.2.1 Bidirectional DC-DC Converter Controller

As previously mentioned, the battery bank is connected to the ac bus through a bidirectional dc-dc converter and a dc-ac inverter. As can be seen in Fig. B.2, the bidirectional dc-dc converter includes two semiconductor switches, i.e., S_{buck} and S_{boost}, that control the direction of power flow. Fig. B.3 explains the detailed control process of battery bank which operates in PQ control mode (or grid following) during both grid-connected and islanded modes of operation. During both modes, the bidirectional dc-dc converter controls the active power, i.e., P_{BESS}, injected or absorbed by battery bank.

The dc-dc converter operates in charging or discharging mode depending on its reference power, i.e., P^*_{BESS}. If the reference power is more than zero, i.e., $P^*_{BESS} > 0$, then the battery will be in discharge mode, while if the reference power is lower than zero, i.e. $P^*_{BESS} < 0$, then the battery will absorb power, and consequently, it will be operating in charge mode. The reference power can be set using an EMS. For example, the battery can be set to be in charge mode during noon when the PV arrays generate more power than what is required

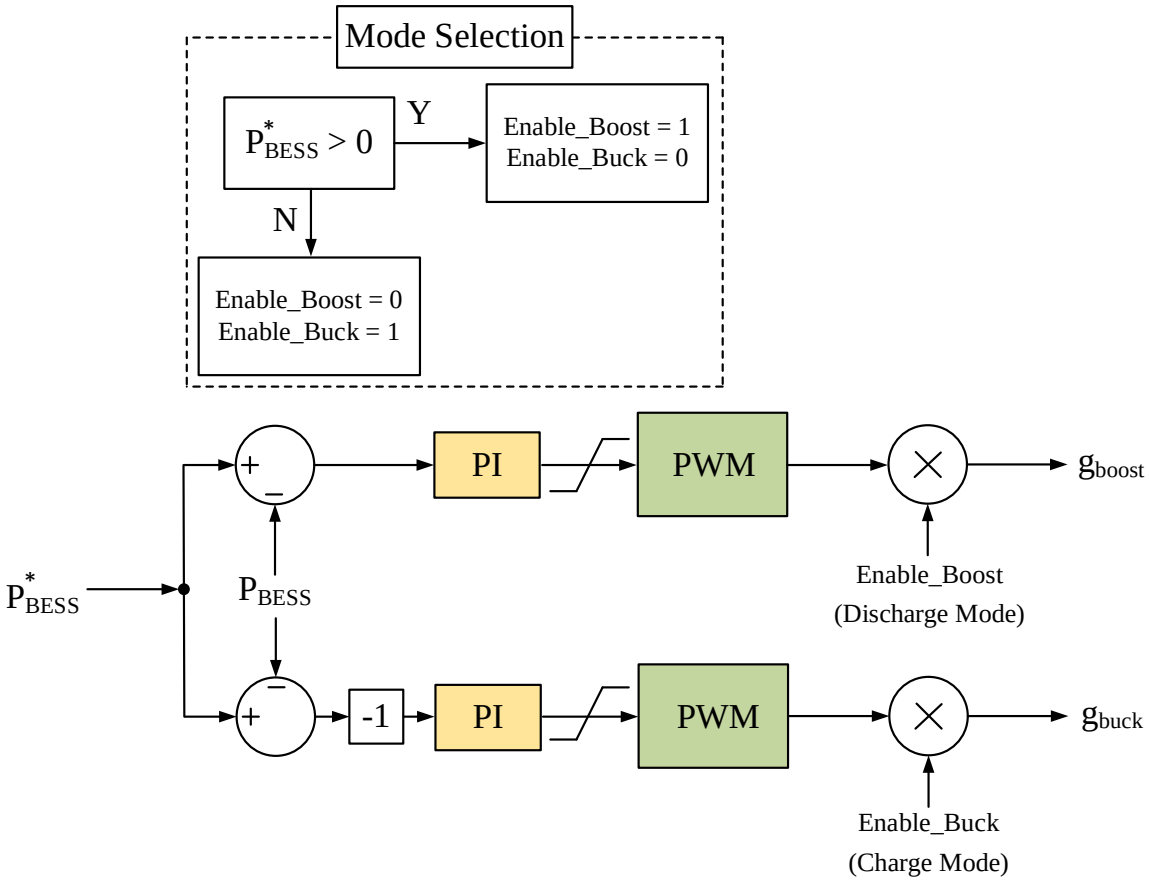

Figure B.3: Battery charge/discharge mode controller (or bidirectional dc-dc converter buck/boost mode controller) for both grid-connected and islanded modes of operation.

by the local loads. On the other hand, the battery can be set to operate in discharge mode during evenings and nights when no solar power is generated. The battery controller consists of two PI controllers. Based on the output of the controllers, the gate pulses for S_{buck} and S_{boost} are generated using a PWM approach.

As illustrated in Fig. B.3, the battery (or bidirectional dc-dc converter) controller has two control loops for generating two switching signals, i.e., g_{boost} and g_{buck}, assigned to the two semiconductor switches, i.e., S_{boost} and S_{buck}, respectively. When operating in discharge or boost mode, g_{buck} is set to zero, and consequently, S_{buck} remains open while S_{boost} is being turned on and off to provide the desired active power. Similarly, during charge or buck mode, S_{boost} remains open by setting g_{boost} equal to zero, while S_{buck} turns on and off repeatedly. Hence, two switching pulses, i.e., g_{boost} and g_{buck}, are the final outputs of the controller.

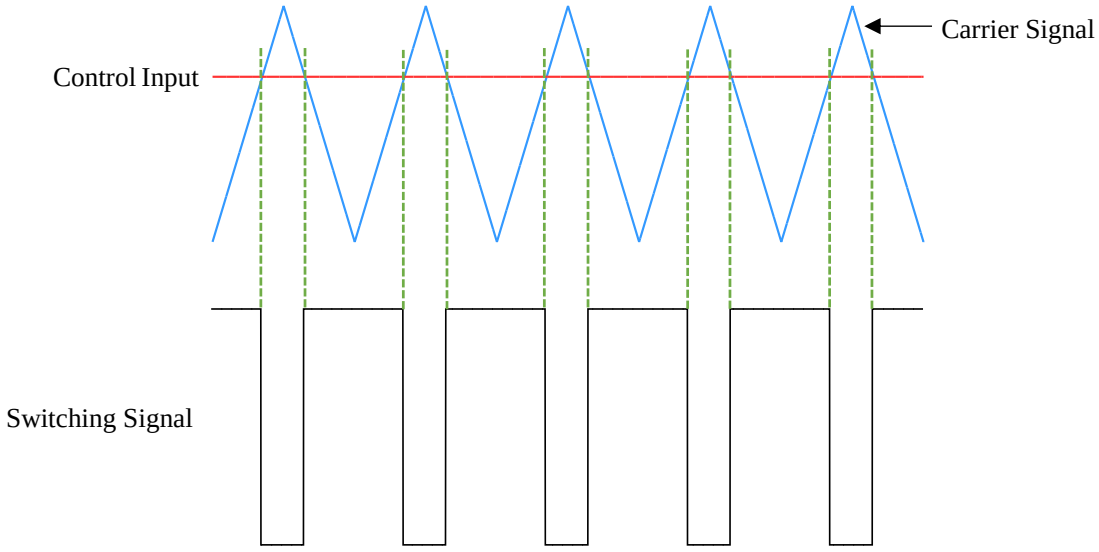

Figure B.4: Switching signal generation through PWM for bidirectional dc-dc converter.

The PWM block generates switching signals for the semiconductor switches, i.e., S_{buck} and S_{boost} in Fig. B.2. The switching signals are generated by comparing the input of the PWM block, which is referred as control input, with a high frequency triangular signal which is called carrier signal, as shown in Fig B.4. Depending on whether the control signal is higher or lower than the carrier signal, a high pulse or low pulse is sent to the gate terminals of S_{buck} and S_{boost}. It is to be noted that the control input for the PWM block is provided by the PI controller.

B.1.2.2 Inverter Controller

The dc-ac inverter is a crucial component for connecting renewable energy resources to the ac bus and supplying the loads. As illustrated in Fig. B.5, during both grid-connected and islanded modes, the inverter is responsible for regulating the dc-link voltage, i.e., v_{dc}, and controlling the reactive power transferred to/from BESS, i.e., Q_{BESS}. Besides, for both operation modes, the current references of inner-loop controller, i.e., i_d^* and i_q^*, can be enforced to proper limits to prevent overloading of the inverter. According to Fig. B.6, the measured PCC voltages, i.e., v_a, v_b, and v_c, and PCC currents, i.e., i_a, i_b, and i_c, are converted from

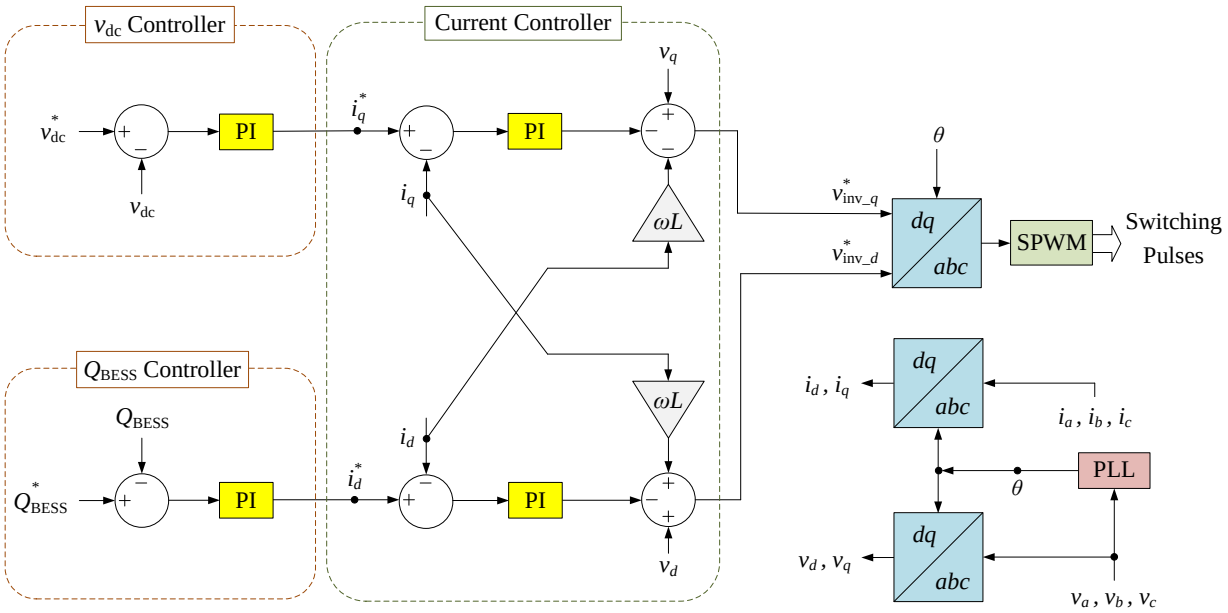

Figure B.5: Control scheme of BESS's inverter for both grid-connected and islanded modes of operation.

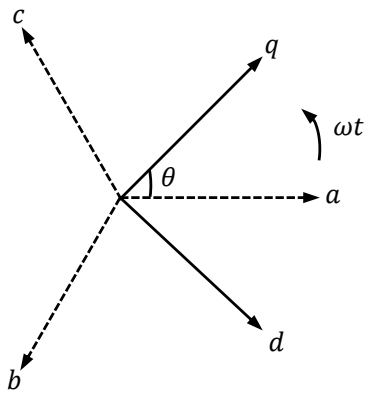

Figure B.6: *dq* frame of reference.

abc frame of reference to *dq* frame of reference using Park transformation [89] as follows:

$$\begin{bmatrix} x_q \\ x_d \\ x_0 \end{bmatrix} = \frac{2}{3} \begin{bmatrix} \cos(\omega t) & \cos(\omega t - 2\pi/3) & \cos(\omega t + 2\pi/3) \\ \sin(\omega t) & \sin(\omega t - 2\pi/3) & \sin(\omega t + 2\pi/3) \\ 1/2 & 1/2 & 1/2 \end{bmatrix} \begin{bmatrix} x_a \\ x_b \\ x_c \end{bmatrix} \tag{B.1}$$

For balanced three-phase systems, the x_0 is always zero. In the *dq* reference frame, the reference is synchronously rotating at the same frequency as the ac signals, and thus, the

signals effectively appear as dc with respect to the reference. This makes the controlling process easier, as the controllers have to regulate dc signals as opposed to the time-varying ac signals. Furthermore, the inverter controller has two inner-loop current controllers. The structure of the control loops can be determined by writing the Kirchhoff's voltage law (KVL) between the inverter terminal and the output of the LCL filter, and then, transferring it to the dq reference frame as follows:

$$v_{\text{inv\_}q} = v_q - R_f i_q - \omega L_f i_d - L_f \frac{di_q}{dt} \tag{B.2}$$

$$v_{\text{inv\_}d} = v_d - R_f i_d + \omega L_f i_q - L_f \frac{di_d}{dt} \tag{B.3}$$

where L_f is the combined inductance of the LCL filter and R_f is the associated resistance. The dq components of voltage at the PCC are denoted by v_d and v_q, while i_d and i_q are the dq components of current at the PCC. Besides, the dq components of inverter output voltage are denoted as $v_{\text{inv\_}d}$ and $v_{\text{inv\_}q}$. The derivative components are usually neglected for simplicity. The inner-loop current controller can be obtained using B.2 and B.3 with R_f used as an initial value for tuning the proportional gain of the controller. Since it is difficut to find the exact value of R_f, an integrator is also employed to eliminate any steady-state error. The reference values for the currents, i.e., i_d^* and i_q^*, are obtained from the outer-loop controller that regulates v_{dc} and Q_{BESS} as shown in Fig. B.5.

Similar to the dc-dc converter, the switching signals for dc-ac inverter are generated using a PWM scheme. However, in this scenario, the outputs of the controller are converted back to ac signals and these sinusoidal signals are used as control inputs. In addition, during grid-connected operation, it is necessary to synchronize the output voltage of the inverter with the grid-side voltage. A PLL plays an important role in this matter by extracting the phase angle of the grid voltage. The inverter output voltage is then generated at the PCC with the same phase angle as the grid voltage, and thus, synchronisation is guaranteed.

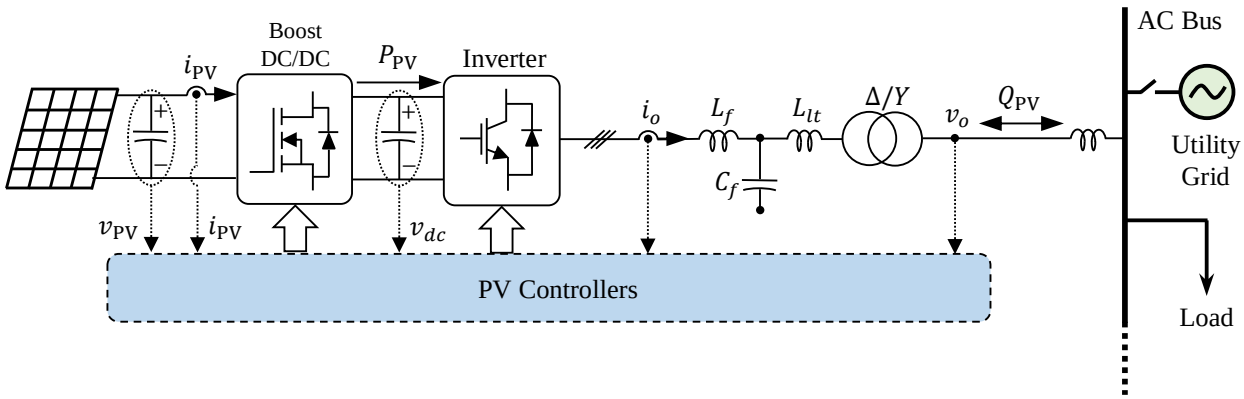

Figure B.7: Basic structure of PV units operating in grid-following mode.

B.2 Modeling and Control of PV Units

Regardless of the operation mode of the system, the PV units employed on the generation sides of nanogrids and microgrids illustrated in Figs. 2.14, 2.18, and 3.1 operate in PQ control (or grid following) mode to take the full advantage of clean and inexhaustible solar energy. This section describes the structure and control scheme of such PV systems with more details.

B.2.1 Basic Structure of PV Units

The basic structure of PV units operating in grid-following mode is shown in Fig. B.7. This system consists of PV panels, which are connected to the dc link through a dc-dc boost converter. A three-phase inverter is also used to convert the dc voltage to ac.

B.2.2 Control Scheme of PV Units

The detailed control schemes of boost dc-dc converter and dc-ac inverter employed in PV units are explained in this subsection.

B.2.2.1 Boost DC-DC Converter Controller

As previously mentioned, the PV arrays convert solar energy into dc current which can be used to supply the loads. The PV arrays are connected to the ac bus via a dc-dc boost

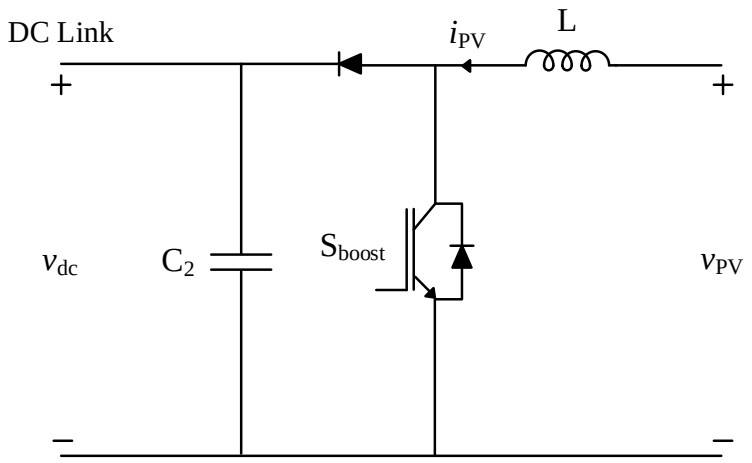

Figure B.8: Boost dc-dc converter in PV units.

converter and a three-phase dc-ac inverter. According to Fig. B.8, the dc-dc boost converter has only one switch, i.e., S_{boost}, which sends the generated power by PV arrays towards load and the grid. The detailed control strategy of dc-dc boost converter is shown in Fig. B.9. Due to the nonlinear characteristics of PV panels and the stochastic fluctuations of solar irradiance, there is a specific maximum power point (MPP) at every operating condition of PV array. For this reason, the MPPT algorithms are typically used in PV systems to extract the maximum power at different operating conditions. The proposed control system uses Perturb and Observe MPPT algorithm [117] to find the voltage in which the PV arrays will produce the maximum power, i.e., v_{MPPT}. Two possible control modes are considered for controlling the PV output power: (i) power-reference mode, and (ii) MPPT mode. Different parameters play a role in choosing the operation mode of PV arrays. For instance, during islanded mode, when the generated maximum power by PV arrays, i.e., $P_{\mathrm{PV\_MPPT}}$, is more than load demand, then the PV arrays will operate in power-reference mode. During MPPT mode, the instantaneous output voltage and current of PV arrays, i.e., v_{PV} and i_{PV}, are measured and sent to the MPPT module as inputs, and then, v_{MPPT} is provided as a voltage reference. An integrator (or PI controller) is then used to compute MPP as the reference power during the MPPT mode, i.e., $P_{\mathrm{PV\_MPPT}}$. The final output of the controller is a switching pulse, i.e., g_{boost}.

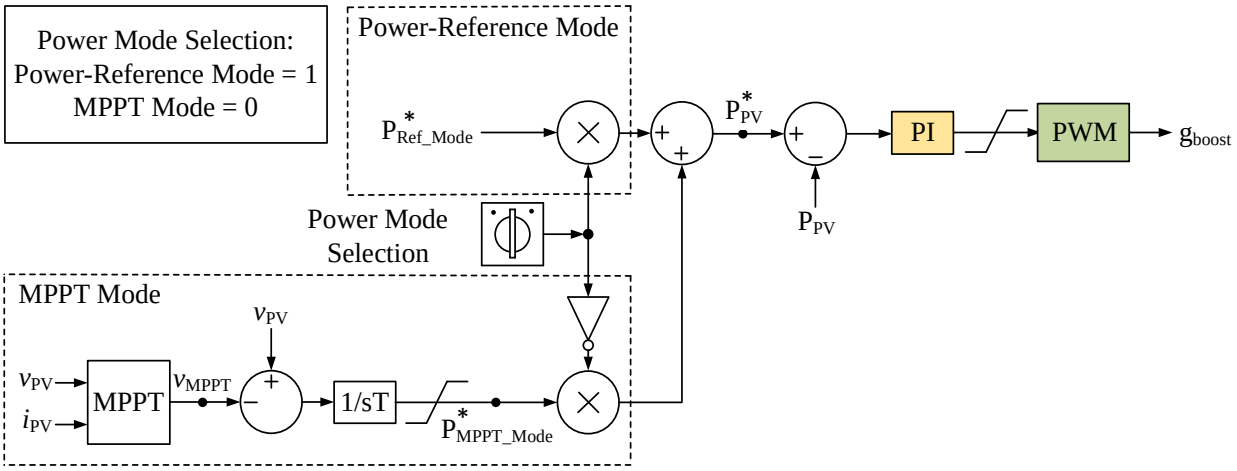

Figure B.9: Boost dc-dc converter controller for PV units during both grid-connected and islanded modes of operation.

B.2.2.2 Inverter Controller

Similar to BESS, the inverter is responsible for regulating the dc-bus voltage, i.e., $v_{\rm dc}$, and controlling the reactive power transferred to the ac side, i.e., $Q_{\rm PV}$, for both grid-connected and islanded modes, see Fig. B.10. Besides, to prevent overloading of the inverter, the current references of inner-loop controller, i.e., i_d^* and i_q^*, can be enforced to proper limits. A PLL is used to extract the angle of PCC voltage, i.e., θ. This angle is then used to decompose the three-phase ac-bus voltages and inverter output currents into dq reference frame using Park transformation as expressed in B.1.

B.3 Modeling and Control of Diesel Generator

This section provides an overview for the diesel generator which is used as a synchronous-based DG unit in this dissertation, along with its basic structure and controller design. The low cost of synchronous-based DGs has made them one of the main parts of mixed-inertia microgrids. These kind of DGs consist of a synchronous generator with a prime mover which is driven by an engine. Besides, AVR and governor are used for regulating the generator's terminal voltage and the speed of prime mover, respectively [14].

Droop control is one of the most common control methods employed in synchronous-

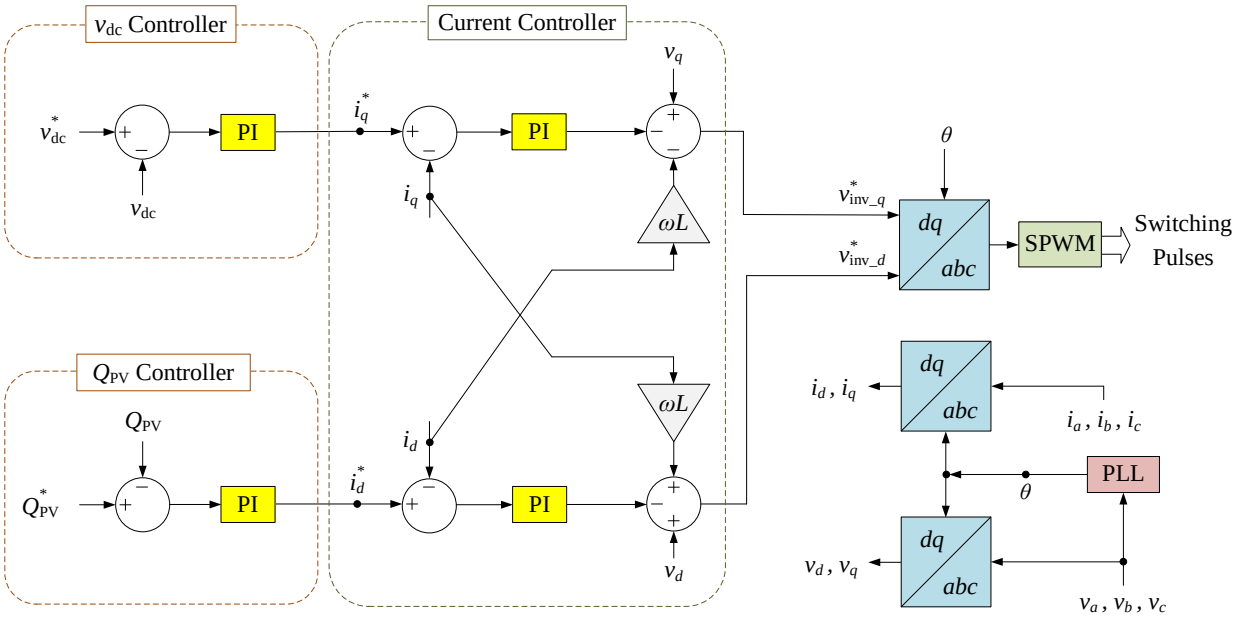

Figure B.10: Control scheme of PV's inverter for both grid-connected and islanded modes of operation.

based DG units. In such systems, the active power, frequency, voltage, and reactive power can be regulated within acceptable limits using droop control strategy. During islanded mode of operation, synchronous-based DGs usually regulate the frequency and voltage of the system using P-f and Q-v droop controllers, while in grid-connected mode, these DG units are typically operating in PQ control mode to supply the desired active and reactive power.

B.3.1 Basic Structure of Diesel Generator

The overall configuration of diesel generator system is depicted in Fig. B.11. This system consists of a synchronous generator which is equipped with governor and AVR. During islanded mode, the governor is responsible for controlling the generator speed, i.e., ω, and AVR is regulating the terminal voltage of generator, i.e., v_t, by providing the exciter field voltage and current, i.e., v_f and i_f. On the other hand, during grid-connected mode, governor controls the active power and speed of generator, i.e., P_e and ω, while AVR is used to regulate the generator terminal voltage and reactive power, i.e., v_t and Q_e.

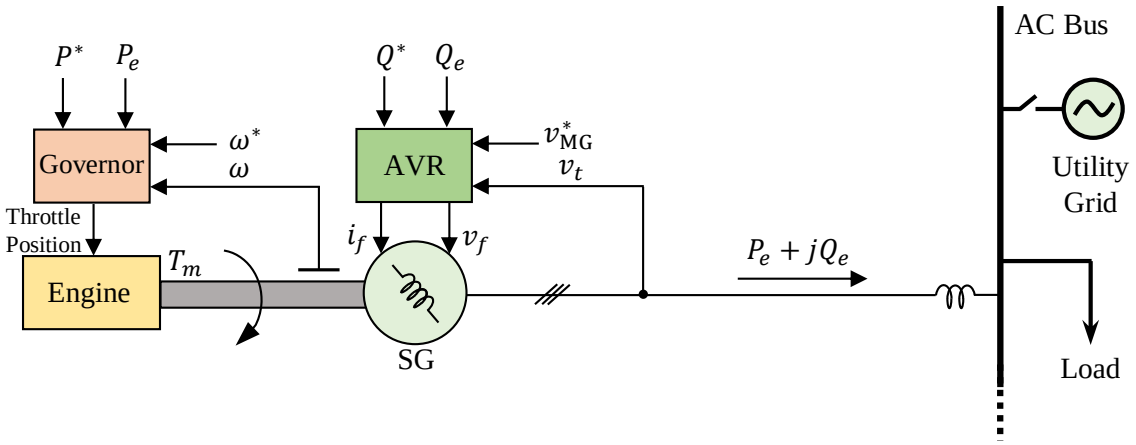

Figure B.11: Overall configuration of proposed system for diesel generator.

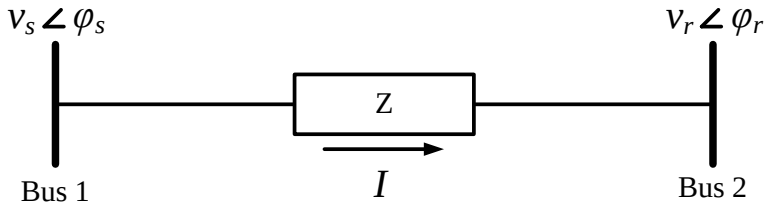

Figure B.12: Simplified model of an ac power transmission system.

B.3.2 Control Scheme of Diesel Generator

The principles of droop control approach along with the control schemes of governor and AVR are provided with more details in this subsection.

B.3.2.1 Principles of Droop Control Method

The model of a simple power transmission system is shown in Fig. B.12. By neglecting the line losses, the active and reactive power transmitted between the two busses can be calculated as follows:

$$P = \frac{v_{\mathrm{s}} v_{\mathrm{r}}}{X_L} \sin \delta \tag{B.4}$$

$$Q = \frac{v_{\mathrm{r}}}{X_L}(v_{\mathrm{s}} \cos \delta - v_{\mathrm{r}}) \tag{B.5}$$

where δ is the power angle and equal to $\varphi_{\mathrm{s}} - \varphi_{\mathrm{r}}$. Since δ has a small value, (B.4) and (B.5) can be simplified further by assuming $\sin\delta \approx \delta$ and $\cos\delta \approx 1$ as follows:

$$\delta \approx \frac{PX_L}{v_{\mathrm{s}} v_{\mathrm{r}}} \tag{B.6}$$

$$(v_{\mathrm{r}} - v_{\mathrm{s}}) \approx \frac{QX_L}{v_{\mathrm{r}}} \tag{B.7}$$

From (B.6) and (B.7), it can be concluded that the active and reactive power, respectively, have a significant effect on power angle and voltage difference. Therefore, power angle and voltage can be controlled by controlling the active and reactive power. Besides, based on the swing equation [118], frequency and power angle are related to each other. Thus, frequency can also be controlled by controlling the active power. This forms the basis of frequency and voltage droop control as follows:

$$f = f^* - R_P(P - P^*) \tag{B.8}$$

$$v = v^* - R_Q(Q - Q^*) \tag{B.9}$$

where R_P and R_Q are droop gains. f and v are measured frequency and voltage of the system, respectively, while f^* and v^* are the reference (or rated) frequency and voltage, respectively. P and Q are measured active and reactive power, respectively, while P^* and Q^* are the reference (or rated) active and reactive power, respectively. Fig. B.13 shows the P-f and Q-v droop characteristics obtained from (B.8) and (B.9).

Droop gains determine the steady-state speed\voltage versus active\reactive power of generating unit [119]. The ratio of speed deviation, i.e., $\triangle\omega$, or frequency deviation, i.e., $\triangle f$, to the change in active power, i.e., $\triangle P$, is equal to R_P. While R_Q can be obtained by dividing the voltage deviation, i.e., $\triangle v$, to the change in reactive power, i.e., $\triangle Q$. R_P and R_Q can be expressed as follows:

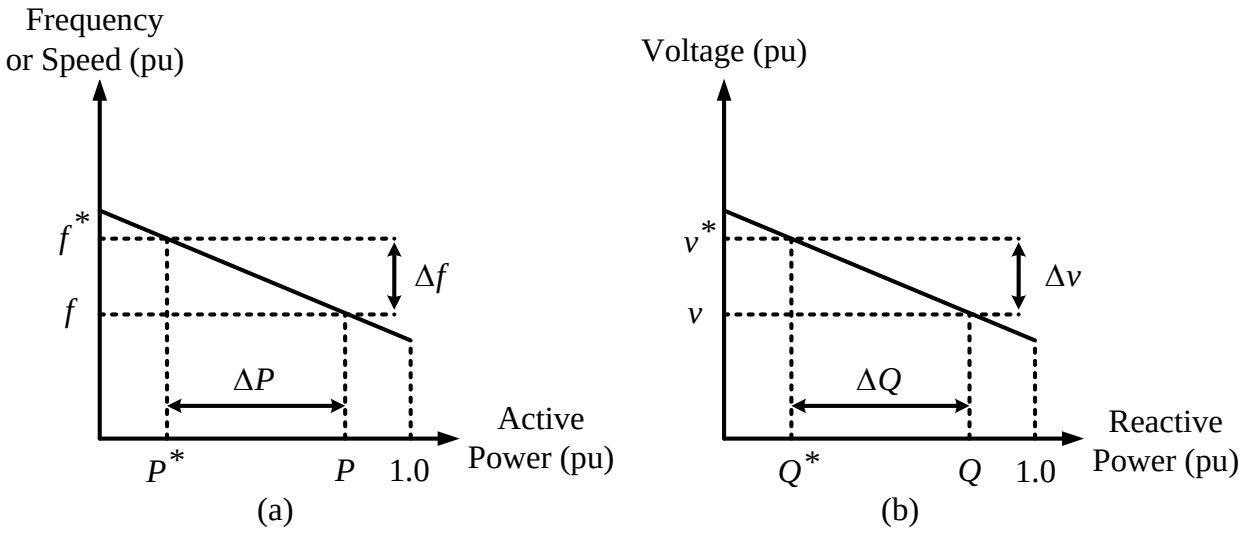

Figure B.13: (a) P-f and (b) Q-v droop characteristics.

$$R_P = \frac{\triangle\omega \text{ (or } \triangle f)}{\triangle P} \tag{B.10}$$

$$R_Q = \frac{\triangle v}{\triangle Q} \tag{B.11}$$

According to Fig. B.13(a) and equation (B.10), a 10% droop means that a 10% deviation in frequency causes a 100% change in the active power.

B.3.2.2 Governor and AVR Controllers

As can be seen in Fig. B.14, depending on the operation mode of the system, the governor controller selects which variables should be controlled. During islanded mode, the signal "Mode Selection" is set to "0", and thus, the generator speed, i.e., ω, is the only variable which is controlled. On the other hand, during grid-connected mode, the signal "Mode Selection" is set to "1", which makes the governor to control the generator speed and active power, i.e., ω and P_e, simultaneously.

One of the most challenging issues in each islanded mixed-inertia microgrid is synchronizing the generator with the grid before closing the breaker. This means that before transition from islanded to grid-connected mode, the ac-bus voltage must be synchronized with the

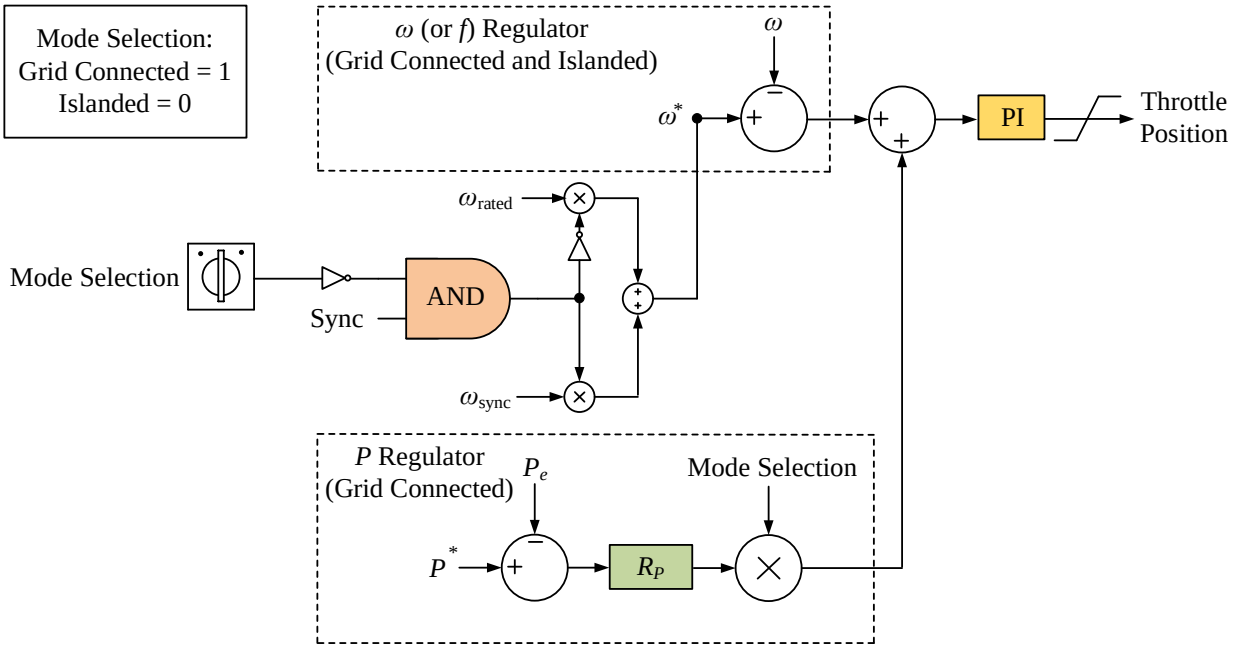

Figure B.14: Governor model including *P-f* droop controller in diesel generator system.

grid-side voltage. To accomplish this, four criteria must be met: (i) phase sequence, (ii) voltage magnitude, (iii) frequency, and (iv) phase angle. In order to avoid overcurrent while closing the breaker, the phase difference between the generator output voltage (or ac-bus voltage) and the grid-side voltage must be zero (or close to zero). In this way, before re-connecting the system to the main grid, subtraction of ac-bus voltage and the grid voltage will be equal to zero (or close to zero), and therefore, there won't be any overcurrent in the system. Fig. B.15 shows the waveforms and phasors for Phase-A of ac-bus voltage, i.e., v_a, and grid voltage, i.e., e_a, when they both have the same sequence, magnitude, and frequency, but there is a phase difference, i.e., φ, between them. Since both voltage waveforms have the same frequency, there is no way that they reach to each other. Therefore, as can be found from Fig. B.14, during islanded mode, i.e., Mode Selection = 0, the signal "Sync" is set to "0" so that ω_{rated}, which is equal to 1 pu, is chosen as ω^*. However, a few moments before closing the breaker, the signal "Sync" needs to be set to 1 in order to ensure a smooth transition upon switching from islanded to grid-connected mode. This results in choosing ω_{sync}, which is set to 0.99 pu, as ω^*. This means that the frequency of generator output voltage will be different from the frequency of grid voltage right before closing the breaker.

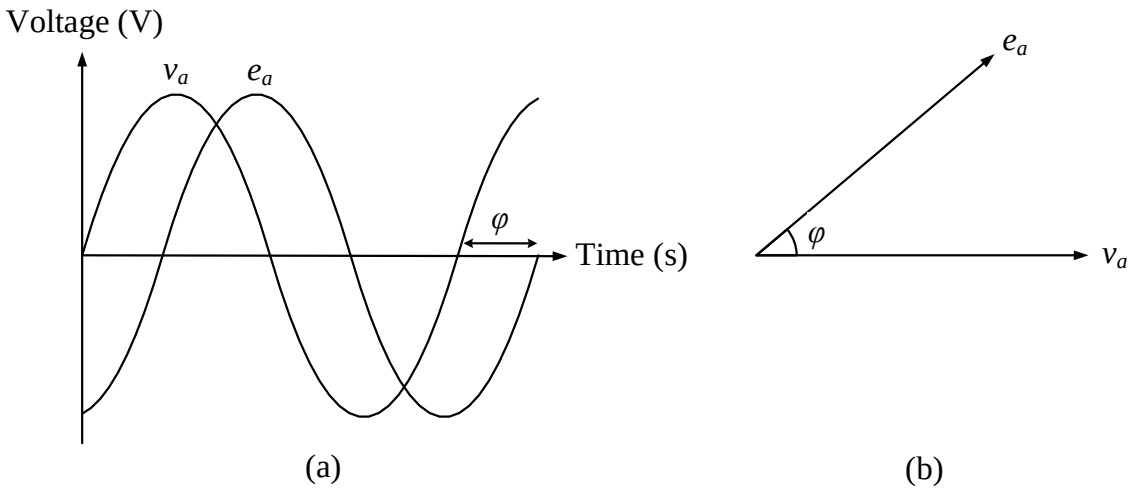

Figure B.15: (a) Voltage waveforms and (b) voltage phasors of generator side and grid side when there is a phase shift in between.

Nevertheless, there will be some moments that the phasors of both generator output voltage and grid voltage cross each other during which the system should reconnect to the utility grid by closing the breaker, i.e., Mode Selection = 1. After transition to grid-connected mode, the signal "Sync" should be set to "0" again.

The AVR and its Q-v droop controller are shown in Fig. B.16. The exciter model is based on the IEEE standard recommended AC5A excitation system [120]. Depending on the operation mode of the system, the governor controller selects the propoer variables to be controlled. During islanded mode, i.e., Mode Selection = 0, the generator terminal voltage, i.e., v_{t}, is the only variable which is controlled. On the other hand, when the system is connected to the main grid, the signal command "Mode Selection" is set to "1" in order to make the system to control the generator terminal voltage and reactive power, i.e., v_{t} and Q_{e}, simultaneously.

B.4 Modeling and Control of Microturbine System

This section provides an overview for microturbine system employed on the generation side of NG2 shown in Fig. 2.18, along with its basic structure and controller design. In recent years, microturbines have received wide attention in power industry as sources of

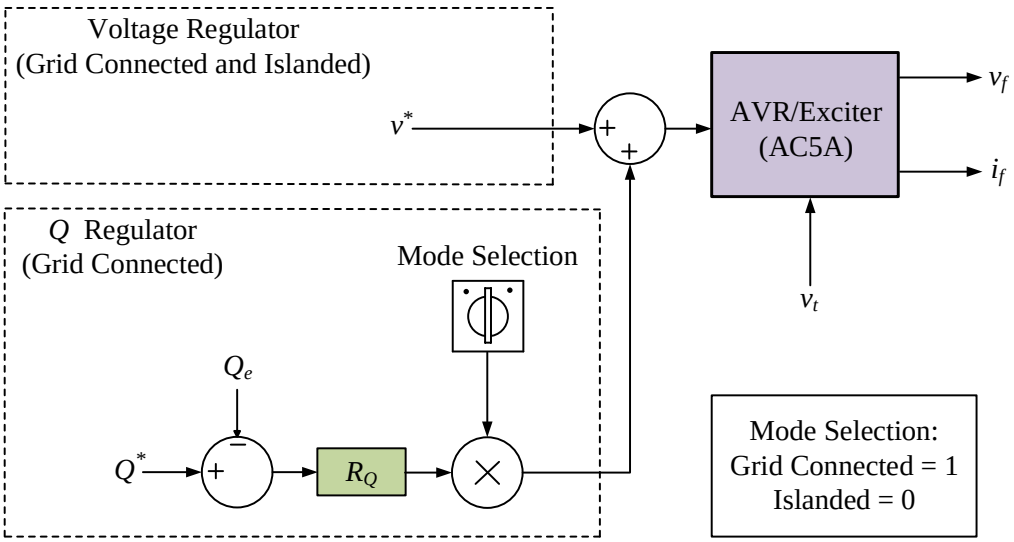

Figure B.16: AVR and its Q-v droop controller in diesel generator system.

power generation, particularly in areas where both electricity and the heat are in demand. In these areas, microturbines reach very high efficiency rates. Microturbines are able to operate during both grid-connected and islanded modes of operation. Microturbines are commonly used in combined heating and power systems (CHP). For the heat generation aspect, the waste heat from the microturbine is used to produce hot water, heat the building space, drive absorption cooling or desiccant dehumidification equipment, and to supply other thermal energy needs in a building or industrial process. The fuels used in microturbine systems commonly include natural gas, sour gas, gasoline, kerosene, and diesel fuel/distillate heating oil. In some recovery applications, waste gases can also be used instead of being released into the environment. As an example, the installed microturbine systems in the world headquarters of Black & Veatch company are shown in Fig. B.17. Also, the Capstone C65 microturbines and their internals can be seen in Figs. B.18 and B.19, respectively.

B.4.1 Basic Structure of Microturbine System

The basic structure of microturbine system is shown in Fig. B.20. In this system, the microturbine is connected to the dc link through an ac-dc rectifier. A dc-ac inverter is also included to convert the dc-link voltage to ac.

Figure B.17: Black & Veatch world headquarters microturbines.

B.4.2 Control Scheme of Microturbine System

The control schemes of ac-dc rectifier and dc-ac inverter implemented in microturbine system are explained in detail in this subsection.

B.4.2.1 Rectifier Controller

The microturbine is connected to the ac bus through a permanent magnet synchronous generator (PMSG), an ac-dc rectifier, and a dc-ac inverter as illustrated in Fig. B.20. The detailed control process of ac-dc rectifier for both grid-connected and islanded modes is shown in Fig. B.21. During grid-connected mode, the rectifier is responsible for controlling the active and reactive power transferred from PMSG, i.e., P_{PMSG} and Q_{PMSG}, while during islanded mode, the dc-link voltage, i.e., v_{dc}, and Q_{PMSG} are controlled by the rectifier.

The voltage drop between two points of a transmission system can be expressed as follows:

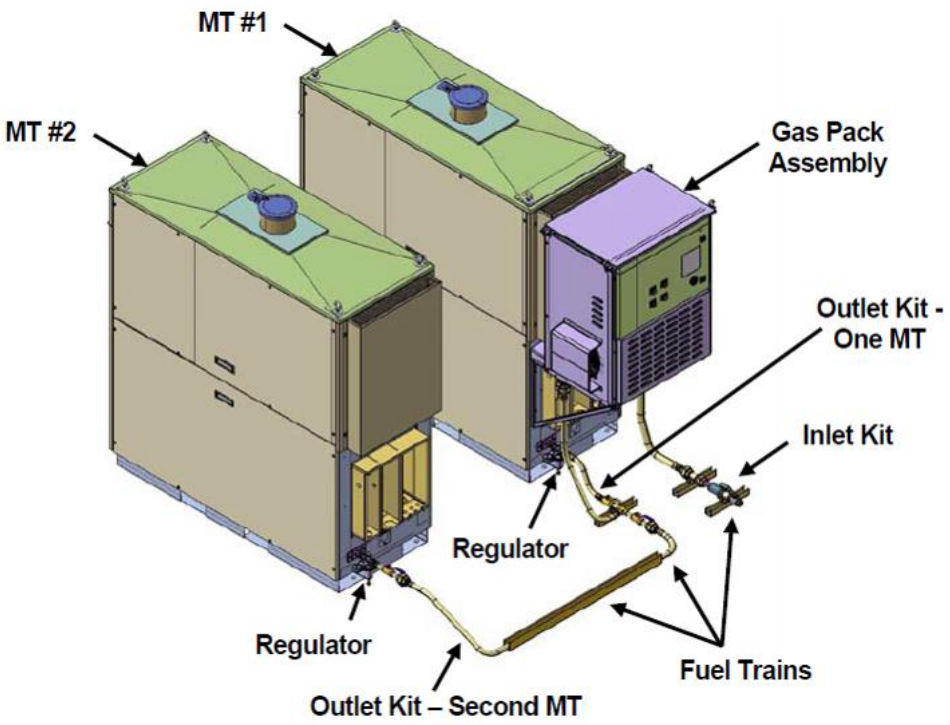

Figure B.18: Capstone C65 microturbines [121].

$$\triangle v = -K_Q Q \tag{B.12}$$

where $\triangle v$ is the voltage drop between two points of the system, K_Q is a coefficient dependent upon the properties of the transmission line, and Q is the transmitted reactive power between the points. According to (B.12), by making the reactive power transferred from PMSG equal to zero, the voltage drop across the implemented filter between the PMSG and rectifier would also be almost equal to zero. Hence, during both grid-connected and islanded modes of operation, Q_{PMSG} is set to zero using the rectifier controller.

A PLL is utilized for extracting the angle of PMSG's terminal voltage, i.e., θ_i. Then, using θ_i and Park transformation, the output voltage and current of PMSG are decomposed into dq reference frame variables.

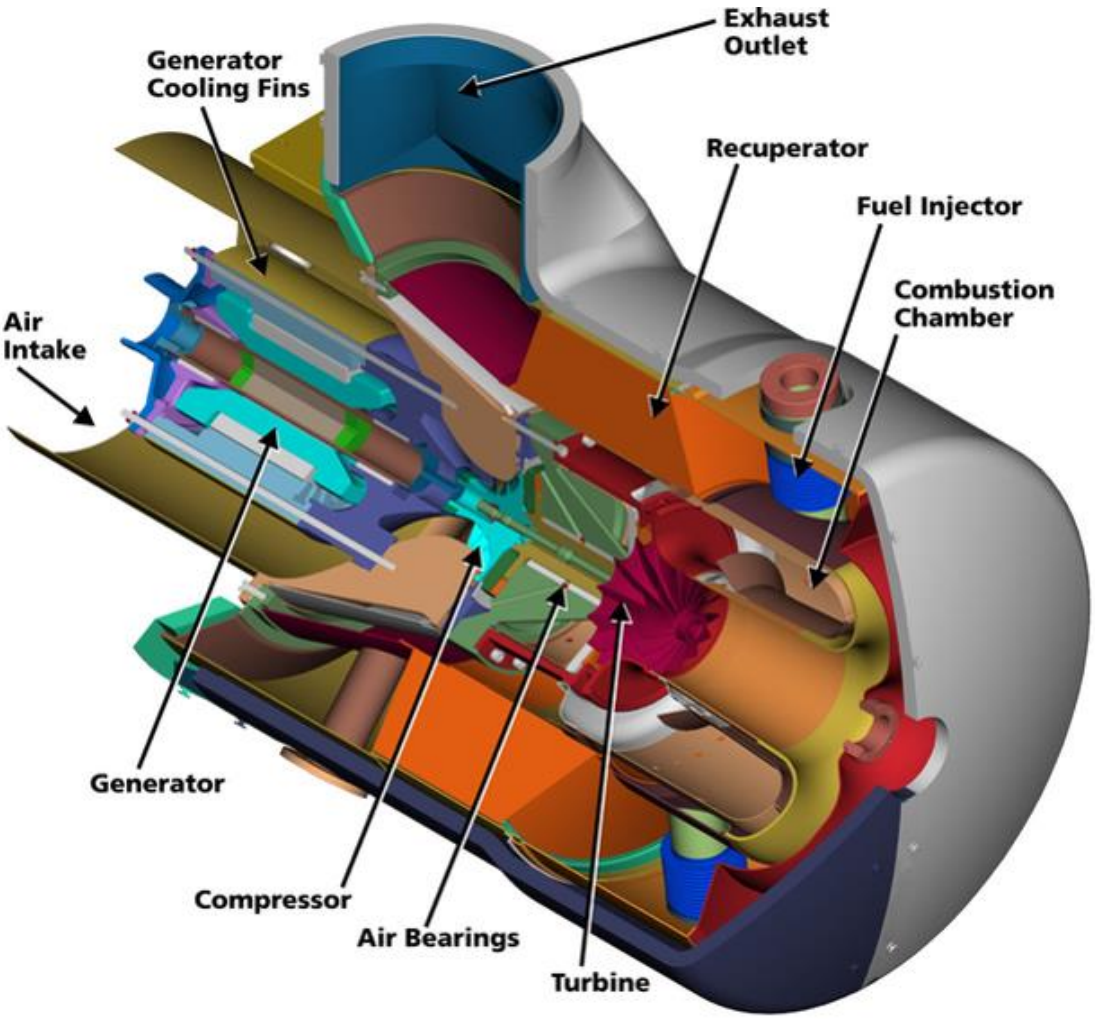

Figure B.19: Microturbine internals [121].

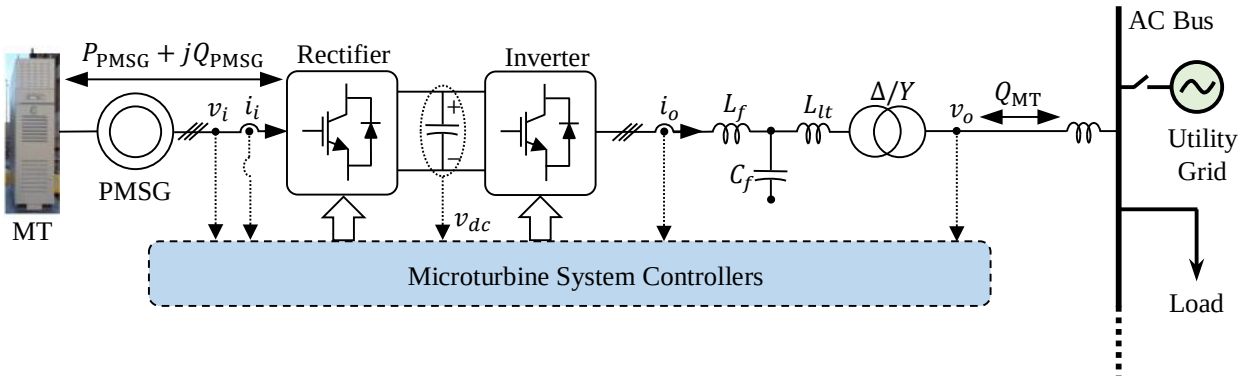

Figure B.20: Basic structure of microturbine system operating in both grid-following and grid-forming modes.

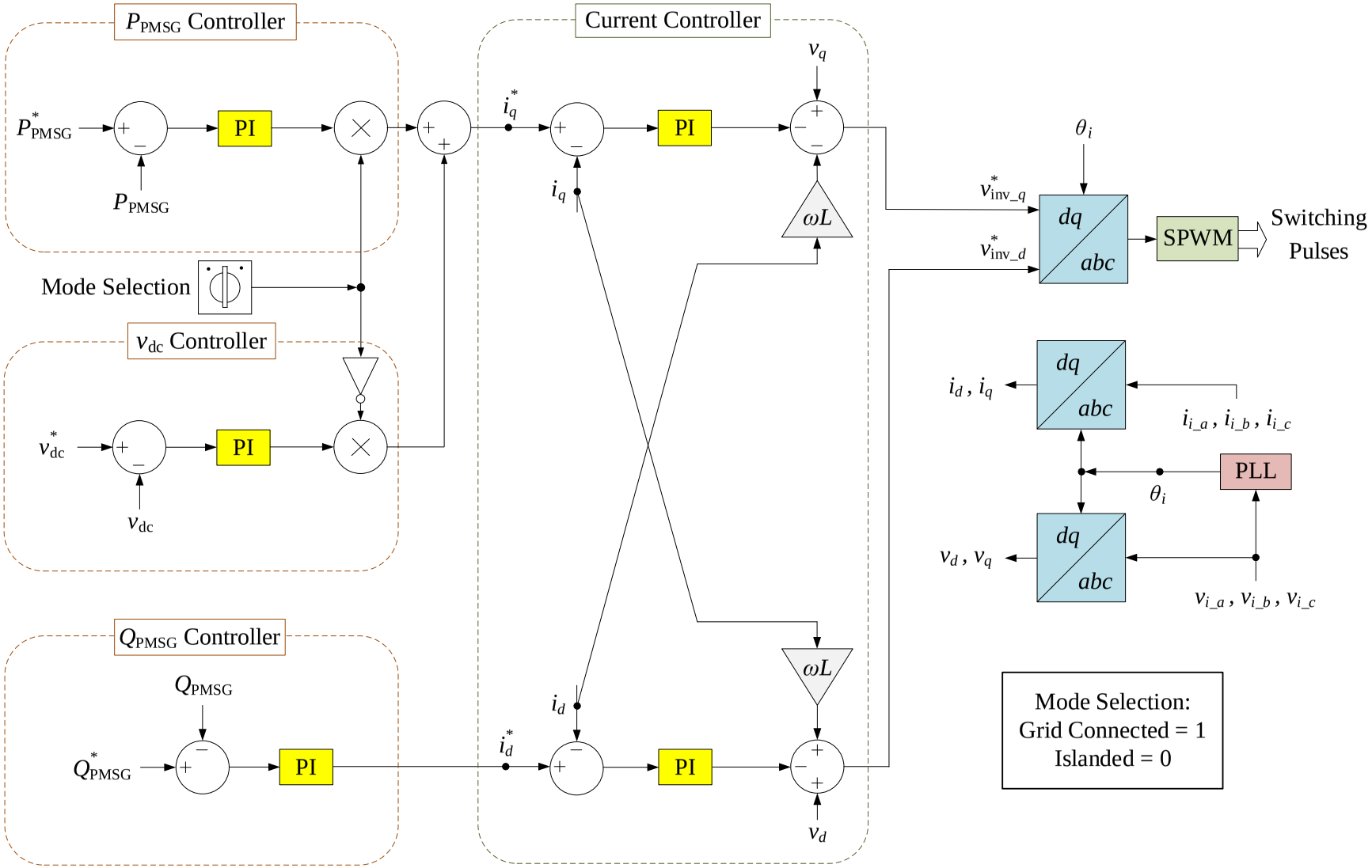

Figure B.21: Control scheme of rectifier in microturbine system for both grid-connected and islanded modes.

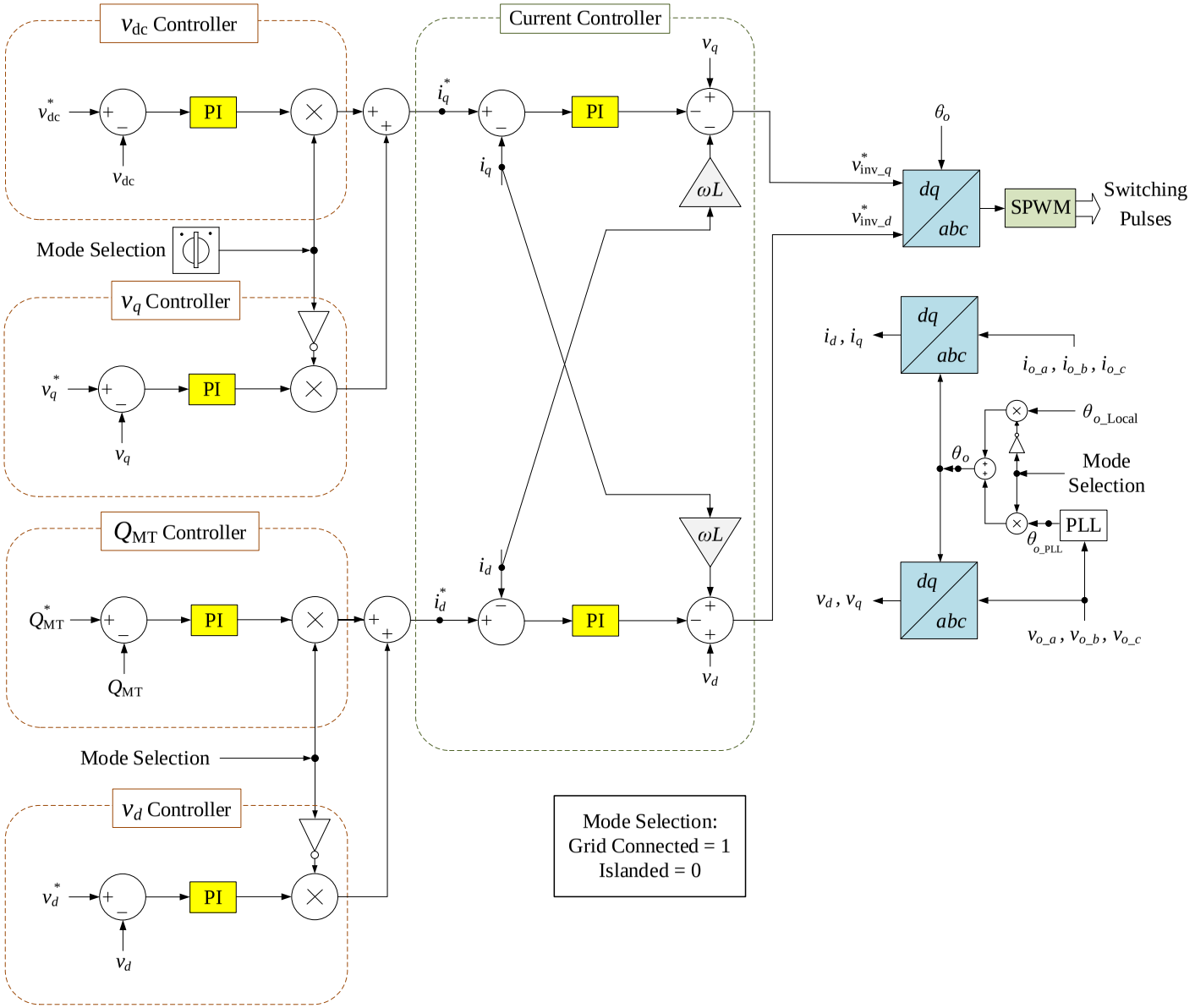

Figure B.22: Control scheme of inverter in microturbine system for both grid-connected and islanded modes.

B.4.2.2 Inverter Controller

Depending on the operation mode of the system, the inverter controller selects which variables should be controlled as illustrated in Fig. B.22. During grid-connected mode, the inverter regulates dc-link voltage, i.e., v_{dc}, and controls the reactive power transferring to the ac side, i.e., Q_{MT}. Besides, a PLL is used to extract the angle of output voltage, i.e., θ_{o_PLL}.

On the other hand, during islanded mode, the inverter is responsible for regulating the dq components of output voltage, i.e., v_d and v_q. In this mode of operation, the angle of output voltage is a locally generated periodical ramp signal, i.e., $\theta_{\mathrm{o\_Local}}$, which is varying from 0 to 2π with the frequency of 60 Hz.